CHARGE AND SPIN TRANSPORT IN GRAPHENE-BASED DEVICES

AHMET AVSAR

DEPARTMENT OF PHYSICS
NATIONAL UNIVERSITY OF SINGAPORE
(2014)

CHARGE AND SPIN TRANSPORT IN GRAPHENE-BASED DEVICES

AHMET AVSAR

A THESIS SUBMITTED

FOR THE DEGREE OF DOCTOR OF PHILOSOPHY

DEPARTMENT OF PHYSICS
NATIONAL UNIVERSITY OF SINGAPORE
(2014)

DECLARATION

I hereby declare that the thesis is my original work and it has been written by me in its entirety. I have duly acknowledged all the sources of information which have been used in the thesis.

This thesis has also not been submitted for any degree in any university previously.

Date

Ahmet Avsar

ACKNOWLEDGEMENTS

I would like to thank my supervisor, Prof. Barbaros Özyilmaz, for accepting me to work in his research group. During the entire period of my studies, I always felt his guidance, patience, support and care. Whenever I was stuck with my experiments, I always got invaluable input from him to solve the problems I was facing with. I admire his sixth sense while he was identifying the actual problems. While the characterization of heterostructure devices took longer than what we were expecting, he was always patient and gave me support and encouragement. I will never forget his support and care while I had problem with my scholarship during my PhD study. He created a wonderful laboratory from scratch (though we still don't have a couch and coffee machine) and I am sure the group will do breakthrough research more often in the coming future.

I am grateful to the head of graphene research center, Prof. Antonio Helio Castro Neto, for his invaluable discussions and theoretical support during my studies. His leadership while managing the world class center, his deep theoretical understanding of the matter and most importantly his interpretations on experimental results always amazed me. He is a truly role model for me. The special thanks go to Dr. Alexandra De Carvalho for her theoretical supports and discussions.

I especially thank to Dr. Jayakumar Balakrishnan, Mr. Gavin Kok Wai Koon and Mr. Jun You Tan. I would never be able to complete my studies without their helps. Dr. Jayakumar Balakrishnan was always there whenever I need to discuss anything related to transport phenomena in graphene. Mr. Gavin Kok Wai was always helping me whenever I need a hand while I was working with MBE system or doing measurements. He has an eidetic memory and you should not leave your credit card numbers around him. I don't know how to express my gratitude to Mr. Jun You Tan. It was impossible to make heterostructure project work without his hard working and problem solving abilities.

I am grateful to Dr. Xu Xiangfan for his guidance at the early stage of my PhD studies. The weekly spin meetings were very beneficial thanks to the critical discussions with Dr. Eoin O'Farrel and Dr. Thiti Tychatanapat. Dr. Tychatanapat was always patient with my simple transport questions and his magic program made the proximity work possible. I will like to extend my gratitude to all my group members especially Mr. Henrik Andersen, Mr. Orhan Kahya, Dr. Jong Hak Lee, Dr. Raghu Sharma, Mr. Wu Jing, Mr. Chee Tat Toh, Ms. Yuting Yeo, Dr. Steven Koenig, Mr. Alexandre Pachoud and all members of Özyilmaz group and graphene research center for their friendship and help during my PhD studies.

I would like to thank Prof. Gernot Güntherodt, Prof. Bernd Beschoten, Dr. Tsung-Yeh Yang and Mr. Frank Volmer from the RWTH Aachen University, Prof. Byung Hee Hong and Dr. Su-Kang Bae from the Sungkyunkwan University for their help at the initial spin transport experiments.

I would also like to thank my close friends Dr. Mustafa Eginligil, Mr Mehmet Erdogan and Mr. Kadir Durak. Singapore is a memorable place for me with their accompany. I also like to thank Mr. Orkun Saka for his constant support and helps from high school to now.

I would like to gratitude my family. Without their support and faith, I would never find a chance to follow my dreams and reach this point. I will never forget the moment while my brother, Mr. Mehmet Avsar, was convincing my parents for my initial internship and PhD studies at abroad. Finally I thank Ms. Saziye Yorulmaz (Avsar (soon)) for her patience and love.

Table of Contents

ABSTRACT

The field of spintronics offers new technologies and fundamental discoveries by using the spin degree of freedom of electron. Having low spin orbit coupling, negligible hyperfine interaction and extremely high electronic quality make graphene a promising material for spintronics studies. While the exceptionally long spin relaxation length was demonstrated experimentally in mechanically exfoliated graphene-based spin valve devices, the manipulation of spin current for the practical applications was missing. The experimental work presented in this thesis focuses on understanding the fundemantal spin transport properties of graphene to prepare it for future spintronics applications.

In the first part of the thesis, I study the spin transport properties of CVD grown graphene. Spin injection, transport and detection in CVD single and bi-layer graphene are successfully demonstrated. I show that the CVD specific structural differences such as wrinkles, grain boundaries and residues do not limit spin transport properties of CVD graphene. The observation of long spin relaxation length comparable to the exfoliated graphene samples makes CVD graphene a promising material of choice for possible spintronics applications. The large scale CVD grown graphene also allows the batch-fabrication of large arrays of lateral spin valve devices with a fast-around time well suited for studying the device physics.

In the second part of thesis, charge transport property of graphene is studied in heterostructure devices. While the graphene field effect transistors fabricated on various 2D substrates show enhanced electronic mobilities compared to conventional SiO2 substrate, BN and WS_2 substrates appeared to be the most promising substrates to reach high electronic mobilities in graphene. Our results raise the importance of ideal choice of material for graphene-based heterostructure devices before building the complex heterostructures.

The absence of significant spin orbit coupling in graphene is detrimental for the manipulation of spin current in graphene based devices. In the last part of

thesis, I demonstrate that with the creation of an artificial interface between graphene and WS_2 substrate, graphene acquires a SOC as high as 17meV with a proximity effect, three orders of magnitude higher than its intrinsic value. This proximity effect leads to the spin Hall effect even at room temperature. These results open the doors for the realization of Datta-Das type spin field effect transistors.

List of Figures

CHAPTER 1 Introduction

1.1 Spintronic

The discovery of electron, an elementary particle, by J.J. Thomson in 1897 started a new era in science and technology. After having a better understanding of the fundamental properties of this charged particle, J. Bardeen, W. H. Brattain and W. B. Shockley created the first transistor in 1947 at Bell laboratories[1]. This discovery is the building block of the modern electronic devices. In fact, by using neutral silver atoms, O. Stern and W. Gerlach had shown that electrons have intrinsic angular momentum[2]. In 1925, G. Uhlenbeck and S. Goudsmit discovered that the angular momentum of electrons is coupled with the magnetic field[3], [4]. It is soon understood that if the spin of electron is measured under magnetic field, only two distinct values can be obtained: spin-up (ħ/2) and spin-down (-ħ/2). This interesting finding triggered the area of spintronics that focuses on the fundamental discoveries and new technologies by using the spin degree of freedom of electrons[5]. For example, these two distinct spin states can be assigned to zero and one states for carrying out the binary logic operations[6].

The effect of spin on charge transport was noticed in 1857 for the first time. W. Thomson observed that the resistance of a ferromagnetic material (FM) depends on the relative orientation of the magnetization and current[7], [8]. This effect is known as anisotropic magneto resistance (AMR) effect. The breakthrough experiments in spintronics field were performed independently by A. Fert and P. Grunberg in 1988. They showed that the resistance of Fe/Cr multilayer structure depends on the relative orientation of the magnetization of the magnetic material[9], [10]. This effect results in a giant magneto resistance (GMR). The 2007 Nobel Prize for physics was awarded to A. Fert and P. Grunberg for the discovery of GMR effect. GMR effect is utilized to read the data in the magnetic field sensor of the hard disks[11]. The discovery of the

GMR effect renewed the interest for spintronics. The insertion of a thin tunnel barrier between two FM layers[12], [13] leaded some new applications such as TMR MRAM.

The effort to induce the magnetization in non-magnetic materials started with the theoretical predictions by A. Aronov and G. Pikus in 1976[14]. Nine years after this calculation, M. Johnson and R. H. Silsbee managed to create spin accumulation in aluminum (Al) by flowing a charge current from injector permalloy (Py) electrode to detector Py electrode[15]. The observation of spin injection, transport and detection in Al accelerated the research of induced magnetization in metal and semiconductor materials. In 2001, F. J. Jedema utilized a new four terminal non-local technique to separate the charge and spin currents in lateral spin valve devices to mask the spurious charge related effects that mimicking the spin signal[16]. Spin transport measurements on metallic materials such as Silver (Ag), Copper (Cu), and Aluminum (Al) show spin relaxation lengths up to micron size at room temperature (RT)[17], [18]. The early attempts for the spin injection into semiconductors failed due to conductivity mismatch between semiconductor and ferromagnetic contacts[19]. This problem was solved by introducing a tunnel barrier between ferromagnetic and non-magnetic materials. Spin injection into semiconductors at low temperatures was successfully demonstrated[20], [21].

While the spin injection has been demonstrated successfully in the lateral spin valve devices, the measured spin relaxation lengths are not very ideal for the practical spintronics applications. The isolation of 2D crystalline graphene from graphite triggered a tremendous attention for electronic and spintronics communities[22]. Having very small spin orbit coupling[23], negligible hyperfine interaction[24] and very high electronic charge mobility[25] makes graphene very promising material for such spin transport studies too. A spin relaxation length of ~ 100 μm is extracted in graphene based spin valve devices[26].

1.2 Thesis Outline

In this thesis, I present the experimental study on spin transport in graphene. In the first part of the thesis, I demonstrate spin injection, transport and detection in CVD grown graphene-based spin valve devices by utilizing the four terminal non-local geometry[27]. I show that spin relaxation times comparable to the exfoliated graphene samples demonstrating that CVD specific structural differences such as nano-ripples[28] and grain boundaries[29] do not limit spin transport in the these samples. These observations make Cu-CVD graphene a promising material of choice for large scale spintronic applications. In the second part of the thesis, I study the electronic properties of graphene on various two-dimensional (2D) substrates. It is found that not only the surface roughness, but also the charge traps on substrate affect the graphene mobility. Our results raise the importance of ideal choice of material for graphene-based heterostructure devices before building increasingly complex graphene-based heterostructures. In the last part of the thesis, I demonstrate that with the creation of an artificial interface between graphene and WS_2 substrate, graphene acquires a spin orbit coupling (SOC) as high as 17meV, three orders of magnitude higher than its intrinsic value[30], without modifying any of the structural properties of the graphene. Such proximity SOC leads to the spin Hall effect (SHE) even at room temperature and opens the doors for spin FETs. Finally I discuss the current status of the graphene spintronics field and offer possible experiments to solve the major problems in the field. This thesis includes seven chapters and a brief outline for the each chapter is given below:

Chapter 2: The basic theoretical spintronics concepts are discussed. I introduce the spin injection, transport and detection phenomena in non-magnetic materials. The non-local spin valve geometry technique is explained. After discussing the basics of SHE, I present the electronic properties of graphene briefly.

Chapter 3: In this chapter, I discuss the experimental techniques required to fabricate and characterize the graphene-based spin valve and heterostructure devices. I demonstrate the mechanical exfoliation technique, the electron beam lithography technique, the electron beam evaporation technique and the graphene transfer technique. The details of the device fabrication recipes for charge and spin based devices are given. Finally, I present the various measurement techniques and set-up that have been utilized to characterize the charge and spin transport properties of graphene.

Chapter 4: The experimental results on the spin transport in CVD grown single and bi-layer graphene are discussed. I discuss the effect of CVD specific structural differences on the spin transport. Finally, the spin transport properties of exfoliated and CVD graphene are compared.

Chapter 5: In this chapter, the surface morphologies of the 2D boron nitride (BN), gallium selenide (GaSe), tungsten disulfide (WS_2) and molybdenum disulfide (MoS_2) crystals are characterized with optical and atomic force microscopy techniques. The effect of the surface morphology and the surface charged traps on the charge transport properties of graphene are studied experimentally.

Chapter 6: I present the experimental results on charge and spin transport in graphene on WS_2 substrate. I show that the electronic mobility of graphene is enhanced significantly on WS_2 substrate. I present data on the SOC enhancement due to the proximity effect. The proximity induced SHE in graphene is demonstrated for the first time without changing the structural properties of graphene. The origin of such proximity effect is discussed with theoretical and experimental supports.

Chapter 7: In this chapter, I summarize the experimental work presented in this thesis and give an outlook.

CHAPTER 2 Basic Concepts

In this chapter, I provide some essential theoretical concepts for understanding the experiments performed in the thesis. I discuss the injection, transport and detection of spin current in non-magnetic (NM) materials. Then, I describe the manipulation of the spin current with magnetic field (Hanle spin precession) in such systems. The generation, transport, manipulation and detection of spin current in H-bar geometry via Spin Hall effect are also discussed. Finally, I explain some basic concepts of graphene including the electronic band structure, field effect behavior and magneto-transport properties. The following works were consulted extensively and used as a guide for the preparation of this chapter: (1) F.J. Jedema PhD thesis[31], (2)N. Tombros PhD thesis[32], (3) D. Cooper et al., "Experimental review of graphene"[33] and (4) J. Balakrishnan PhD thesis[34]

2.1 Electrical spin transport

2.1.1 Electrical spin Injection and detection

The electrical spin injection relies on the creation of a non-equilibrium population of the spin-up and spin-down currents. Since the density of states and the Fermi velocity of the two spin sub-bands at the Fermi level are different in a ferromagnetic (FM) material, FM has non-equilibrium spin-up and spin-down conductivities[31]. In a 1D system, the spin current density can be shown as[35]

$$J_{\uparrow\downarrow} = \frac{\sigma_{\uparrow\downarrow}\partial\mu_{\uparrow\downarrow}}{e\partial x} \tag{2.1}$$

where $\mu_{\uparrow\downarrow}$ is the electrochemical potential, $\sigma_{\uparrow\downarrow} = e^2 N_{\uparrow\downarrow} D_{\uparrow\downarrow}$ is the electrical conductivity, $D_{\uparrow\downarrow} = \frac{1}{2}\vartheta_{F\uparrow\downarrow} l_{\uparrow\downarrow}$ is the diffusion constant, $\vartheta_{F\uparrow\downarrow}$ is the Fermi

velocity, $l_{\uparrow\downarrow}$ is the free mean path for spin-up and spin-down charges. The spin polarization in ferromagnetic material can be described as

$$P = \frac{J_\uparrow - J_\downarrow}{J_\uparrow + J_\downarrow} = \frac{\sigma_\uparrow - \sigma_\downarrow}{\sigma_\uparrow + \sigma_\downarrow} \tag{2.2}$$

Since the net charge current is $J = J_\uparrow + J_\downarrow$ and the net spin current is $J_S = J_\uparrow - J_\downarrow$, the spin-up and spin down current can be written as

$$J_\uparrow = (1 + P)\frac{\sigma_{Total}}{2e}\frac{\partial \mu_\uparrow}{\partial x} \tag{2.3}$$

$$J_\downarrow = (1 - P)\frac{\sigma_{Total}}{2e}\frac{\partial \mu_\downarrow}{\partial x} \tag{2.4}$$

The equations of (2.3) and (2.4) show that the densities of spin-up and spin-down currents are different ($J_\downarrow \neq J_\downarrow$). This means that a charge current that passes through a ferromagnetic material will be spin polarized. If a ferromagnetic material is in contact to a non-magnetic material, this spin polarized current will create a spin accumulation in nonmagnetic material[15]:

$$\frac{D_S \partial^2 \Delta\mu}{\partial^2 x} = \frac{\Delta\mu}{\tau_S} \tag{2.5}$$

where D_S is the spin diffusion constant, τ_S is the spin relaxation time, $\Delta\mu = \mu_\uparrow - \mu_\downarrow$ is the electrochemical potential difference of spin-up and spin-down and x is the distance from the injector contact. As can be seen from equation (2.5), the spin accumulation decays exponentially with the distance. This spin signal can be detected with a second ferromagnetic contact if the separation between injector and detector contacts is less than a distance that non-equilibrium spin-up and spin-down currents still persist. This length is known as spin relaxation length and it is described as:

$$\lambda_S = \sqrt{\tau_S D_S} \tag{2.6}$$

The schematic representation of density of states for ferromagnetic metal, un-polarized non-magnetic metal and polarized non-magnetic metal is shown in Figure 2-1. The non-equilibrium population of the spin-up and spin-down states is created in nonmagnetic metal due to an induced magnetization from the ferromagnetic metal[31]. The injected spin travel in this non-magnetic material and detected by the second ferromagnetic-metal. The total resistance of device depends on the relative polarization directions of the injector and detector ferromagnetic contacts. The parallel and anti-parallel polarization configurations can be obtained by using the shape anisotropy property of ferromagnetic materials. Towards this purpose, ferromagnetic injector and detector contacts are commonly fabricated with different widths or thicknesses in order to have different coercive fields for each of them[36], [37]. The continuous sweeping of magnetic field creates the parallel and anti-parallel orientations of injector and detector contacts. This results a resistance switching since the spins reaching to detector electrodes will see a higher resistance in anti-parallel orientation of ferromagnetic contacts compared to parallel orientation.

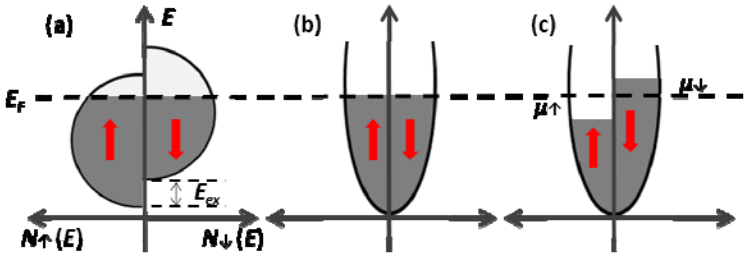

Figure 2-1. Density of states(DOS): Schematic representation of DOS for (a) ferromagnet material, (b) unpolarized non-magnetic material and (c) polarized non-magnetic material. The spin polarized current generates spin accumulation in non-magnetic materal.

2.1.2 Non-local spin valve geometry

As discussed in the section 2.1.1, The FM/NM/FM structure can be utilized for the realization of spin injection, spin transport and spin detection phenomena. In this structure, the charge and spin currents flow together. The measured signal is a combination of spin dependent resistance, contact resistance and non-magnetic material resistance. The ratio of the spin dependent resistance to the total resistance is very small and this makes the realization of spin dependent transport very challenging. Since the charge and spin currents flow together in the channel, many charge based phenomena such as Hall effect, interference effect and anisotropic magneto-resistance effect can even mimic the spin signal[16], [17], [37]. In order to separate the charge and spin currents, a non-local technique is used. The schematic of non-local spin valve geometry is shown in Figure 2-2-(a). This device geometry consists of four contacts and the middle two contacts are utilized as spin injector and detector. While the outer electrodes can be non-magnetic metal contacts, they are commonly formed with ferromagnetic metals to simplify the device fabrication. In this geometry, a charge current is first sent from the injector contact to the reference contact (the red arrow in Figure 2-2-(a) represents the charge flow direction). Since the charge current is spin polarized, the generated spin current diffuses all over the sample. Since there is no net charge current flowing outside of the injector- reference contact channel, a pure spin signal presents at the rest of sample. The spin dependent electrochemical potential can be measured between the detector and the second reference electrodes. The measured signal depends on the relative polarization directions of the injector and detector contacts. The polarization directions of the injector and detector electrodes can be varied with the application of an in-plane magnetic field along the easy axes of electrodes.

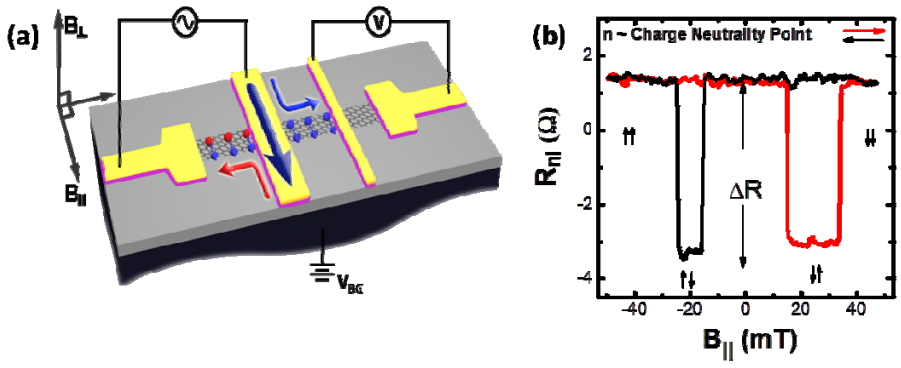

Figure 2-2. Non-local spin valve transport: (a) Schematics for a graphene based non-local spin-valve device. This geometry separates the charge and spin currents. (b) Room temperature bi-polar non-local spin signal in a graphene based spin valve device as a function of in-plane magnetic field.

The spin injection efficiency depends on the relative conductivities of the FM and NM[19]. For effective spin injection, the resistance of the FM/NM interface has to be smaller than the resistivity of FM and NM and the resistivity of FM and NM has to be comparable. Since there is a significant difference between the conductivities of ferromagnetic contact and graphene, a thin Al_2O_3 tunnel barrier was inserted by van Wees group between FM and graphene to combat this conductivity mismatch problem[37]. The introducing of Al_2O_3 tunnel barrier resulted in spin injection efficiency up to 10%. Since MgO based TMR devices show record MR values due to the crystalline nature of MgO[13], we created MgO tunnel barrier for spin injection into graphene.

Such measurement in graphene-based spin valve devices is shown in Figure 2-2-(b). As can be seen in the Figure 2-2-(b), the strength of the coercive fields for the injector and detector electrodes are 18mT and 22mT, respectively.
Figure 2-2-(b) shows the in plane magnetic field dependence of spin signal in a graphene based spin valve device. A magnetic field of 50mT is applied along the easy axes of ferromagnetic contacts to polarize them in the same orientation first. The magnetic field is continuously swept back to -50mT. While magnetic

field is at ~ -20mT, the polarization direction of the wider contact is reversed and a resistance switching is observed. The spin signal stays constant until the polarization direction of the second contact also reverses. In this configuration, the spin signal changes back to its initial value. The obtained spin signal depends on spin injection efficiency (P), spin relaxation length (λ_S), the contact area (A), the conductivity of the graphene (σ) and the separation between injector and detector contacts (x) with the following equation[30], [37]:

$$R_{NL} = \frac{P^2 \lambda_S}{2A\sigma} exp\left(\frac{-x}{\lambda_S}\right) \tag{2.7}$$

The non-local resistance (R_{NL}) decays exponentially as a function of distance between injector and detector electrode. While A, σ and x parameters in the equation (2.7) are known, P and λ_S values are not known. P and λ_S can be correctly estimated from x dependent measurements.

2.1.3 Electrical spin precession

The non-local spin signal can be manipulated with an externally applied magnetic field. The application of a perpendicularly applied magnetic field ($B_\perp$) exerts a torque on the spins and this result in the precession of spins with a frequency of

$$\boldsymbol{w_L} = \frac{-g\mu_B \boldsymbol{B}_\perp}{\hbar} \tag{2.8}$$

where g is the g factor for electron, μ_B is the Bohr magneton, ħ is the Planck constant (Figure 2-3-(b)). When the injected spin current reaches to the detector, the projection of spin to the detector is detected. If the polarization directions of the injector and detector are parallel (anti-parallel), the total non-local signal shows a maximum (minimum) signal before $B_\perp$ is applied. As $B_\perp$ is increased, the signal starts to decrease (increase) and reaches to zero once the

precession angle is 90°. The signal reaches its minimum (maximum) value at the precession angle is 180°. The signal starts to increase (decrease) as precession angle increases and eventually it reaches to its initial maximum (minimum) value at the precession angle of 360°. The angle dependence of non-local signal is shown in Figure 2-3-(a) with assuming that transport is ballistic.

2.1.3

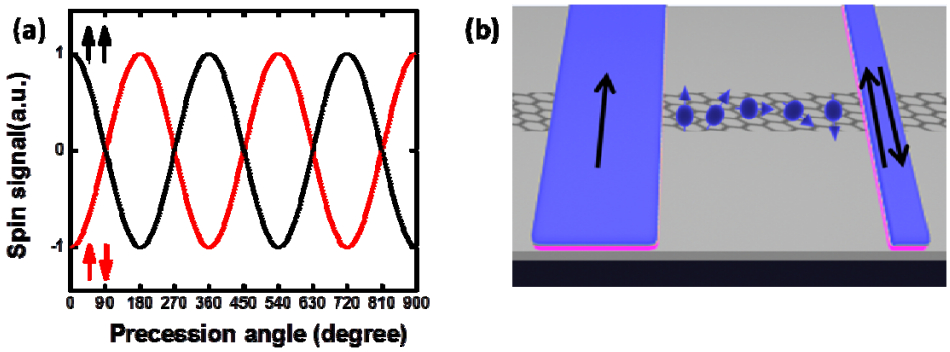

Figure 2-3. Hanle spin precession: (a) The oscillation of spin signal as a function of precession angle. (b) The schematics of spin precession measurement for different polarization configurations. Black arrows represent the polarization directions of ferromagnetic contacts and blue arrows represent the precession of spin signal under perpendicularly applied magnetic field.

However, the transport characteristic of our devices is diffusive. Spins have different paths between the injector and detector electrodes. While spins are precessing, they are also relaxed during the transport. This result in damping of the spin signal at higher $B_\perp$ .The Bloch equation in this case has the following form[30]:

$$D\frac{\partial^2 \boldsymbol{\mu}}{\partial^2 x} - \frac{\boldsymbol{\mu}}{\tau_S} + \boldsymbol{w_L}\, x\, \boldsymbol{\mu} = 0 \tag{2.9}$$

The first term describes the spin diffusion, the second term describes the spin relaxation and the last term describes the precession of spin under $B_\perp$.

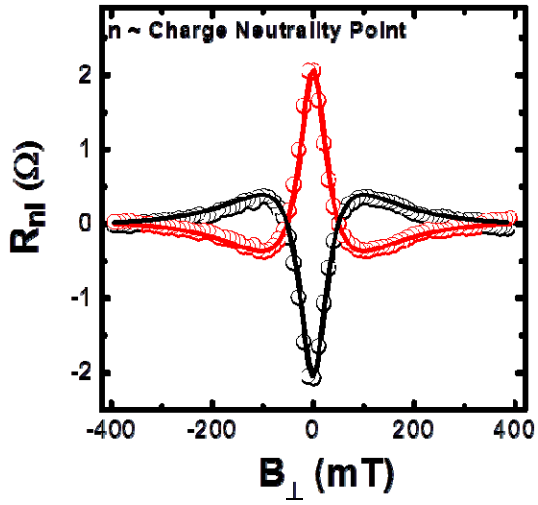

Figure 2-4. Hanle spin precession: Spin precession measurement in graphene based spin valve by employing non-local spin valve geometry. The circles represent the measurement data and the lines represent the fitting of the signal. Red (black) color shows the room temperature measurement result when the relative orientation of injector and detector ferromagnets are parallel (anti-parallel).

Figure 2-4 shows the spin precession measurement in graphene-based non-local spin valve device. Initially, the polarization directions of injector and detector contacts are aligned to be parallel (anti-parallel) with the application of an in-plane magnetic field. The magnitude of spins signal decreases (increases) as the strength of $B_\perp$ is increased. A damping in spin signal at high $B_\perp$ is observed. The resulting signal can be fit with the following equation[37]:

$$R_{NL} \propto \int_0^\infty \frac{1}{\sqrt{4\pi D_S t}} exp\left(\frac{-L^2}{4D_S t}\right) exp\left(\frac{-t}{\tau_S}\right) \cos(w_L t)\, dt \tag{2.10}$$

From this equation, we can extract the important spin parameters such spin diffusion constant (D_S), spin relaxation time (τ_S) and spin relaxation length

($\lambda_S = \sqrt{\tau_S D_S}$). From the fitting (red and black lines in Figure 2-4), we get τ_S= 180ps, D_S=0.007m^2/s and λ_S=1.1μm. We can also calculate the spin injection efficiency, P ~ 6%, by inserting the L, R_{NL}, σ, A and extracted λ_S values into the equation (2-7). The calculated P value is similar to what has been obtained with the previous spin valve devices fabricated with Al_2O_3 tunnel barrier. We associate such low P value to the presence of pinholes in MgO tunnel barrier.

2.2 Spintronics properties of graphene

2.2.1 Introduction

Having very small spin orbit coupling[23] thanks to the low atomic number of carbon atom and negligible hyperfine interaction[24] raised the expectations of a λ_S ~ 100μm in graphene. While the observation of spin injection, transport and detection in graphene-based spin valve device is very promising, there is a striking difference between the theoretically estimated and experimentally observed λ_S. The identification of main spin scattering mechanism in graphene can help to understand the difference between theory and experiment and offer suggestions.

2.2.2 Spin scattering mechanisms in graphene

The transport characteristic of the fabricated graphene-based spin valve devices is diffusive. As a result of this, the spin scattering is observed during the transport. In the diffusive regime, the spin scattering mechanisms types of Elliott-Yafet[38], D'yakonov-Perel[39], Bir-Aronov-Pikus[40] and hyperfine interactions are discussed to be the main spin scattering mechanism in non-magnetic materials. The recent experiments show that Elliott-Yafet and D'yokonov-Perel types of spin scattering mechanism are valid for graphene. In the Elliott- Yafet (EY) mechanism, spin dephasing occurs during momentum scattering. The momentum scattering sources such as impurities[41], substrate induced sources[42], boundaries[43] and phonons[44] can flip the spin. The

comparison of spin and momentum scattering times points that spin dephasing happens after ~thousands of such charge collisions. The probability of electron spins to flip increases as the number of such momentum scattering events increase. Therefore, the spin relaxation time is directly proportional to the momentum scattering time ($\tau_s \propto \tau_p$). On the other hand, the D'yakonov-Perel (DP) mechanism refers to the case where spin dephasing takes place between momentum scattering events, which may result from random Bychkov-Rashba like spin-orbit fields. This leads to a spin relaxation time, which is inversely proportional to the momentum scattering time ($\tau_s \propto \tau_p^{-1}$) .The electric field effect in graphene provides a convenient tool to correlate τ_s and τ_p. Provided that both quantities show discernible charge density dependence, such a correlation can be used to identify the limiting spin dephasing mechanism in graphene. The detailed study of such correlation (see Chapter 4) shows that the dominant spin scattering mechanism in single layer graphene is Elliott-Yafet type[27], [45]. The spin transport properties of single layer graphene can be enhanced in high electronic mobility samples. The dominant spin scattering mechanism in bilayer graphene is surprisingly observed to be D'yakonov-Perel[27], [46], [47]. We observe enhanced spin parameters in low electronic mobility samples.

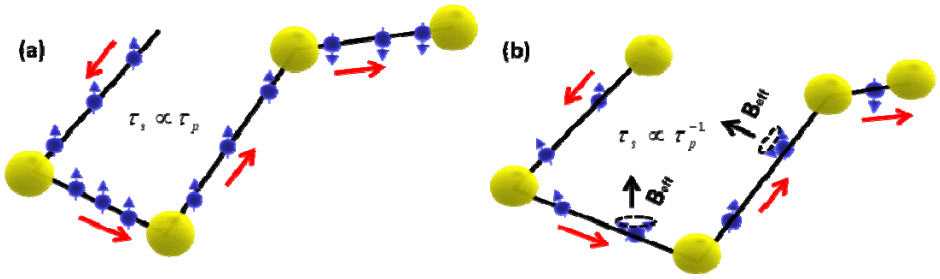

Figure 2-5. The spin scattering mechanisms: The schematics for (a) Elliott-Yafet type spin scattering mechanism and (b) Dyakonov-Perel type spin scattering mechanism.The red arrow represent the diffusion direction of spin current, yellow sphere represent the momentum scattering site, black arrow represent the the direction of effective magnetic field.

2.3 Spin Hall effect

2.3.1 Introduction

Spin orbit coupling (SOC) is the interaction of the linear momentum of particle with its spin angular momentum. While this SOC causes spin relaxation in a material and limits its spin relaxation length, it can also be utilized to manipulate the spin of charge carrier[48]. Spin Hall effect, conversion of the charge (spin) degree of freedom to the spin (charge) degree of freedom, originates from the SOC. The impurities in the material create local potentials and this result in spin dependent scattering of electrons. When un-polarized charge current flows in a nonmagnetic material, the spin up and spin down electrons deflect due to such potentials and the spin up and spin down currents are deflected to the opposite directions. The accumulated spins at the edges of sample create a net spin current perpendicular to the flow of charge current as illustrated in Figure 2-6-(a). Similar to this conversion of the charge degrees of freedom to the spin degree of freedom, the inverse of this effect can also convert the spin degree of freedom to the charge degree of freedom as demonstrated in Figure 2-6-(b). The former phenomena results in the generation of spin current without using the spin dependent ferromagnetic contacts and the latter phenomena can be used for the detection of the signal.

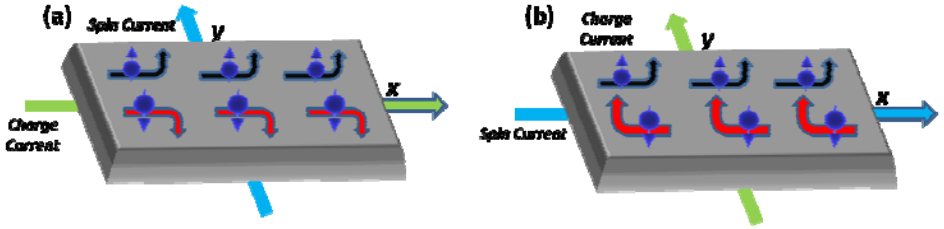

Figure 2-6. Spin Hall effect: (a) Charge current induced spin Hall effect and (b) Spin current induced spin Hall effect.The red and black arrows represent the motion direction of scattered charges, the blue arrow represent the the direction of spin. Turquoise (green) arrow represent the flow direction of spin (charge) current.

2.3.2 Generation and detection of spin current via SHE

SHE is a reliable method to generate spin current and the its inverse effect can be utilized to detect the signal. The schematic of such SHE measurement is shown in Figure 2-7-(a). The charge current is injected from the metallic source electrode 1 to drain electrode 3. The presence of sufficient SOC results in the deflections of the spin-up and spin-down electrons to the opposite directions. This conversion of charge degree of freedom to the spin degree of freedom is illustrated in Figure 2-7-(a) with red arrows denoting the flow direction of charge current and blue spheres with arrows represent the flow direction of spin current. This generated spin current is converted back to charge current and the voltage is measured between detector electrodes 2 and 4. The generated spin current can be shown as[34]

$$J_s(x) = \frac{Iw\sigma_s}{2\sigma\lambda_s} e^{-|L|/\lambda_s} \tag{2.11}$$

where σ_s is the spin conductivity, σ is the charge conductivity. This spin current creates a non-local voltage in between leads 2 and 4. The obtained nonlocal resistance depends on the sample dimensions as

$$R_{NL} = \frac{1}{2}\gamma^2 \frac{w}{\sigma\lambda_s} e^{-|L|/\lambda_s} \tag{2.12}$$

spin Hall coefficient ($\gamma = \frac{\sigma_s}{\sigma}$) shows the amount of charge current generated due to spin current. While injected charge current flows between leads 1 and 3, a small fraction of charge current leaks to the material too. This ohmic contribution depends on to the resistivity and the dimensions of the material as: $R_{Ohmic} = \rho e^{-\pi L/w}$. The Ohmic contribution and the SHE signal have different width dependence. While SHE signal depends on width linearly, the Ohmic

signal has an exponential dependence on width. This width dependence can be used to differentiate the contributors of the measured signal.

Similar to the lateral spin valve devices, spin precession measurement can be performed to confirm that signal is originating from spin and obtain the important spin parameters. For this purpose we apply an in-plane magnetic field to the direction of charge current flow and we observe an oscillatory behavior as the strength of field increases. Such a spin precession in graphene on WS2 substrate is shown in Figure 2-7-(b) (The detailed discussion is given in Chapter6). The signal fits with the following equation to extract spin dependent parameters[49], [50].

$$R_{NL} = \frac{1}{2}\gamma^2 \rho w Re\left[\left(\sqrt{1 + iw_B\tau_s}/\lambda_s e^{-\left(\sqrt{1+iw_B\tau_s}/\lambda_s\right)|L|}\right)\right] \tag{2.13}$$

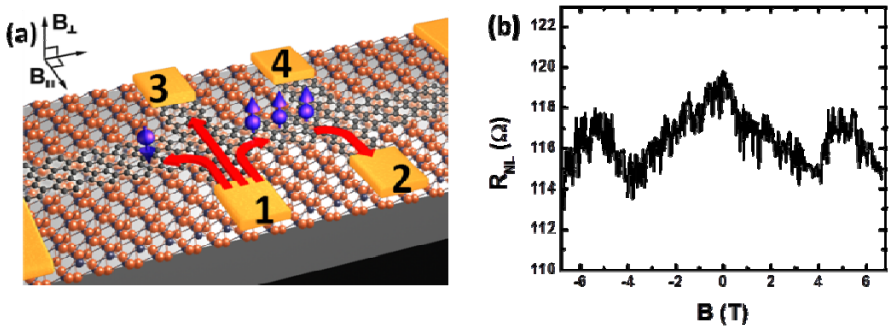

Figure 2-7. Spin Hall effect (SHE): (a) The schematics of SHE configuration. Red arrow represents the flow direction of charge current and blue sphere with the arrow represent the spin current. (b) The modulation of SHE induced spin signal as a function of magnetic field.

2.4 Graphene

2.4.1 Introduction

Graphene lattice consists of carbon atoms that are arranged in hexagon structure on a 2D plane[33]. The lattice of graphene can be regarded as two triangular lattices as shown in Figure 2-8-(a). Each carbon atom shares one in-plane σ bond with its 3 nearest neighboring carbon atoms and these σ bonds ensure the 2D stability of graphene. Each carbon atoms also have an out-of-plane π bonds that are delocalized over the lattice. Graphene owes its unique electronic structure to these π bonds[23].

2.4.2 Band structure of graphene

The band structure of graphene was studied in 1947 by Wallace[51]. Following his tight binding model, the Hamiltonian can be shown as[33]

$$H_K = \begin{pmatrix} \in_A & te^{i\boldsymbol{k}.\boldsymbol{a_1}} + te^{i\boldsymbol{k}.\boldsymbol{a_2}} + te^{i\boldsymbol{k}.\boldsymbol{a_3}} \\ c.c & \in_B \end{pmatrix} \tag{2.14}$$

where $\in_A$ and $\in_B$ are the on site energy of carbon atoms A and B shown in Figure 2-8-(a). t=2.7eV is the hopping energy in between nearest neighboring atoms, $\boldsymbol{a_1} = a(1,0)$, $\boldsymbol{a_2} = a(-1/2, \sin \pi/3)$ and $\boldsymbol{a_3} = a(-1/2, -\sin \pi/3)$ are the positions of these atoms and c.c is the complex conjugate of the off-diagonal matrix element. The eigenvalues of this Hamiltonian is shown in Figure 2-8-(b). The z axis represents the energy and the in-plane axes represent the momentum space on the lattice. Some of the important points in the first Brillouin zone are also shown at the in-plane axes. The valance and conduction bands intersect at K and K' points. These intersection points are known as Dirac Points (DP). In the first Brillouin zone, there are two sets of three DPs; each set is not equivalent with the other sets. The two sets of DPs create a valley degeneracy of $g_v = 2$. The dispersion relation at K and K' points is linear at

low energy. The Hamiltonian at low energy level expanded with $\hbar\vartheta_F = 1ta/2$ can be shown as

$$H_K = \hbar\vartheta_F \begin{pmatrix} 0 & k_x - ik_y \\ k_x + ik_y & 0 \end{pmatrix} = \hbar\vartheta_F \boldsymbol{\sigma}.\boldsymbol{k} \tag{2.15}$$

where $\boldsymbol{\sigma}$ donates the 2D vector of Pauli matrices, **k** is the wavevector. By applying

$$(\hbar\vartheta_F \boldsymbol{\sigma}.\boldsymbol{k})\Psi_K = E\Psi_K \tag{2.16}$$

The dispersion relation at low energy levels of K and K' points can be shown as

$$E_{\pm}(k) \approx \pm\hbar\vartheta_F |k - K| \tag{2.17}$$

This low energy level is described by the Dirac equation for massless fermions. The graphene electrons have a ϑ_F of $1\text{x}10^6\text{cm}^{-2}$.

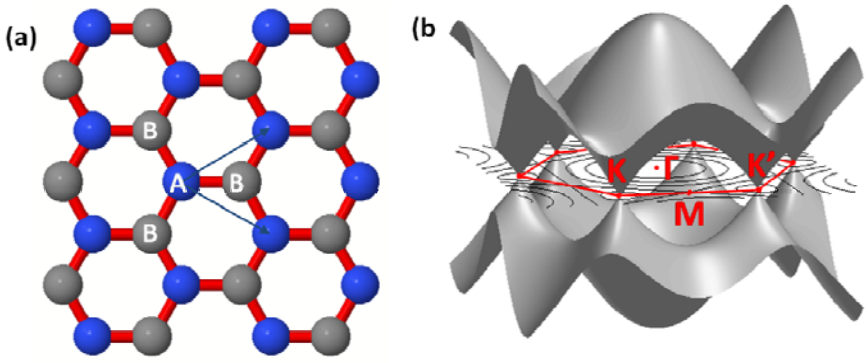

Figure 2-8. The electronic band structure of single layer graphene: (a) The triangular sublattice of graphene. Each A atom has three nearest neighbours carbon atom of B. (b) The band structure of graphene with the first Brillioun zone.

2.4.3 Electronic properties of graphene

The linear dispersion shown in previous section leads to the unique electronic properties of graphene. Since valance and conduction bands intersect at DP, graphene does not have a finite band gap. While this is an obstacle for transistor applications, this property leads not only tuning the charge carrier type between hole and electron but also it changes the charge carrier concentration. The application of an electric field tunes the Fermi energy (ε_f) as[52]

$$\varepsilon_f = \hbar v_f \sqrt{\pi n} \tag{2.18}$$

where n is the charge carrier concentration. The carrier concentration in graphene can be tuned with the application of a gate voltage through SiO_2 gate.

$$n = \frac{\in_0 \in V_g}{te} \tag{2.19}$$

where $\in_0 \in$ is the permittivity of SiO_2, t is the thickness of SiO_2 and V_g is the applied back gate voltage. The Fermi level is expected to be located at DPs and the resistivity (conductivity) of graphene decreases (increases) suddenly with the application of back gate voltage. The application of a positive (negative) back gate voltage brings the Fermi level in conduction (valance) band and the density of electron (hole) charge carriers increases as back gate voltage increases. This results an increase (decrease) in the resistivity (conductivity) of graphene. The charge carrier density dependence of graphene resistivity is shown in Figure 2-9. The electronic charge mobility (μ) is calculated from the Drude formula[41]: $\mu = \frac{\sigma}{en}$

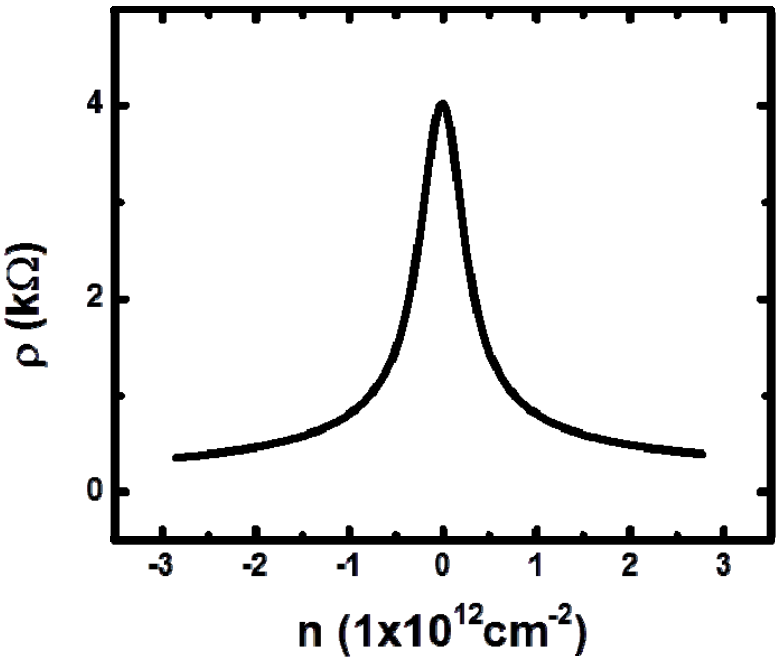

Figure 2-9. The resisitivity of graphene as a function of charge carriers. The charge carrier type and density are tuned with an application of back gate voltage from Si/SiO_2 gate electrode.

The fabricated graphene devices in this thesis have diffusive transport characteristic. The charge diffusion constant (D_c) can be obtained from Einstein relation as

$$D_c = \frac{\sigma}{e^2 v(E)} \tag{2.20}$$

The density of states ($v(E)$) in 2D graphene is related to the energy (E) as[45]

$$v(E) = \frac{2\pi g_v g_s |E|}{h^2 {v_F}^2} \tag{2.21}$$

The E can be extracted in terms of number of carriers as

$$E = h\vartheta_F \sqrt{\frac{n(E)}{g_v g_s \pi}} \tag{2.22}$$

So the D_c can be finally shown as

$$D_c = \frac{\sigma}{e^2} \frac{h\vartheta_F}{\sqrt{g_v g_s \pi n(E)}} \tag{2.23}$$

Since D_c and momentum relaxation time (τ_p) has the following relation

$$\tau_p = \frac{2D_c}{{\vartheta_F}^2} \tag{2.24}$$

τ_p can be shown for single layer graphene as

$$\tau_p = \frac{\sigma}{e^2} \frac{h}{\vartheta_F \sqrt{g_v g_s \pi n(E)}} \tag{2.25}$$

In bilayer graphene, the τ_p can be derived by using the Boltzman theory [53]

$$\tau_p = \frac{\sigma m^*}{ne^2} \tag{2.26}$$

where m^* is the effective mass ~ $0.03m^e$. τ_p has *n* dependence in both single and bi-layer graphene. Unlike single layer graphene, the energy momentum dispersion in bilayer graphene is quadratic. A finite band gap can be opened in bilayer graphene with the application of an electric field.

2.4.4 Electronic transport in graphene under magnetic field

In classical picture, if a conducting material is placed under magnetic and electric fields, the charge carriers with a velocity of $\boldsymbol{v}$ feel the Lorentz force of

$$\boldsymbol{F}_L = \pm e(\boldsymbol{E} + \boldsymbol{V}x\boldsymbol{B}) \tag{2.27}$$

and they are deflected to the edge of the material[33], [54]. In Hall bar geometry, this accumulation will raise a transverse potential, V_{xy}. The transversal resistivity (ρ_{xy}) is linear with applied perpendicular magnetic field (B_z).

$$\rho_{xy} = \frac{V_{xy}}{I_{xx}} = \frac{B_z}{n_s e} = B_z r_H \tag{2.28}$$

where $r_H = \frac{1}{n_s e}$ is the Hall coefficient. This measurement is performed in conducting materials to determine the type and density of charge carriers. The Hall Effect measurement at low B_z range is also a reliable method to extract the electronic mobility of a conducting material. The mobility (μ) can be calculated as $\mu = \frac{r_H}{\rho_{xy}}$. The longitudinal resistivity (ρ_{xx}) is independent of B_z, it just depends on the sample dimensions.

$$\rho_{xx} = \frac{W}{L} = \frac{V_{xx}}{I_{xx}} \tag{2.29}$$

In 2D materials, ρ_{xy} has quantized conductance and ρ_{xx}vanishes in high mobility samples at low temperature under high external magnetic fields. This Hall effect is known as quantum Hall effect (QHE). The universal quantized steps in ρ_{xy} has the following sequence: $\rho_{xy} = \frac{h}{ve^2}$ where h is the Planck constant, e is the charge and v is an integer. Since these quantization values

depend on universal constants of h and e, it is very reliable and it is used as primary standard of resistance[54].

The observed quantization arises because of the Landau Level quantization. The application of high magnetic field decreases the size of cyclotron orbit and it becomes comparable to the wavelength of charge carriers. If the mobility of the measured material is sufficiently high, the momentum scattering time increases and it allows the charge carrier to complete a few cyclotron orbits before they relax. The size of orbit only takes some allowed numbers. The quantized cyclotron orbit results in discrete levels of density of states. This is called Landau Level and has only allowed energies for cyclotron orbits under quantization conditions. These levels can be completed with the application of magnetic field perpendicular to the plane of conducting material. Because of the presence of disorder in the system, Landau Levels broaden. If the Fermi Level aligns to the center of a Landau Level with the application of magnetic or electric field, the plateaus in ρ_{xy} and the vanishing of ρ_{xx} are observed. The number of completed Landau level equals to the number of localized carriers per total density of charge carriers. The half integer QHE in graphene quantizes the transverse resistivity with the following relation[33], [54]

$$\rho_{xy} = \frac{B}{en_s} = \frac{h}{4e^2(N + \frac{1}{2})} \tag{2.30}$$

where N is the integer number including zero.

In bilayer graphene case, the quantization takes the form of

$$\rho_{xy} = \frac{h}{4e^2(N)} \tag{2.31}$$

where N is the integers excluding zero. QHE measurements can be used as a direct tool to determine whether graphene is single or bi-layer. QHE can be realized in two-dimensional electron gas (2DEG) systems too. The main differences between these two different systems are:

1- The Landau Levels in graphene can take two times more charge carriers than the LL in conventional 2DEG materials. This property is a consequence of valley degeneracy in graphene at K, K' points.
2- The energy spacing of consecutive LLs depends on magnetic field (B) as $\sqrt{B_z}$ in graphene, whereas it scales directly proportional to B in conventional 2DEG materials.

In diffusive transport, quantum interferences give a correction to the Drude conductivity. The motion of two electrons in opposite directions around a closed loop and finally their intersection at the starting point result in a constructive interference if wave functions have the same phase and their phases don't change during the propagation[55]. These charge carriers have a delay due to propagating around the loop and as a result, the resistance of material increases. This constructive interference phenomenon is known as Weak Localization (WL). In graphene case, the presence of Berry phase results in a destructive interference and weak anti-localization (WAL) is expected. The WAL in graphene is suppressed and the presence of short range scatterers restores WL effect. Such quantum interfering effect can be realized experimentally by destroying the phase difference between the wave functions of electrons with the application of magnetic field. In the WL case, the conductivity of material decreases whereas in WAL case the conductivity increases. In graphene, the change in conductivity takes the following term

$$\Delta\sigma(B) = \frac{e^2}{\pi h}\left[F\left(\frac{\tau_B^{-1}}{\tau_\theta^{-1}}\right) - F\left(\frac{\tau_B^{-1}}{\tau_\theta^{-1} + 2\tau_i^{-1}}\right) - 2F\left(\frac{\tau_B^{-1}}{\tau_\theta^{-1} + \tau_i^{-1} + \tau_*^{-1}}\right)\right] \quad (2.32)$$

where $\tau_B^{-1} = \frac{4eDB}{\hbar}$, D is the diffusion constant, $F(x) = \ln x + \Psi\left(\frac{1}{2} + \frac{1}{x}\right)$, Ψ is the digamma function, τ_i is the intervalley scattering time and τ_* is the intravelley scattering time.

At low temperature, τ_θ is large and the WL effect is dominant. The equation 2-32 at low temperature modifies as

$$\Delta\sigma(B) \approx \frac{e^2}{\pi h} F\left(\frac{\tau_B^{-1}}{\tau_\theta^{-1}}\right) > 0 \tag{2.33}$$

At high temperature, τ_θ is small and the WAL effect is dominant. In this case, the equation 2-32 at high temperature modifies as

$$\Delta\sigma(B) \approx -2\frac{e^2}{\pi h} F\left(\frac{\tau_B^{-1}}{\tau_\theta^{-1}}\right) < 0 \tag{2.34}$$

Such a temperature dependent transition is experimentally shown by F.V. Tikhonenko et al in single layer graphene[56]. In 2DEG systems the presence of spin-orbit coupling results in the WAL[57]. Graphene has weak spin orbit coupling then these conventional materials.

CHAPTER 3 Experimental Techniques

In this chapter, the process details for the fabrication of graphene based heterostructures and spin valve devices are described. The mechanical exfoliation and chemical growth techniques are employed to produce the 2D crystals including graphene. Optical microscopy, Atomic force microscopy (AFM) and Raman spectroscopy methods are utilized to select ideal 2D crystals for further device fabrication. Dry transfer method is used for the transferring of graphene onto arbitrary 2D substrates. Device contacts are formed by utilizing electron beam lithography and deposition techniques including electron beam evaporation and thermal evaporation. Finally, the electronic and spintronics transport properties of devices are characterized with different measurement configurations in a vacuum cryostat chamber.

3.1 Production of 2D crystals

3.1.1 Preparation of mechanically exfoliated graphene

Prior to producing the graphene flakes, Si/SiO_2 substrate is carefully cleaned to have a better adhesion between graphene and substrate. The Si/SiO_2 wafers (Nova Wafers, 6" size, ~0.01ohm-cm resistivity, 300nm dry chlorinated thermal oxide thickness) are diced into 1cm*1cm size first. This is followed by cleaning of wafers in an acetone beaker for 15 minutes with a sonicator to remove the debris and residues. Then, the wafers are kept in IPA bath for 15 minutes and finally wafer is gently dried with nitrogen gas. Graphene is obtained by mechanically cleavage of the highly oriented pyrolytic graphite with a simple method discovered by Manchester group in 2004[22]. This method is known as "Scotch tape" or "micromechanical cleavage". A thick graphite piece is first put onto an adhesive tape (Nitto- BT-150E-KL) and it is continuously peeled until graphite on tape is thinned enough as shown in Figure 3-1. We noticed that a short oxygen plasma treatment to the Si/SiO_2 wafer just before pressing the tape

on it results in larger graphene pieces. The field effect transistors made with these graphene pieces have an enhanced electronic properties compared to the ones fabricated on non treated wafer. Since the strength of van der Waals force in between graphene layers is weaker than the one between graphene and SiO_2 substrate, removing the tape from SiO_2 substrate leaves graphene sheets with a surface area up to 2,000 μm^2 on substrate. While the dimensions of the obtained graphene flake are far below from the size required for practical applications[58], it is big enough to make devices and study its fundamental properties. This simple exfoliation method gives the highest quality crystalline structure among all discovered methods[59].

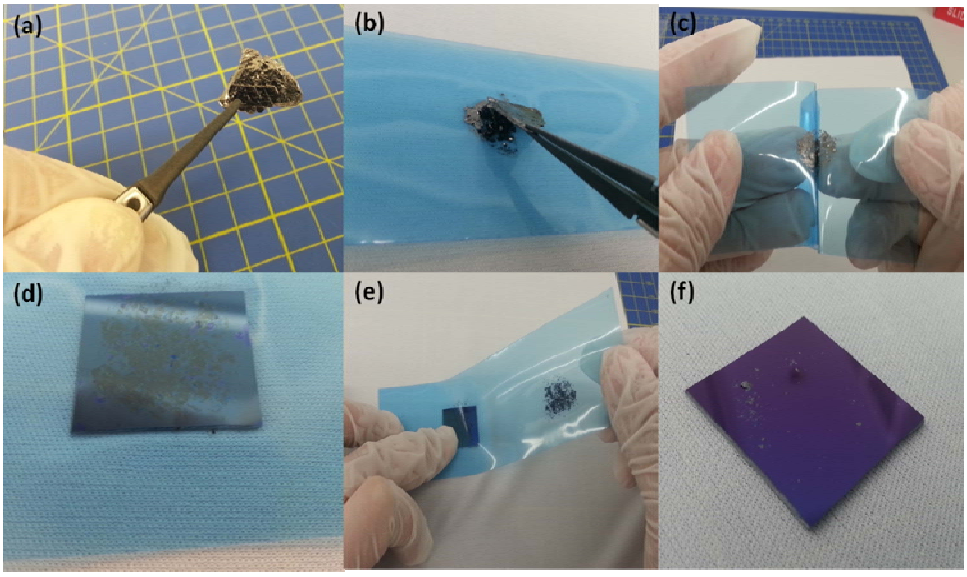

Figure 3-1. The mechanical exfoliation of graphene: (a-f) The steps involved in the production of graphene with mechanical cleavage method using the scotch tape. The same technique is also used to produce thin layers of BN, WS_2, MoS_2, and GaSe.

While single layer graphene is the thinnest material in the world and has an optical transparency of ~ % 98[60], specific thickness of SiO_2 substrate (300nm used in this thesis) creates enough contrast for the identification of graphene

under optic microscopy[61]. With this simple optical characterization method, it is possible to locate and identify the position of graphene on a wafer. For more detailed characterization, AFM and Raman spectroscopy methods can be utilized.

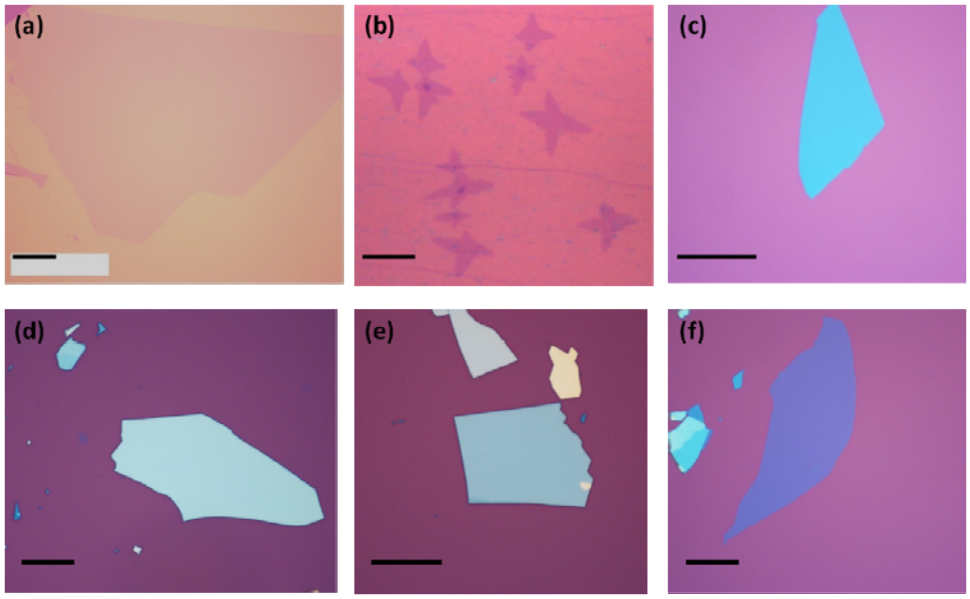

Figure 3-2. The optical images of exfoliated 2D crytsals: Optical images of (a) mechanically exfoliated single layer graphene,(b) CVD grown single-layer and bilayer(flower shape) graphene, mechanically exfoliated thin layers of (c) BN, (d) WS2, (e) MoS2, and (f) GaSe. Scale bars in each image is 10 μm.

Since graphene is a 2D crystal with only one surface, electronic properties of graphene strongly depends on its environment[62]. AFM is very strong tool not only for its surface morphology characterization but also it can determine the number of graphene layers precisely[63]. Raman spectroscopy is another non-contact characterization method that gives detailed information on the doping level, the number of graphene layers, the strain percentage and the defect concentration[64]. There are two main peaks in the Raman spectrum of graphene: G band at ~1580 cm^{-1} and 2D band at ~ 2690 cm^{-1}. The intensity ratio and full width half maxima of these peaks determine the number of layers. For instance, the intensity of G peak is smaller than the intensity of 2D peak for

only single layer graphene. The shape of 2D peak for bilayer graphene is very different than the single layer and multilayer graphene. The full with half maxima and the position of 2D peak are also utilized to determine the number of graphene layers. The doping of graphene and the strain in graphene can be calculated with the shift in the position of these peaks. D peak at ~ 1370 cm^{-1} is absent in high quality crystalline graphene but appears in defective graphene.

3.1.2 Preparation of CVD grown graphene

While mechanical exfoliation method produces very high quality crystalline graphene, the size of flakes are in general limited to a length of ~100 μm and the production yield is low. This scalability and low production yield are problem for the integration of graphene into industrial applications[58]. There are different approaches to grow large area graphene such as epitaxial graphene growth on SiC [65], Chemical vapor deposition (CVD) grown graphene[58][66] and graphene oxide[67] techniques. While SiC graphene and graphene oxide has been widely studied, CVD method is the most promising method for the production of high quality large area graphene with a single layer graphene coverage up to %95[66]. This method simply relies on the flowing of a stock gas containing carbon to the furnace. The hydrogenation process of gas results in the rearrangement of carbon atoms into honeycomb structures on the catalytic surfaces such as Nickel (Ni) or Copper (Cu) at temperatures as high as 1050 C. While this process results in multilayer graphene production on Ni substrate[58], it is possible to grow high quality single layer graphene on Cu substrate with the fine tuning the growth parameters such as pressure, temperature etc[66]. It has been shown that this method can produce CVD graphene on Cu with a grain size up to 1mm[68]. Since most of the graphene based electronic devices rely on back gate voltage, graphene on Cu substrate is transferred onto Si/SiO_2 substrate by following the below simple recipe:

1. Since graphene is grown on both sides of Cu substrate, the graphene at one side of Cu substrate is spin coated with a protective PMMA layer. The graphene on other face is etched with O_2 plasma treatment.
2. The resulting PMMA/Graphene/Cu structure is left in 2% (20g in 1000ml of DI water) ammonium per sulfate (APS) solution with keeping PMMA surface facing up for 12 hours to etch Cu substrate. We notice that while higher percentage of APS solution etches Cu faster, it leaves more residues on graphene compared to low concentration APS solution. After the etching of Cu, PMMA/Graphene layer is gently scooped by using a clean glass slide from APS solution and transferred into the DI water. The layer is kept there for 2 hours in order to remove the APS residues.
3. The floating PMMA/Graphene film on fresh DI water is scooped with Si/SiO_2 wafer. In order to dry the film on SiO_2, the wafer is first kept at 70 C on a hot plate for 20 minutes. It is noticed that higher temperature dries the wafer faster but cracks the graphene more. Finally, the temperature of hot plate is increased to 180 C and sample kept there for 20 minutes to ensure the interface is free of water residues.
4. To remove the protective PMMA layer on graphene, a fresh anisole is poured on the cured $PMMA/G/SiO_2$ wafer first. The re-dissolution of the PMMA tends to mechanically relax the underlying graphene. This increases the adhesion of CVD graphene to the substrate and results in graphene with fewer amounts of cracks and PMMA residues. After taking out the wafer from anisole solution, wafer is dipped into acetone solution. Sample is kept in hot acetone beaker (65 C) for 30 minutes, followed by 5 minutes of IPA treatment. Sample is finally dried with a low flow nitrogen gas.
5. At the final stage, CVD graphene is characterized with optical microscopy to select the ideal area with fewer amounts of wrinkles, residues and ripples for device fabrication.

3.1.3 Preparation of exfoliated 2D crystals beyond graphene

The extraordinary properties of graphene have brought other types of layered materials to the attention of the scientific community. The optimized methods for graphene device fabrication allowed a fast production and characterization of these crystals. There are two main focuses with these 2D crystals beyond graphene: 1- Studying the fundamental properties of the crystals[69]–[73]. 2- Making heterostructure devices with these 2D crystals and graphene to compensate the weakness of graphene or add new functionalization to graphene[59], [74]–[79]. In this thesis, we mainly focus on the graphene-based heterostructure devices with hexagonal BN, WS_2, MoS_2, and GaSe. BN has been utilized in such graphene-based heterostructure devices as a substrate due to its reduced surface charge traps, phonon and improved surface roughness compared to conventional SiO_2 substrate. While BN has very similar lattice constant with graphene (only 1.7% difference), BN has insulating characteristic with a band gap of ~ 5.5eV[80]. The detailed AFM analysis demonstrates that BN has pin hole free, homogenous surface[81]. Graphene field effect transistors fabricated on BN substrates show an enhanced electronic mobility quality, approaching the performance of substrate free, suspended graphene[74], [75], [80]. In addition to this unique crystal, semiconducting MoS_2, WS_2 and GaSe are also widely accepted as promising elements in graphene based heterostructure devices. These are recent members of 2D crystals with a big potential in photovoltaic applications. While bulk MoS_2 and WS_2 have indirect band gaps, the band structures change in the single layers of these materials. The band gap increases and it changes from in-direct band gap to direct band gap[82]. More surprisingly, MoS_2 and WS_2 have high spin splitting band in uppermost valance band up to 0.45meV, making them promising materials for spintronic applications[83]. BN, MoS_2, WS_2 and GaSe flakes are cleaved with the standard method shown in Figure 3-1. Optical microscopy is utilized to select the potential candidate flakes having a ~300 um^2 clean surface area and a height of ~20nm for the device fabrication. This thickness is the most optimum

for serving to graphene as a substrate since it is thick enough to compensate the roughness of SiO_2 and thin enough to make contacts onto these flakes. Figure 3-2 shows optical images of such crystals on 300nm SiO_2 substrate. In order to remove the tape contamination forming during exfoliation process, BN, MoS_2 and WS_2 crystals are annealed in Ar-H_2 atmosphere at 400 C for 6 hours. Finally, these crystals are characterized with Raman and AFM techniques to ensure the surface is free of residue before transferring the graphene onto them.

3.2 Preparing a graphene-based heterostructure device

3.2.1 Introduction

Having an enhanced optical contrast on SiO_2 and lack of any transfer technique restricted the early graphene field effect transistors to be fabricated on conventional SiO_2 wafers. The presence of surface charge traps and phonons limits the electronic quality of graphene[41], [84]. In 2010, a breakthrough for graphene electronics is established by transferring the graphene onto atomically flat hexagonal BN substrate via a wet transfer technique[80]. In this technique, graphene is isolated from SiO_2 wafer with the help of a water soluble layer and transferred onto BN substrate with a manipulator attached to optical microscope. In this section, the transfer method developed in our clean room is described with details.

3.2.2 Dry transfer method

The fabrication steps for transferring the graphene onto 2D crystals are illustrated in Figure 3-3

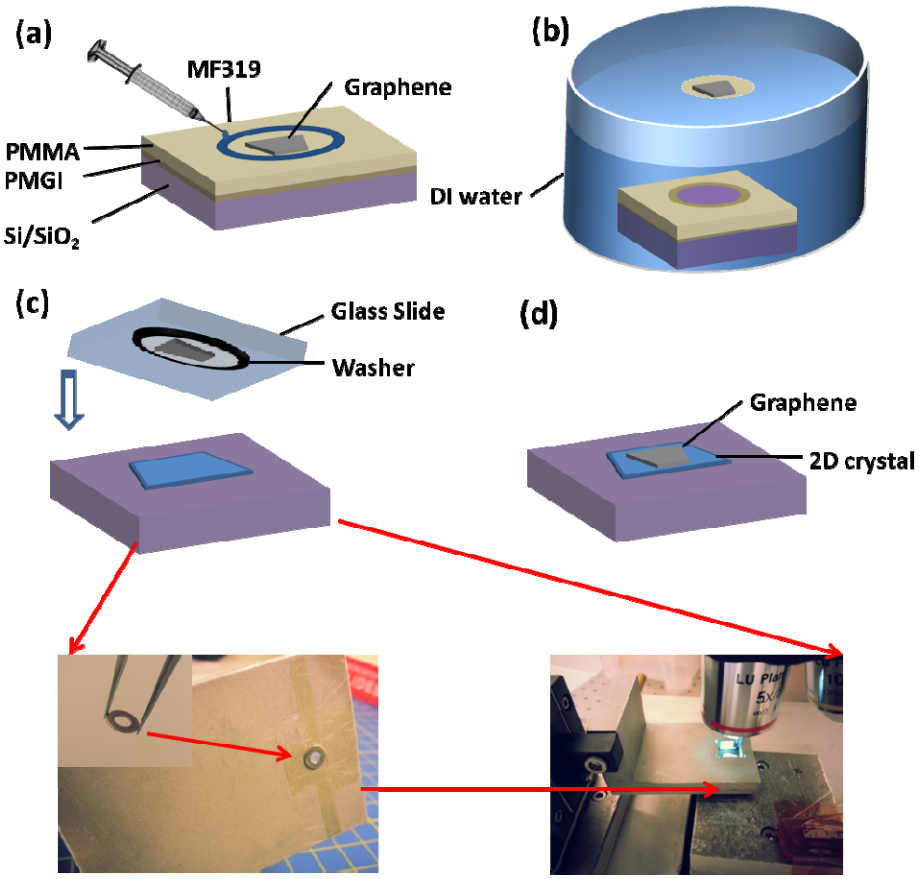

Figure 3-3. The transferring of graphene on arbitrary 2D crystal substrates: The transfer process involves (a) the exfoliation of graphene on PMMA/PMGI bilayer resist stack. MF319 developer removes the PMGI and graphene/PMMA layer floats on surface. (b) Graphene/PMMA layer is cleaned from residues with DI water. (c) Graphene/PMMA layer is scooped with a washer and (d) transferred onto 2D crystal with a support glass slide by using an optical microscope. The inset in (c) represents the optical pictures of washer, transfer slide and the mounting of transfer slide to the system.

The transfer process includes the below steps:

1- PMGI is spun coated at 4000 rpm for 80 seconds onto SiO_2 wafer with a spinner and baked at 130 C for 5 minutes. After substrate is cooled down to room temperature, PMMA (%5, 950K) is spun coated at 4000

rpm for 80 seconds on PMGI layer. The wafer with polymer stack is baked one more time at 130 C for 5 minutes. The total thickness of polymer stack is ~ 400nm. Mechanical exfoliation technique is employed to deposit single layer graphene on the wafer. The reduced graphene optical contrast on polymer is enhanced with using red pass filter.

2- In order to isolate the graphene from the substrate, a circle with a diameter of ~ 5mm is scratched on polymer film with a sharp tweezer (graphene is located to the middle of circle). Bottom resist layer, PMGI, is dissolved carefully with adding MF319 developer to the scratched area for about 15 minutes. Since PMMA is insoluble to this developer, PMMA/graphene stack floats onto the MF319 developer. This process isolates the PMMA/graphene stack from the wafer. The film is then kept in DI water for 5minutes to remove the PMGI and developer contamination.

3- Next, we scoop the floating film from DI water with a washer ring (diameter ~ 4mm). Graphene on PMMA film is located to the center of washer. Film on washer is dried carefully with a clean-room cloth and washer ring is loaded to the custom made washer holder as shown in Figure 3-3-(c). This washer holder is stuck to the manipulator with facing graphene to the ground.

4- The target substrate for graphene transfer is exfoliated onto Si/SiO_2 wafer and characterized with the methods described in section 3.2.2. If the flake has tape residue, it is annealed before the transfer process. Substrate is finally baked with a heater at 85 C for 5 minutes to clean its surface further before the transfer process.

5- Alignment of graphene to the target substrate requires practice. The height of graphene from the substrate is lowered down until it almost touches the substrate. At this height, both graphene and substrate can be distinctly seen under optical microscope. After a final alignment of the

graphene and substrate, the manipulator is lowered down further until substrate starts to move. This means that the washer is contacted to the substrate wafer. At this point, the transferred stack is baked at 80 C for 5 minutes to have a strong adhesion between graphene and substrate. Finally, a sharp needle is used to scratch a circle to the inner diameter of washer to cut PMMA and isolate the transferred wafer from washer. The Washer is lifted up manually with the manipulator and the SiO_2/substrate/graphene/PMMA stuck is further annealed at 130 C for 5 minutes for a stronger adhesion between graphene and the 2D substrate.

6- In order to remove the PMMA film on graphene/substrate/SiO_2, wafer is put in an acetone beaker for 5 minutes. Then, the sample is put into the second acetone beaker and heated on the hotplate at 70 C for 30 minutes to minimize the PMMA residues. Finally the wafer is rinsed in IPA and dried with nitrogen.

3.2.3 Electron beam lithography

The device dimensions are very critical for the observation of various quantum related physical phenomena. For instance, spin transport and ballistic charge transport phenomena are observed in submicron devices[74]. In addition to this, mechanically exfoliated crystals are also in the micrometer range only[22]. These make electron beam lithography very important tool for the fabrication of the submicron size contacts on 2D crystals. In this thesis, Nova nanoSEM-230 system (Figure 3-4-(a)) is used for electron beam lithography and PMMA polymer is used as lithography resist.

For electron beam lithography, the wafer is spin coated with bilayer PMMA resist. The first layer of PMMA (%3, 450K) is spun onto the wafer at 2000 rpm for 80 seconds to produce a uniform resist layer of ~120 nm. The wafer is baked at 170 C for 5 minutes on hot plate to remove the excess solvent. This process is followed by the spinning of the wafer with another PMMA (%5,

950K) layer at 4000 rpm for 80 seconds. The wafer is baked at 180 C for 2 minutes. The total thickness of PMMA is ~450 nm. Bilayer PMMA resist has larger undercut and thickness compared to single layer PMMA. This results in a better lift off process. Electron beam is focused on this polymer to break the polymer chain in the target area. The beam is controlled by the dedicated software (Nabity, NPGS & designCAD). 30kV accelerated voltage is used with an area dose of 450 $\mu C/cm^2$ for the patterning. Sample is developed with MIBK/IPA (1/3) solvent for 1 minute to remove the exposed polymer. This is followed by 1 minute of IPA cleaning to remove the MIBK residues. Lithography process is illustrated in Figure 3-5- (a-b & e-f). Acetone is used to remove the PMMA layer.

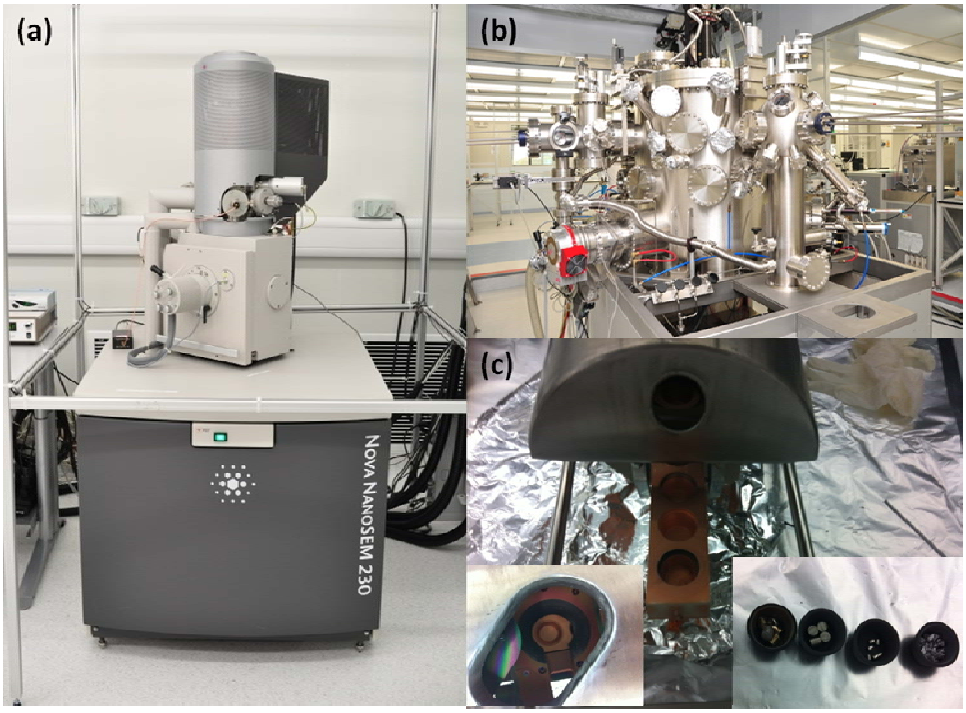

Figure 3-4. The experimental tools for device fabrication: (a) The Nova nanoSEM-230 system is used for the electron beam writing of graphene mesoscopic devices. It provides beam voltages ranging from 1kV to 30 kV. The dedicated patterning software(Nabity, NPGS & designCAD) allowed to generate small size patterns down to few nanometers (b) The UHV-MBE

chamber is specifically designed for the growth of tunnel barriers for spin transport studies. This UHV system uses many pumps including roughing, turbo, cryopump, titanium sorption and ion pumps to maintain an ultra high vacuum in chamber (base pressure is in the low 10^{-10} Torr range) and it is equipped with two high power multi-pocket linear electron beam evaporators(6*8cc capacity and 9Kw), an effusion cell and a thermal source with three boats. The unique rotating arm manipulator of this system can rotate the 2" substrate 360 degree; therefore travel from source to source is possible for sequential deposition cycles with an option to change the height and angle of the sample with respect to deposition source. All these components are controlled via lab view software for remote control. (c) One of the electron beam source in the UHV system with its crucibles, crucible hearth and shutter.

3.2.4 Recipe for heterostructure device fabrication

Graphene based heterostructure devices involve three times electron beam lithography, two times metal evaporation, an etching process and last but not least important four times annealing processes. These processes has to be fine tuned otherwise devices don't show high quality charge transport properties. The device fabrication involves the following steps:

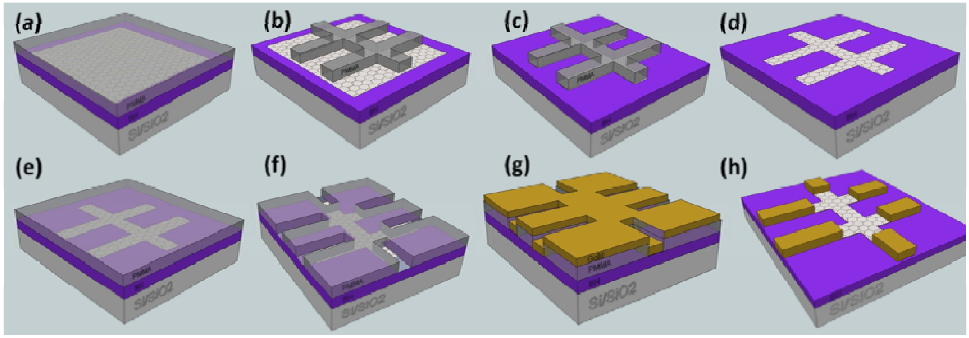

Figure 3-5. The illustration of device fabrication steps for building the graphene based heterostructure devices: (a) Bilayer PMMA is spin coated on the wafer and (b) an etch mask is patterned with electron beam lithography. (c) graphene at the ouside of PMMA mask is ecthed with oxygen plasma and (d) finally

PMMA mask is removed with acetone to finish the graphene patterning process. For creating the metal contacts, (e) a new fresh PMMA is spin coated on patterned graphene, followed by (f) a patterning step with electron beam lithography. (g) Device is evaporated with chromium and gold metals. Thin chromium layer increases the adhesion of gold contacts to the wafer (h) The excess metal is lifted off with acetone and the remaining metals on graphene forms the electrodes.

1. Graphene transfer on atomically flat 2D crystal produces pyramid shape bubbles due to the presence of hydrocarbons at the interface[85], [86]. AFM image of such bubble is shown in Figure 3-6-(a). While these bubbles restrict the available area for device fabrication, it is still possible to find ultra flat regions for fabricating the micron size devices. The annealing of sample after the transfer process moves the small bubbles into the big size bubbles. This process creates larger area for device fabrication as shown in Figure 3-6-(b&c). Effective cleaning is achieved with step annealing under H_2/Ar (1/9) gas flow. In the first step, temperature of furnace is increased to 200 C within 2 hours, and then dwelled at 200 C for 1 hour. After ramping up the temperature to 340 C within 2 hours, sample is annealed for 6 more hours. Finally the furnace temperature is ramped down to room temperature within 2 hours. For effective cleaning, it is very important to keep the furnace tube clean. The annealing set-up used in this study is shown in Figure 3-6-(d). The sample is characterized under the optic microscope and AFM to select the most promising areas for the further device fabrication.

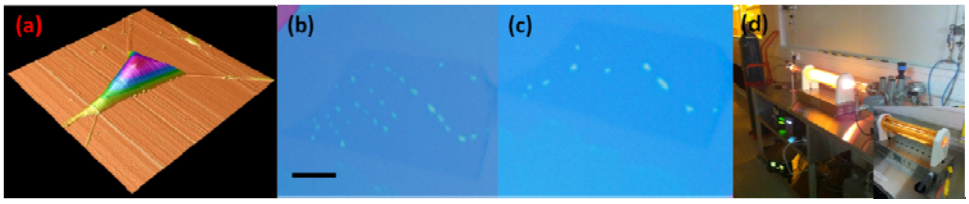

Figure 3-6. Bubble characterization: (a) AFM image of a single bubble. The height of bubble varies from 40 nm to 100 nm and the length of bubble reaches up to 1μm. The darker area shows the graphene on BN substrate and the white dots in the image shows the bubbles. Optical images of a bubbled sample before and after the annealing step are shown in (b) and (c), respectively. The annealing step removes the small size bubbles and create a larger area for the device fabrication. Scale bar is 10 μm. (d) The annealing set-up with a vacuum station. Before Ar/H2 gas is sent to the furnace for annealing process, tube is pumped down for 30 mins.

2. Graphene field effect transistors on 2D crystals are fabricated in Hall bar geometry. In order to know the exact position of graphene with respect to the wafer, alignment markers are patterned by using electron beam lithography followed by a thermal evaporation step. By using these alignment markers, a Hall bar shape PMMA mask is patterned on graphene by using electron beam lithography as shown in Figure 3-5-(b). The excess graphene is etched with oxygen plasma (Figure 3-5-(c)). For etching plasma, 20 W power is applied for 20 seconds while 20 sccm of O2 was flown in chamber. The resulting graphene Hall bar structure (Figure 3-5-(d)) has a length of 3 μm in between Hall contact pairs and has a width of 1 μm. After etching process, the sample is annealed to remove the PMMA resist residues. Samples are scanned with AFM to check the surface contamination level of graphene.
3. Next, the contact electrodes are patterned with electron beam lithography by using the same alignment markers previously used for etch mask writing. This results a high precise alignment between Hall bar leads and contact electrodes. (Figure 3-5-(f)). The width of contact

pattern is 1 μm. Dark field or AFM scanning are used to check the cleanness of patterned channels (we continue the process if root mean square (rms) of channels is less than 0.25 nm).

4. Cr/Au electrodes are formed under high vacuum conditions by using a thermal evaporator. Before actual deposition, both Cr and Au sources are out-gassed. The chamber of evaporator is pumped down until ~ $1x10^{-7}$ Torr. 2 nm Cr is evaporated with a deposition rate of 0.5A/sec for a better adhesion between Au contact and graphene. Next, 100 nm of Au is evaporated with a deposition rate of 1A/sec (Figure 3-5-(g)).
5. Sample is dipped into hot acetone (65 C) for 2 hours for lift off process. PMMA mask is lifted off with the evaporated material on top, leaving Cr/Au contacts only on patterned area. Sample is rinsed in IPA for 1 minute and then dried with nitrogen gas (Figure 3-5-(h)).
6. Sample is annealed to remove the fabrication residues with the recipe in 3.3.4.1.

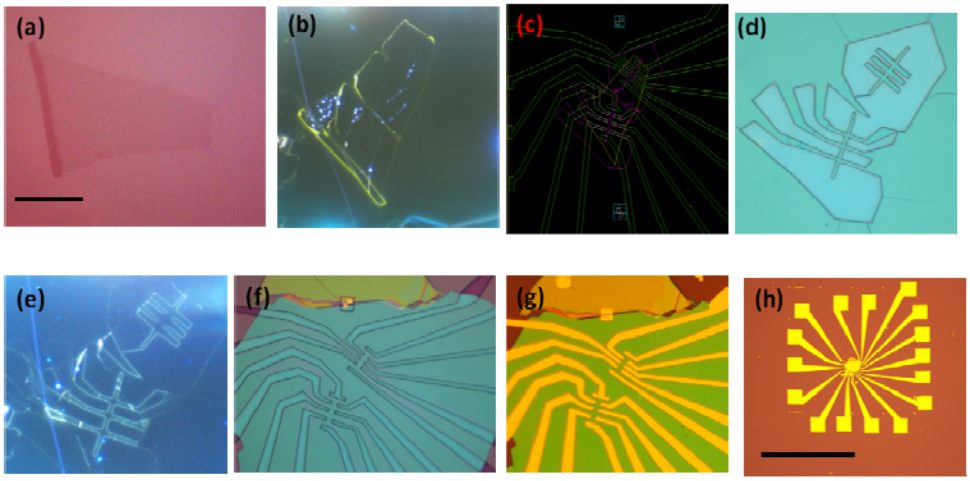

Figure 3-7. Optical images of a fabricated graphene device on boron nitride substrate: (a) Bright field imaging of graphene on PMMA/PMGI polymer stack. Scale bar is 10 μm. (b) Dark field imaging of a transferred graphene on boron nitride substrate after the annealing step. The white spots show the bubbles and the white lines shows the edges of graphene. The bubble free area is selected for

the device fabrication. (c) The designCAD of device with NPGS software for electron beam lithography. Green and purple colors represent the contact and etch mask patterns respectively. (d) Electron beam lithography is utilized to writing the etch mask for patterning the graphene. (e) Dark field imaging of Hall bar patterned graphene on boron nitride. (f) Optical image of device after contact patterning. Scale bar is 500 μm. (g) and (d) represents the final device after annealing process for small and big contacts.

3.3 Preparing a graphene spin transport device

3.3.1 Introduction

Spin injection, transport and detection are the main three criteria for a non-magnetic material to be able to integrated into a spintronics device. Having weak spin orbit coupling and negligible hyperfine interaction raises long spin transport length expectations for graphene[24]. Conductivity mismatch[19] between ferromagnetic electrode and graphene was an obstacle for effective spin injection to the graphene. This problem was solved by introducing a ~ 1 nm Al_2O_3 barrier in between electrode and graphene and resulted in micrometer size spin relaxation lengths at room temperature[37]. In this thesis, we replaced amorphous Al_2O_3 with crystalline MgO crystal and results in such devices are discussed in Chapter 4.

3.3.2 Recipe for spin transport device fabrication

In this section, the device fabrication steps for graphene based spin valve devices are described. CVD graphene based spin valve devices have only an extra etching step compared to exfoliated graphene based spin valve devices. The steps include:

1. Ribbon shape exfoliated single layer graphene is selected for a uniform barrier deposition. For CVD Graphene case, CVD graphene is deposited

on SiO_2 substrate with the method described in 3.2.2 (Figure 3-8-(a)). This CVD graphene is etched into ribbons with electron beam lithography and oxygen plasma processes to prevent the direct electrical shortage between the electrodes (Figure 3-8-(b)). Graphene samples are annealed in Ar/H2 gas mixture at 250C for 3 hours to remove residues.

2. As a next step, alignment markers are written on PMMA for a precise alignment of contacts to etched graphene. Optical images of sample with different magnificent are captured and inserted into design program for contact patterns.

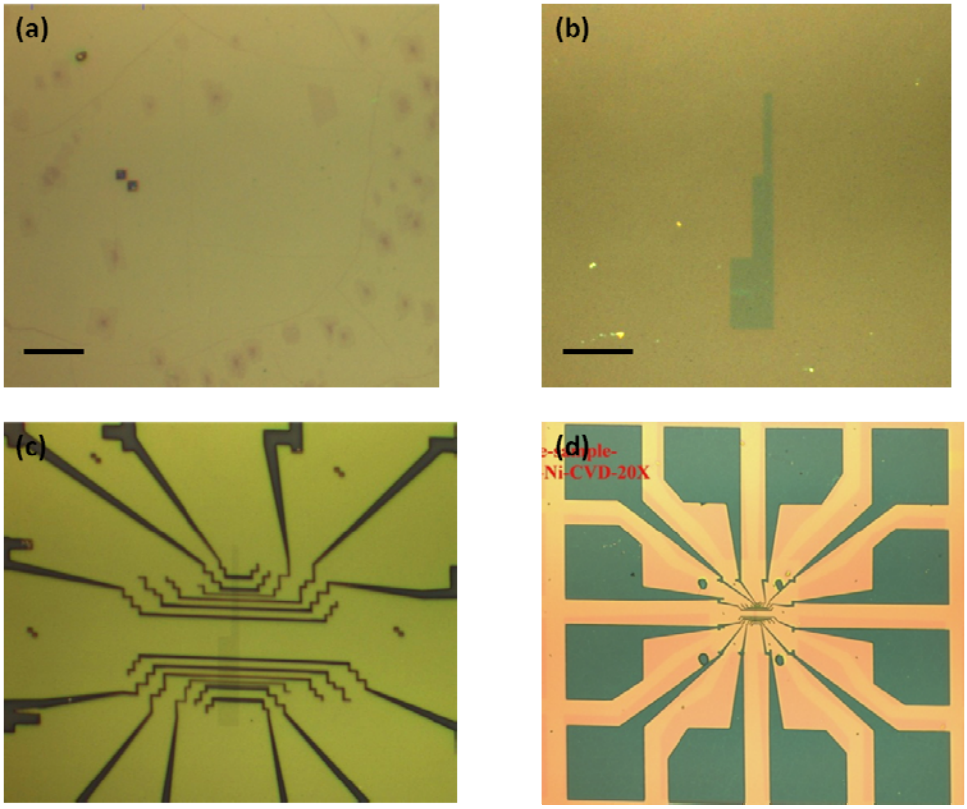

Figure 3-8. Device fabrication for CVD graphene based spin valve devices: (a) CVD graphene is transferred onto 300nm SiO2 wafer after etching the Cu substrate. Scale bar is 10 μm. (b) CVD graphene is etched with Oxygen plasma into stripes with different widths. Electron beam lithography is utilized for patterning the (c) small and (d) big electrode patterns.

3. Electron beam lithography is used to pattern the contact electrode. The previous alignment markers are used before starting the patterning process to have a precise alignment of graphene to the contacts patterns. Sample is developed in MIBK/IPA (1/3) solution for 1 minute, followed by 1 minute of IPA cleaning. Optical images for small and big patterns are shown in Figure 3-8-(c&d) respectively. Since the resistance switching phenomena in spintronics relies on electrodes with different widths, we varied the contact widths from 300 nm to 1.2 μm and a separation of ~1 μm in between contacts with electron beam lithography. A special design with zigzag edges (Figure 3-8-(c)) near contact bars on graphene is patterned to simplify the device fabrication. Zigzag contacts are implemented to stop the domain wall motion in the ferromagnetic electrodes and isolate the contact bars on graphene from the rest of the electrodes. With this geometry, the application of a magnetic field allows the control of the polarization of small leads independently from the rest of ferromagnetic electrodes. Sample is mounted into molecular beam epitaxy (MBE) system for the deposition process. UHV-MBE system used in our laboratory is shown in Figure 3-4-(b).
4. In order to minimize the PMMA residues in patterned channels for uniform MgO tunnel barrier, sample is heat annealed at 100 C for 1 hour in MBE system under ultra high vacuum conditions. After cooling down the sample to the room temperature, ~ 2 nm MgO is evaporated with extremely small deposition rates (0.027 A/sec) by using electron beam evaporator in the MBE system (Figure 3-4-(c)). Base pressure and deposition pressure are ~ $5x10^{-10}$ Torr and ~ $2x10^{-9}$ Torr, respectively. To increase the uniformity of MgO, sample is post annealed at 100 C for 1 hour. We have also another successful approach by depositing a ~ 2nm MgO on bare graphene before any device fabrication. In this approach, we pre- and post anneal the MgO film at 200C for 1 hour.

This is called “global MgO deposition” method. AFM images of such MgO film at the different stage of process are shown in Figure 3-9. I continue with the explanation of the first recipe called “local MgO deposition”.

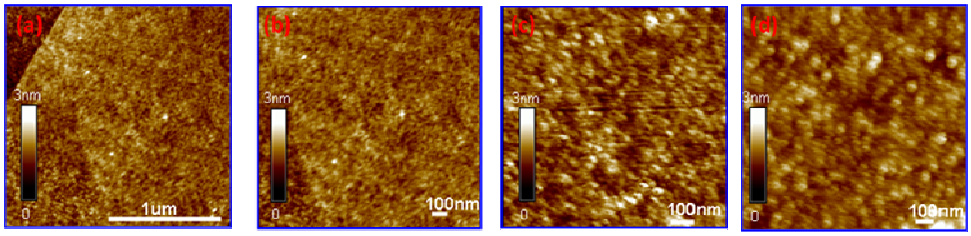

Figure 3-9. AFM scans for the optimized ultrathin MgO tunnel barrier on graphene: (a) Topography of graphene on SiO2 substrate. (b) Topography of graphene after pre-annealing step (200C annealing for 1 hour). (c) AFM image of graphene after the deposition of 1.5nm MgO. (d) AFM image the sample after a post annealing step (200C annealing for 1 hour). The rms values of scans are (a)=0.189nm, (b)=0.208nm, (c)= 0.329nm and (d)=0.221nm.

5. After graphene sample with MgO is cooled down to room temperature from 100 C, 35 nm cobalt (Co) is evaporated with a deposition rate of 0.1A/sec at a deposition pressure of ~ $5x10^{-9}$ Torr. 5 nm of gold capping layer is evaporated on top of Co to prevent the ferromagnetic Co from oxidation.
6. Sample is dipped into hot acetone (65 C) for 2 hours for lift off process. PMMA mask is lifted off with the evaporated material on top, leaving MgO/Co/Au (2 nm/35 nm/5 nm) contacts only on e-beam exposed area. Sample is rinsed in IPA for 1 minute and then dried with nitrogen gas.

3.4 Measurement set-ups and techniques

In this section, I will describe the measurement set-up and characterization techniques for the experiments performed in the thesis.

3.4.1 Measurement set-ups

After the device fabrication is completed, samples are glued onto the 44 pin chip carrier with silver paste. The spin valve devices are carefully located to the chip carrier to ensure that the easy axis of electrodes is parallel to the direction of magnetic field. Aluminum wire is used for the connection between the electrodes on graphene device and the gold paths on chip carrier (West bond wire bonder). Samples are loaded to the rotating probe for the room temperature charge transport characterization. The rotating probe can be pumped down to $1x10^{-6}$ Torr. The probe can be inserted to variable temperature insert cryostat for performing the electronic and spintronics measurements as a function of temperature (1.6 K – 400 K) and magnetic field (0 T - 16T). For transport measurements, a constant ac current at low frequencies (~ 13Hz) is injected to the sample with the standard lock in technique. Back gate voltage is applied with Keithley 6430 source through 300nm SiO_2 dielectric to change the charge carrier density in graphene. All measurements are automated and controlled by IGOR and LabView softwares.

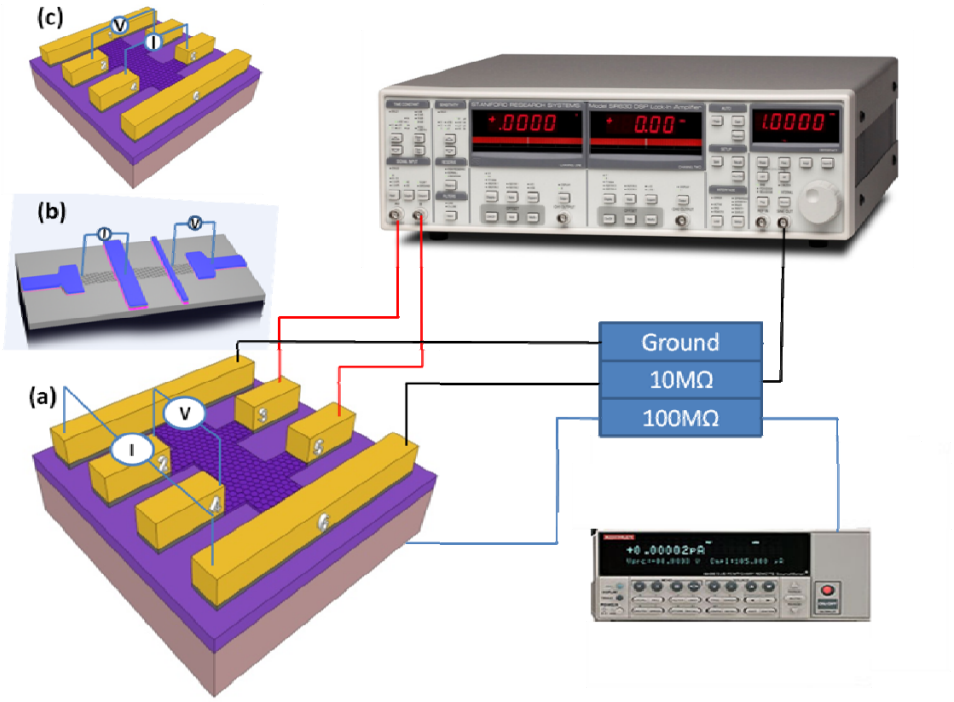

Figure 3-10. Measurement set-up: The lock in (SR 830) is used during all transport measurement performed in this thesis. Keithley 6430 is used to apply gate voltage. The measurement configurations for (a) Hall effect, (b) spin transport and (c) spin Hall effect measurements are shown. *I* represents the injected charged current between source and drain electrodes, *V* represents the measured potential at the interest area.

3.4.2 Charge transport measurements

Before any transport characterization, two probe measurement technique is implemented to characterize the contact resistances. In this geometry, a constant current is sent to device from the source electrode to the drain electrode and potential difference is probed again with the same pair of contacts. The total measured resistance includes the contribution from the resistance of wires, source and drain electrodes and graphene channel. Cr/Au contacts have a resistance in the order of 1 kΩ and MgO based tunnel barrier contacts have a resistance value between 3 - 10 kΩ. 2 probe measurement technique also

specifically points if graphene channel is damaged. Very high contact resistance values and high phase angles (> 10°) are observed if contacts or graphene has problem.

Four probe measurement technique is utilized to measure the graphene resistance without having any contribution from contacts and wires by employing the standard four terminal geometry or Hall bar geometry (Figure 3-10-(a)). In this technique, a current is sent from the source electrode through the drain electrode and potential difference is measured by two separate contacts that are fabricated between source and drain electrodes. The measurement set-up and geometry for such measurement is illustrated in Figure 3-10-(a).

3.4.3 Spin transport measurements

In this thesis, electronic spin transport and spin precession measurements are performed in graphene-based spin valve devices. Ferromagnetic contacts are polarized with the application of an in-plane magnetic field along the easy axis of ferromagnetic electrodes. The charge current is spin polarized while it is injected to the graphene through polarized ferromagnetic injector electrode. Sweeping the in-plane magnetic field changes the relative magnetization directions of the injector and detector electrodes and hence the spin accumulation between the injector and detector electrodes. This leads to a clear bi-polar non-local spin signal with a change in resistance.

Local and non-local geometries have been implemented to observe these spin transport phenomena in lateral spin valve devices. Local geometry has the same configuration with 2 probe geometry discussed in section 3.4.2. It is difficult to differentiate the contribution of spin signal to total signal. Non-local geometry has been utilized to isolate the spin current from charge current flow. The measurement configuration of this geometry is shown in Figure 3-10-(b). Pure

spin dependent non-local voltage is measured between the detector electrode and the reference electrode after sending an ac current of ~ 10 μA.

3.4.4 Spin Hall effect measurements

Spin Hall effect (SHE) is a novel way to create spin current. For SHE measurements, a charge current (~10 μA) is sent from non-magnetic source electrode to the opposite electrode and a non-local voltage is measured with the adjacent opposite contact pairs as shown in Figure 3-10-(c). The resistivity of graphene probed with upper and below electrode pairs has to be the same in homogenous samples and one has to check the homogeneity of sample before measuring the SHE effect to significantly decrease the leakage contribution.

CHAPTER 4 Spin Transport in CVD Single Layer and Bi-layer Graphene

We demonstrate spin injection, spin transport and spin detection in both copper based chemical vapor deposition (Cu-CVD) synthesized single layer and bilayer graphene spin valve arrays[27]. We observe spin relaxation times comparable to those reported for exfoliated graphene samples demonstrating that CVD specific structural differences such as nano-ripples and grain boundaries do not limit spin transport in present samples. Our observations make Cu-CVD graphene a promising material of choice for large scale spintronic applications.

4.1 Introduction

High charge mobility[25], small spin-orbit coupling[23], negligible hyperfine interaction[24], the electric field effect[22] and last but not least the ability to sustain large current densities[87] make graphene an exceptional material for spintronic applications. The demonstration of micrometer long spin relaxation length in exfoliated single layer graphene (SLG) and bilayer graphene (BLG) even at room temperature[37], [45]–[47], [88], [89] and spin relaxation times in the order of nano-seconds may pave the way to realize several of the recently proposed spin based device concepts[90]–[92]. However, for realistic device applications it remains to be seen, if such impressive spin transport properties can also be achieved in wafer scale graphene. Equally important, spin transport studies based on micromechanically exfoliated graphene sheets are often too slow for the quick exploration of the basic spin properties of graphene and for testing potential device architectures. The recent progress in the Cu-based CVD growth of graphene has a strong impact on charge based graphene device applications[66]. However, CVD graphene has a large number of structural differences when compared to exfoliated graphene such as grain

boundaries[58], defects like pentagons, heptagons, octagons, vacancies, 1D line charges[93] and in the case of bilayer graphene possibly interlayer stacking faults[94]. In addition, the current growth and transfer process introduces residual catalysts, wrinkles, quasi-periodic nanoripple arrays and new classes of organic residues[28]. Despite all these defects, charge mobilities in CVD graphene field effect transistors have been comparable to what has been reported for most exfoliated graphene FETs on Si/SiO_2 substrates[95], [96]. Whether this synthesis route will also play an important role for spin-transport studies and large scale spin based device applications depends on how the same defects affect the spin relaxation times. In this chapter, I demonstrate spin transport in Cu-CVD grown SLG and BLG transferred on conventional Si/SiO_2 substrates and discuss the role of nano-ripples, a ubiquitous surface structure of Cu-CVD graphene[28]. Spin transport in CVD graphene is compared with its exfoliated counterpart.

4.2 Spin transport in exfoliated single layer and bi-layer graphene

Prior to the study the spin transport phenomena in CVD graphene, spin transport is characterized with optimized MgO tunnel barriers in exfoliated graphene spin valve devices. In principle, crystalline MgO has coherent spin tunneling[97] compared to amorphous Al_2O_3 barriers that have been utilized at the initial graphene spin valve devices[30], [37], [45]. In this section, I will present the spin transport in exfoliated graphene-based spin valve devices by using MgO tunnel barrier. Towards this, 1.5 nm MgO tunnel barrier and 30 nm Co are deposited in lithographically patterned exfoliated single and bi-layer graphene devices.

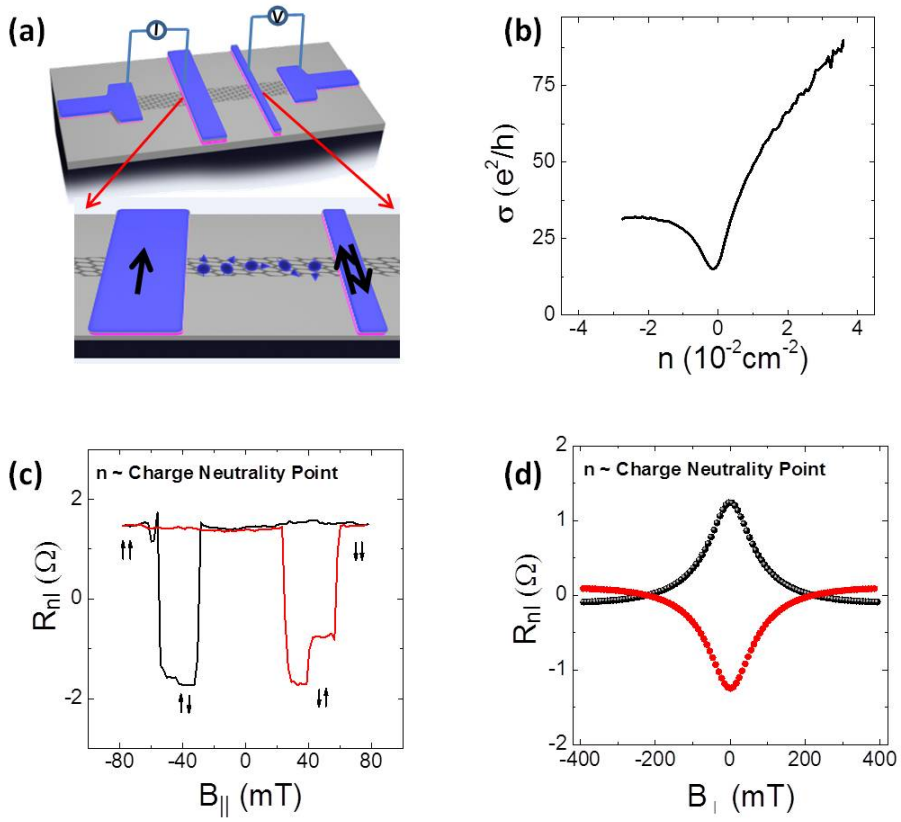

Figure 4-1. Spin transport measurement in exfoliated single layer graphene: (a) Schematics of non-local geometry. The zoomed area shows the schematic for the precession of spin signal under perpendicular magnetic field. Black arrow represent the polarization direction of ferromagnet and blue sphere with the arrow represent the precession of spin. (b) The room temperature conductivity of graphene as a fucntion of charge carrier density (c) Spin transport measurement in non-local gemetry. (d) Out of plane magnetic field dependence of nonlocal spin signal.

The charge transport properties of exfoliated single layer graphene in such spin valve devices are characterized first. Figure 4-1- (b) shows the conductivity of single layer graphene as a function of charge carrier density. We observe a strong distortion on the hole side, similar to the recent report on graphene field effect transistor with ferromagnetic electrodes[98]. Electron and hole mobilities

of 4,350 cm^2/V.s and 1,450 cm^2/V.s are extracted at low charge carrier concentrations. These mobilities are similar to the reported values in graphene-based spin valve devices with Al_2O_3 barrier[30], [37], [45]. Next, we study the spin transport properties of graphene in MgO tunnel barrier based spin valve device by employing the four terminal non-local geometry (Figure 4-1-(a)). A clear bi-polar resistance switching is observed with changing the relative polarization orientations of injector and detector electrodes by sweeping the in-plane magnetic field (Figure 4-1-(c)). In order to confirm that the observed signal is due to spin, not related to spurious effects, spin precession measurement is performed. After keeping the magnetization directions of injector and detector ferromagnetic contacts parallel or anti-parallel with an initially applied in-plane magnetic field, a magnetic field perpendicular to the graphene plane is continuously swept. This resulted in the oscillation of spin signal as a function of magnetic field as shown in Figure 4-1-(d). In order to extract the important spin parameters, the obtained data is fit with the following equation[37]:

$$R_{NL} \propto \int_0^\infty \frac{1}{\sqrt{4\pi D_S t}} exp\left(\frac{-L^2}{4D_S t}\right) exp\left(\frac{-t}{\tau_S}\right) \cos(w_L t)\, dt \tag{4.1}$$

where D_S is the spin diffusion constant, w_L is the Larmor frequency and L is the separation between injector and detector contacts. This fitting gives a spin relaxation time of 103 ps, spin diffusion constant of 0.02 m^2/s and a spin relaxation length of 1.46 μm. These results are comparable to the spin parameters obtained in the Al_2O_3 barrier-based graphene spin valve devices[30], [37], [45].

To determine the spin scattering mechanism of single layer graphene in MgO tunnel barrier based spin valve devices, we study the spin transport properties of single layer graphene as a function of charge carrier concentration and temperature. Towards this, spin precession measurement has been repeated at

different back gate voltages ranged from -50 V to +50 V with a 5 V steps at room temperature. Then, this set of experiment is repeated at each 50K steps while sample is cooled down to 5K from room temperature. The spin diffusion constant, spin relaxation time and spin relaxation length parameters are extracted from the fitting of the spin signal. It is observed that these spin parameters strongly depend on the charge carrier concentration and increase more than % 100 as back gate voltage is increased from charge neutrality point to 40V (Figure 4-2 (a)). Since charge diffusion constant has a linear dependence with spin relaxation length, the dominant spin scattering mechanism is found to be Elliot-Yafet type spin scattering[38]. We note that the observed distortion in charge transport at hole conduction side does not show up in the spin transport measurements at hole side. Spin parameters are symmetric at electron and hole sides. As shown in Figure 4-2-(b), the spin parameters have very small temperature sensitivity.

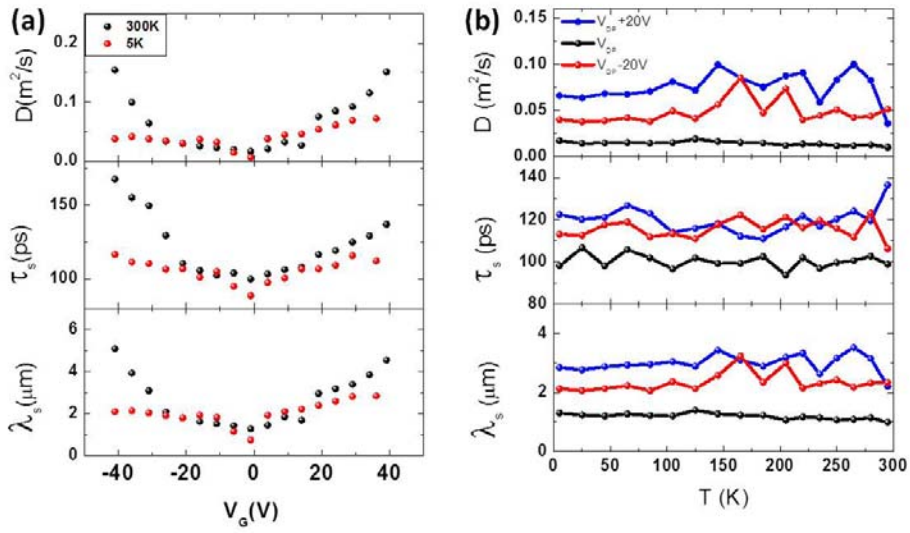

Figure 4-2. Charge carrier density dependent spin transport measurements in exfoliated single layer graphene: (a) Back gate voltage dependence of spin diffusion constant, spin relaxation time and spin relaxation length at 300K and 5K. (b) Temperature dependence of spin diffusion constant, spin relaxation time

and spin relaxation length at different back gate voltages (Vbg=CNP, 20V and -20V)

As a next step, the similar charge and spin transport measurements are also repeated in exfoliated bilayer graphene based spin valve devices. Similar to single layer graphene, a strong asymmetry in conductivity between electron and hole charge carriers is observed. Next, the spin transport measurements in bilayer graphene with MgO tunnel barriers are performed. A clear spin transport and spin precession signals are obtained. Spin relaxation time in bilayer graphene is found to be longer than single layer graphene[46]. The back gate voltage dependency of spin relaxation time in bilayer graphene shown in Figure4- 3. It has the same trend with single layer devices at room temperature. The main difference between single layer and bilayer graphene is observed at the charge carrier density dependent spin relaxation time data at 5K. Unlike room temperature, spin relaxation time is observed to decrease as carrier concentration is increased at lower temperatures and it becomes best noticable at 5K. This behavior is associated to the dominance of Dyakonov-Perel type spin relaxation mechanism[39] in bilayer graphene and discussed in detail in reference[46].

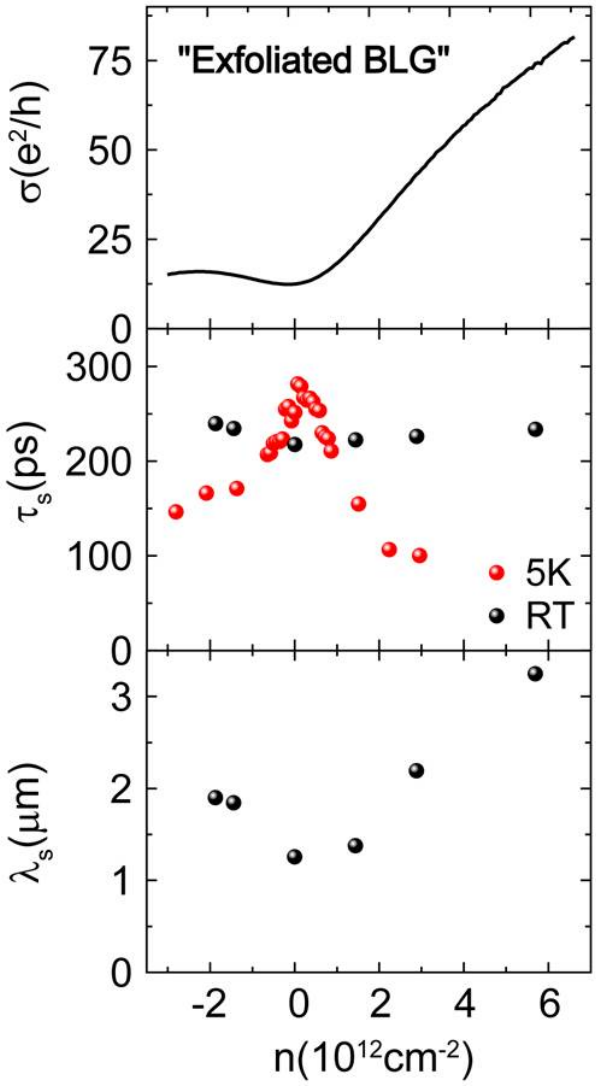

Figure 4-3.Charge carrier density dependent spin transport measurements in exfoliated bi-layer graphene: Carrier density dependence of conductivity, spin relaxation time and spin relaxation length at 300K and 5K.

4.3 Spin transport in CVD single layer and bi-layer graphene

In this section, we study the spin transport properties of CVD grown single and bi-layer graphene. We compared the results obtained in these devices with their exfoliated counterparts.

We followed the growth and transfer of large-scale Cu-CVD graphene by following the recipe described in chapter 3. By controlling the post-growth annealing time of CVD graphene, we can obtain films with SLG coverage up to 95% or additional BLG coverage up to 40%. The latter samples are ideal for directly comparing spin transport in both systems. Figure 4-4-(a) shows the Helium Ion microscopy image of CVD graphene on SiO2 substrate. The darker regions show the CVD bilayer graphene. The cracks in CVD graphene are also visible. The inset in Figure 4-4-(c) shows the optical image of CVD SLG and BLG on a Si-SiO_2 substrate. Raman spectra (Figure 4-4-(c)) with insignificant D-band peak near 1370 cm^{-1} show the high quality of both single-layer and A-B stacked bilayer samples. Spin valves are fabricated by first forming isolated SLG and BLG stripes by means of a PMMA etch mask. A second e-beam lithography step is used to form the device electrodes. Next, we deposit in the same run a ~ 2-nm thick MgO layer followed by 35 nm thick Co electrodes; the details are discussed in chapter 3. This approach allows the batch-fabrication of large arrays of lateral spin-valves with a fast turn-around time well suited for studying device physics. An optical image of a 3 × 5 array of such devices is shown in Figure 4-4-(e) together with a scanning electron microscopy (SEM) image (Figure 4-4-(d)) of multiple spin-valve junctions showing the specific electrode configuration at a single site. The typical length and width of the spin channel in our spin valve devices are in the range of 1 μm to 2 μm. Measurements are performed with standard a.c. lock-in techniques at low frequencies using the local four terminal set-up for charge conductivity measurements and the non-local set-up for spin transport measurements. The schematic of the non-local set-up is shown in Figure 4-4-(f). The spin transport

results obtained from CVD graphene are compared with the results from exfoliated graphene samples of similar charge mobilities prepared under identical conditions[37], [45]–[47], [88], [89].

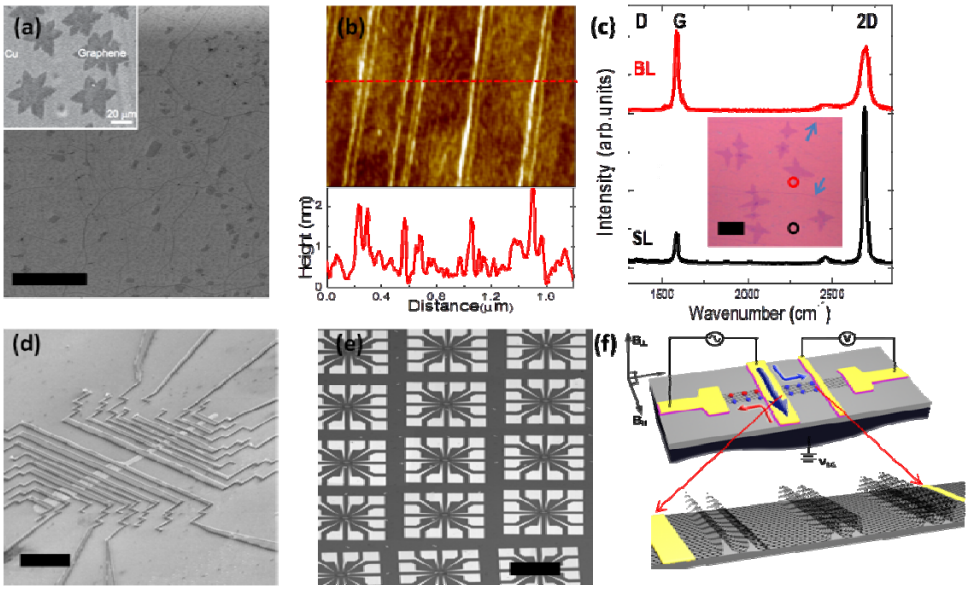

Figure 4-4. CVD graphene-based spin valve fabrication: (a) Helium Ion microscopy image of transferred CVD grown graphene on SiO2 substrate. Inset: Scanning electron microscopy image of sub-monolayer graphene coverage on Cu. The grain boundary size is ~50μm. (b) High resolution contact mode AFM image of CVD graphene after transfer onto Si/SiO_2 wafer revealing the presence localized nanoscale ripples of high density. (c) Raman spectra of CVD single and bilayer graphene on Si/SiO_2 substrate (300 nm SiO_2 thickness) with their optical image. Black and red circles indicate the Raman spectroscopy locations. Blue arrows point to low density wrinkles typical for CVD graphene films. (d) Scanning electron micrograph of CVD SLG spin sample with multiple non-local spin valve devices. Electrode widths range from 0.3 μm to 1.2 μm. (e) Optical image of a 3 × 5 device array. CVD graphene allows the fabrication of large arrays of identical lateral spin valves. (f) Schematics for a graphene based non-local spin-valve together with a possible configuration of quasi-periodic nano-ripples in a spin-valve.

Prior to any spin transport measurements, we characterized the charge transport properties of CVD SLG and BLG in conventional Hall bar devices with Cr/Au contacts. Figures 4-5-(a&c) show the typical am-bipolar field effect[22] in our CVD SLG and BLG devices, respectively. Conductivity scales linearly with carrier concentration and it is symmetric in between electron and hole charge carrier sides. Field effect mobilities $\mu = \Delta\sigma/(e\Delta n)$ are extracted at $n \approx 2 \times 10^{12}/\text{cm}^2$, and vary from 4,000 to 6,000 cm^2/Vs at room temperature. Samples are further characterized at low temperature under high magnetic fields. Both CVD SLG and BLG show the similar quantum Hall effect features as their exfoliated counterparts. Single layer CVD graphene has the anomalous quantization plateau of $(4e^2/h(N+1/2)$ and bilayer graphene has $(4Ne^2/h)$ quantization as shown in Figures 4-5-(b&d), respectively[28], [99] .

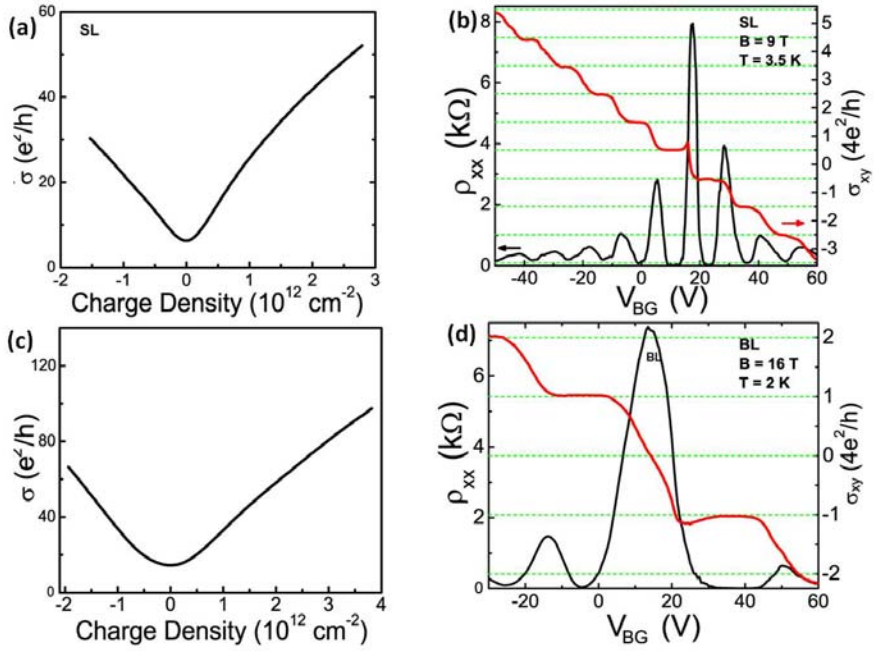

Figure 4-5. Charge transport characterization of single and bi-layer graphene-based devices:(a&c) Charge carrier density dependence of conductivity in single and bi-layer CVD graphene. (b&d) Quantum Hall effect in single an bi-layer graphene.

Prior to the spin transport measurements in spin valve devices fabricated with MgO tunnel barrier, the charge transport is characterized first. A weak electron doping, possibly resulting from the MgO barrier, is observed in all our devices ($n \approx 0$ at $V_{DP} \approx$ -5 V, not shown). In addition, our spin valves show a strong asymmetry between the electron ($n > 0$) and hole ($n < 0$) doped region, such that the conductance in the hole region is strongly distorted (Figure 4-6-(a)). Here, we limit our spin transport analysis mainly to the electron doped region. In total, we have measured spin transport across 15 CVD SLG and BLG non-local spin-valve junctions. Field effect mobilities $\mu = \Delta\sigma/(e\Delta n)$ are extracted at $n \approx 2 \times 10^{12}/\text{cm}^2$, and vary from 1,000 to 2,100 cm^2/Vs. Here we discuss representative CVD SLG junctions and BLG junctions with mobilities of $\approx$ 1,400 cm^2/Vs and $\approx$ 2,100 cm^2/Vs, respectively. While these values are lower than the values in Hall bar devices fabricated with non ferromagnetic contacts[28], they are similar to the values reported for most of the exfoliated graphene based spin valves in the literature[37], [46]. Therefore, this allows a direct comparison of the spin transport properties of CVD graphene with exfoliated graphene.

We first discuss RT spin transport results in CVD SLG near the charge neutrality point (CNP). Sweeping the in-plane magnetic field $B_{\parallel}$ (Figure 4-6-(b)) changes the relative magnetization directions of the Co electrodes and hence the spin accumulation between the injector and detector electrodes. This leads to a clear bi-polar non-local spin signal with a change in resistance of $\Delta R \approx 4\ \Omega$ (Figure 4-6-(b)). The origin of the spin signal is confirmed by conventional Hanlê spin precession measurements. With $L \sim 1.15$ *um* being the separation between the electrodes (center-to-center distance) and ω_L the Larmor frequency we fit our data with the equation 4-1. This gives a transverse spin relaxation time of (τ_s) $\approx$ 180 ps, a spin diffusion constant of $D_s \approx 0.007\ \text{m}^2/\text{s}$ and hence, a spin relaxation length ($\lambda_s = \sqrt{D_s \tau_s}$) of $\lambda_s \approx 1.1$ μm. A clear spin valve signal is also observed for the CVD BLG samples (Figure 4-7-(b)). The origin of the

signal is again confirmed by the Hanlé measurements (Figure 4-7-(c)). Using the same fitting procedure as for the SLG measurements, we obtain for the BLG a spin relaxation time $\tau_s \approx 285$ ps, a spin diffusion constant of $D_s \approx 0.0063$ m^2/s and hence, a spin relaxation length of $\lambda_s \approx 1.35$ µm.

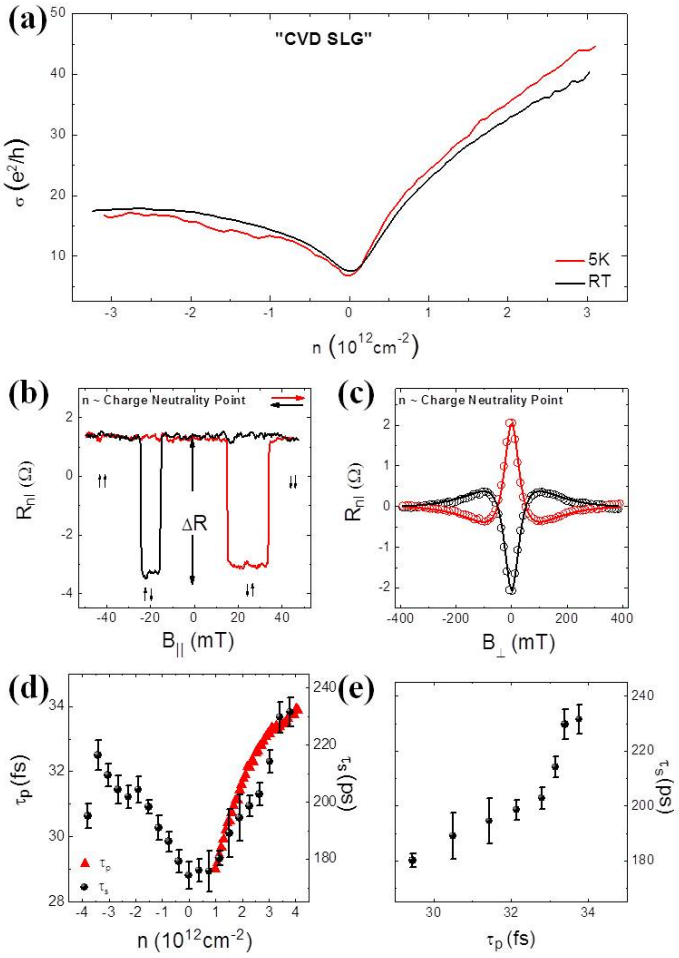

Figure 4-6. Spin transport characterization of single layer graphene-based spin valve device: (a) Conductivity of CVD single layer graphene at RT and at $T = 5$ K as a function of carrier density with a strong asymmetry between electron and hole doped region. (b) Bi-polar spin signal obtained in spin valve device at the charge neutrality point. (c) Hanle spin precession measurement confirms the spin signal obtained in b). (d) The carrier density dependence of momentum and

spin relaxation times. Both quantity increase with increasing electron carrier density. (e) Linear dependence of momentum and spin relaxation times showing that EY like spin scattering is dominant in CVD SLG.

Next, we determine the dominant spin scattering mechanisms in CVD SLG and BLG by evaluating from the functional dependence of τ_s on τ_p. For the Elliott- Yafet (EY) mechanism, spin dephasing occurs during momentum scattering. Therefore, the spin relaxation time is directly proportional to the momentum scattering time ($\tau_s \propto \tau_p$)[38]. On the other hand, the D'yakonov-Perel' (DP) mechanism refers to the case where spin dephasing takes place between momentum scattering events, which may result from random Bychkov-Rashba like spin-orbit fields[42]. This leads to a spin relaxation time, which is inversely proportional to the momentum scattering time ($\tau_s \propto \tau_p^{-1}$)[39]. Away from the CNP, the electric field effect in graphene provides a convenient tool to correlate τ_s and τ_p [45], [100]. Provided that both quantities show a strong density dependence, such a correlation can be used to identify the limiting spin dephasing mechanism as has been demonstrated for exfoliated graphene samples. Using this approach at RT, the dominant spin scattering mechanism for exfoliated SLG spin valves with spin injection through pin-hole contacts has been identified to be of EY type[45]. In exfoliated BLG, the DP type mechanism is dominant[46], [47].

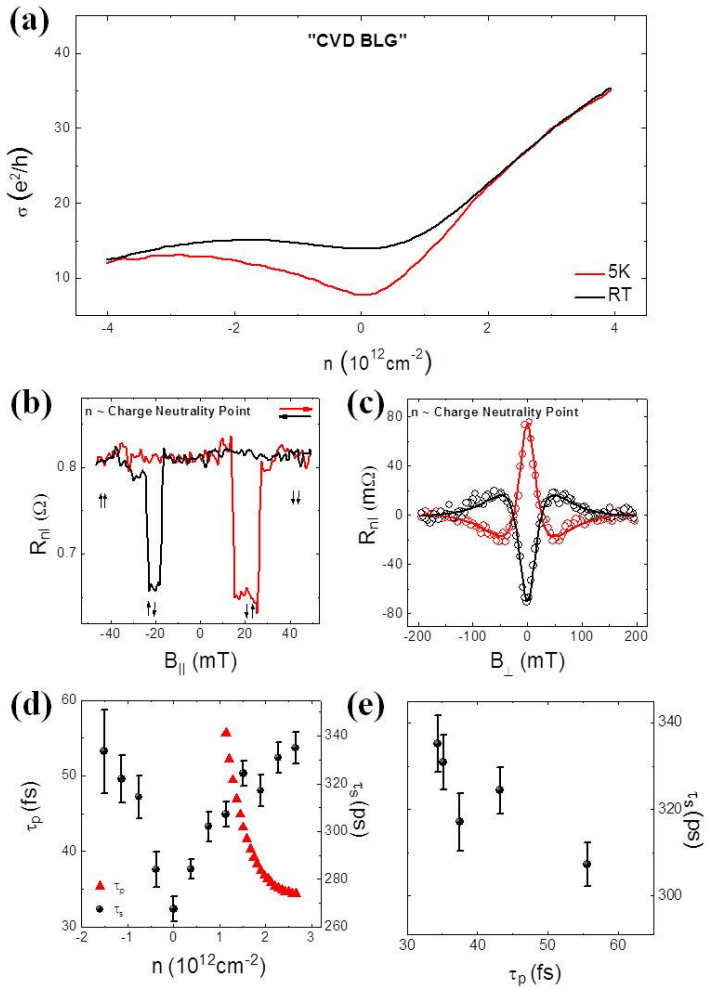

Figure 4-7. Spin transport characterization of bi-layer graphene-based spin valve device: (a)Conductivity of CVD bi-layer graphene at RT and at $T = 5$ K as a function of carrier density. (b & c) Spin valve and spin precession measurements in CVD BLG, respectively. (d) Electron carrier density dependence of momentum and spin relaxation times at RT. (e) Scaling of both quantities indicates DP type spin scattering as the dominant spin scattering mechanism in CVD BLG.

We start our discussion of the Cu-CVD samples with the SLG case and note that τ_s increases with doping by ~ 35% from 175 ps to 230 ps in typical gate

bias ranges. The n dependence of τ_p is extracted from $\tau_p(n) = \frac{h\sigma}{e^2 v_F \sqrt{(n g_s g_v \pi)}}$ within the Boltzmann transport theory framework[100] (Figure 4-6-(d)). Combining both results we obtain an approximately linear scaling of τ_s with τ_p, i.e. ($\tau_s \propto \tau_p$) (Figure 4-6- (e)). In the case of CVD BLG, τ_s increases with increasing n from 265 ps to 335 ps. However, τ_p shows a decreasing trend with increasing n as extracted by $\tau_p(n) = \frac{m^* \sigma}{e^2 n}$, where m^* is the effective mass of the charge carriers (Figure 4-7-(d))[101]. Therefore, correlating τ_s and τ_p, we obtain for BLG an inverse scaling (Figure 4-7-(e)), i.e. ($\tau_s \propto \tau_p^{-1}$). These results summarize the key findings of our experiments: At room temperature the typical spin parameters in CVD graphene differ neither quantitatively nor qualitatively from exfoliated graphene: τ_s, D_s and λ_s, are of same order of magnitude in both systems[30], [37], [45]–[47], [89]. Equally important, their density dependence qualitatively remains the same for exfoliated samples. Hence, the limiting spin dephasing mechanisms at RT remain EY type and DP type in CVD SLG and CVD BLG, respectively.

These results are at first rather surprising, since CVD graphene has additional solvent residues[102], structural differences[93], in particular grain boundaries[58] and nano-ripples[28] when compared to exfoliated graphene. Also, Cu-CVD growth typically requires high temperatures of 1000 – 1050°C. This leads to single-crystal terraces and step edges in Cu (Figure 4-8-(a)), which in turn gives rise to additional nano-ripples in graphene after transfer (Figure 4-8-(b)). They are best seen in high resolution contact mode AFM images after transfer to Si/SiO_2 substrates. Such double peak structures of 0.2 – 2 nm height, ~ 100 nm width and ~ 300 nm separation are quasi-periodic across an area (≥10 μm^2) much larger than the actual spin valve size[28]. Assuming for example a channel area of ~ 1 × 1 μm^2, there will be approximately three such features present independent of their relative orientation with respect to the

ferromagnetic electrodes. Thus, current growth and transfer processes cause local curvature in graphene which may affect spin-orbit coupling. However, it is important to note that the radius of curvatures in CNT and our samples differ greatly. In CNT with a small curvature an enhancement of spin orbit of up to 0.32 meV has been reported[23], [103]. We estimate the curvature induced spin-orbit coupling strength in our nano-ripple samples. Figure 4-8-(c) shows the calculated curvature for such nano-ripples with an average radius of curvature of $R \sim 200$ nm determined by a Gaussian fit of a single AFM trace across a nano-ripple. The smallest curvature of ~ 100 nm is observed at the peak of the nano-ripple. Following Reference [23], we estimate the spin-orbit coupling strength Δ_{curv} as

$$\Delta_{curv} = \frac{\Delta\left(V_{pp\sigma} - V_{pp\pi}\right)}{V_1} x \frac{a}{R} x \left(\frac{V_1}{V_2}\right)^2 \tag{4.2}$$

where Δ = 12 meV, $V_{pp\sigma}$ = 5.38 eV, $V_{pp\pi}$ = -2.24 eV, a = 1.42 Å, V_1 = 2.47 eV, V_2 = 6.33 eV and $R \sim 200$ nm is the radius of curvature of the nano-ripples in our samples. The estimate gives a nano-ripple induced spin-orbit coupling strength of 3.3 μeV. This value is significantly less than the predicted intrinsic SOC in pristine graphene[104], and therefore, in current samples, would not give rise to the limiting spin scattering mechanism. A comparison with the intrinsic spin-orbit coupling of graphene (~ 25 μeV) suggests that the nano-ripples in present samples cannot set a limit for spin transport. Nano-ripples in CVD graphene do have an impact on the charge transport. However, in spin transport the influence of such nano-ripples greatly depends on the curvature in the nano-ripples. However, it should be noted that the size of nano-ripples depends strongly on the various pre-annealing, cooling rate and growth conditions. Thus controlling these growth factors could enable the control of the radius of curvature of these nano-ripples. We estimate that the radius of

curvature needed to affect spin relaxation times of the order of ≤ 10 ns has to be ≤ 30 nm.

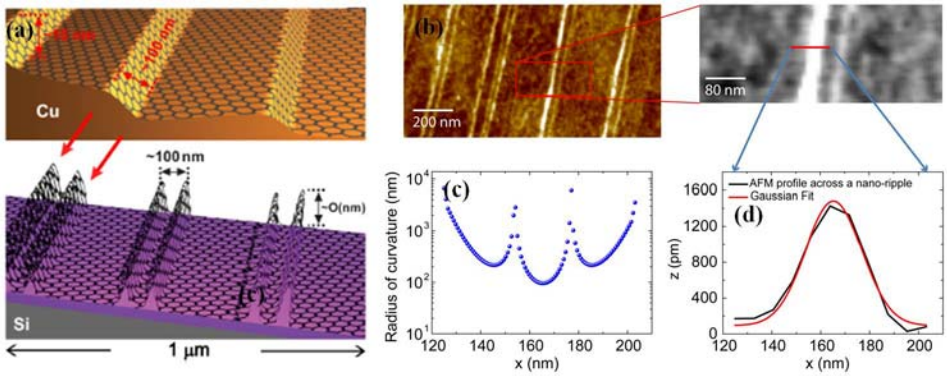

Figure 4-8. Estimate of the SOC strength induced by nanoripples in CVD graphene: (a) The schematics of ripple formation in CVD graphene. The step edges in Cu give rise to nano-ripples in transferred CVD graphene. (b)The AFM image of nano-ripples in Cu-CVD graphene. (c) The Gaussian fit to the nano-ripple for determining the radius of curvature *R*. (d) Radius of curvature determined from the Gaussian fit to the nanoripple.

The high temperature growth of graphene on the Cu surface does however have one advantage. The rather weak interaction with the underlying Cu substrates allows graphene to grow continuously crossing atomically flat terraces, step edges, and vertices without introducing defects[29]. Thus, by controlling pre-growth annealing[66] and fine tuning growth parameters[96], it is now possible to synthesize Cu-CVD graphene with millimeter grain size[96]. The grain size of our Cu-CVD graphene is ~ 50 – 100 μm, as determined by SEM of sub-monolayer coverage graphene on the Cu foil (Inset: Figure 4-4-(a)). This makes spin transport across grain boundaries in sub-micron size spin valves highly unlikely. Thus, under current growth conditions, neither grain boundaries nor nano-ripples, which are the two key differences of Cu-CVD graphene with respect to exfoliated graphene, have a limiting effect on spin transport. The main spin scattering mechanism in Cu-CVD samples seems to originate from the same source as in the case of spin valves based on exfoliated

samples: adatoms[105], scattering from the tunneling barrier interface[106] and the supporting substrate[42].

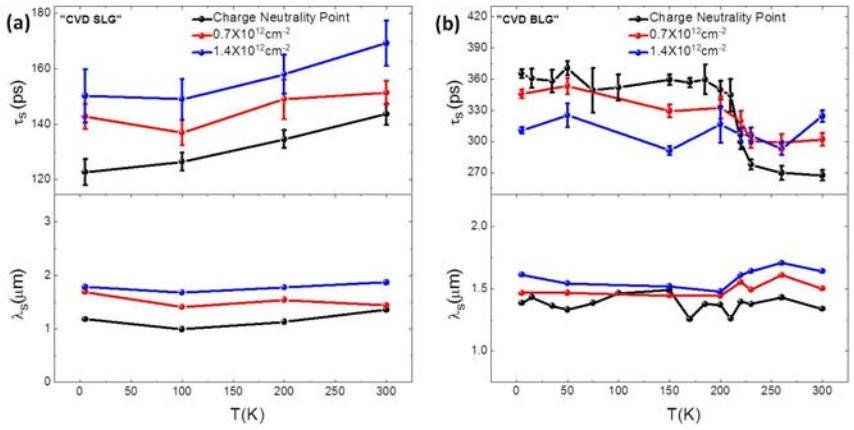

Figure 4-9. Temperature dependent spin transport measurements in CVD single and bi-layer graphene: (a) Temperature dependent spin relaxation time and lenght are shown for CVD grown single layer graphene for three different electron carrier densities. (b) The temperature dependences of spin relaxation time have different behavior at different doping levels in CVD bi-layer graphene. Spin relaxation length depends very weakly on temperature, but its carrier dependence is much weaker than for CVD single layer graphene. Spin relaxation length is observed to be very weakly dependent on temperature for fixed carrier densities in both CVD singleand bi-layer graphene, since different temperature dependence trends of spin relaxation time and spin diffusion constant almost suppress each other in both systems.

Next, we present spin transport measurements as a function of temperature from RT down to 5 K (Figure 4-9). The temperature dependence of τ_s, λ_s and D_s has been measured for three distinct doping levels: 1) at the CNP, 2) at $n \approx 7.5 \times 10^{11}\text{cm}^{-2}$ and 3) at $n \approx 1.5 \times 10^{12}/\text{ cm}^{-2}$. We focus our discussion on the quantity τ_s. In CVD SLG spin valves, similar to results in exfoliated SLG devices[46], we observe at all doping levels only a weak temperature dependence (Figure 4-9-(a)). The CVD BLG, on the other hand, shows a more complex temperature dependence of τ_s, which differs strongly between the CNP and the high carrier

densities (Figure 4-9-(b)). At high doping, τ_s in CVD BLG is only weakly temperature dependent. However, at the CNP τ_s shows a sharp increase from 260 ps to 360 ps between 250 K and 200 K. In contrast, for temperatures above 250 K and below 200 K, τ_s varies again only weakly with temperature at the CNP. This non-monotonic temperature dependence at the CNP is typical also for our exfoliated bilayer devices. Then, we discuss the n dependence of τ_s and λ_s in CVD samples at 5 K. Similar to the RT case, at low temperature (LT) τ_s increases with increasing n in SLG (Figure 4-10-(a)). This implies that in SLG the main scattering mechanism remains of the EY type even at LT. However, in CVD BLG, τ_s decreases with increasing n in contrast to RT (Figure 4-10-(a)). This behavior becomes noticeable for temperatures below 200 K, but is most pronounced at the lowest measured temperature (T = 5K). While this qualitative change of the density dependence of τ_s at low temperature is not yet understood, it is bilayer specific. A very similar behavior has also been observed previously in exfoliated BLG samples[46].

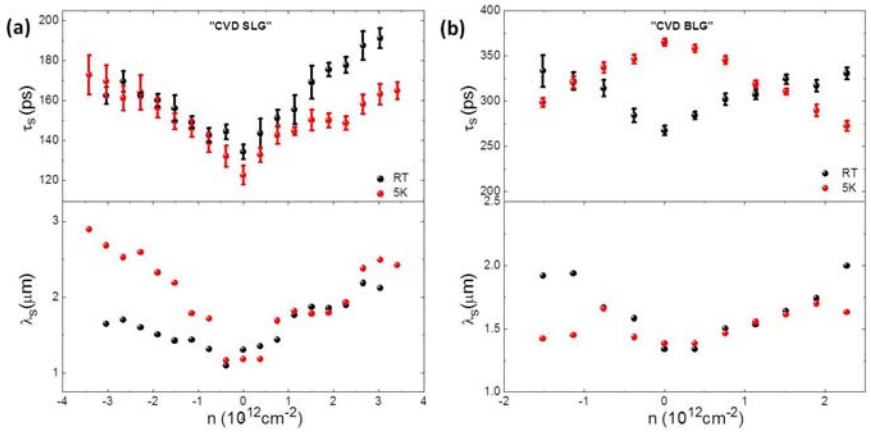

Figure 4-10. Charge carrier density dependent spin transport measurements in CVD single and bi-layer graphene: (a) Charge carrier density dependence of spin relaxation time and spin relaxation length at room temperature and at 5 K for CVD single layer graphene. (b) Charge carrier density dependence of spin relaxation time and spin relaxation length at room temperature and at 5 K for CVD bi-layer graphene. Note that the carrier density dependence of spin

relaxation time of CVD bi-layer graphene at 5 K shows an opposite trend compared to the measurement at room temperature.

Last but not least important, the n dependence of spin signal (ΔR), spin diffusion constant (D_s), and polarization (P) are studied in CVD SLG and CVD BLG samples at room temperature (RT) (Figure 4-11). In CVD SLG, the ΔR is observed to have little variation with the n, a minimum value near the CNP and saturation away from CNP. This behavior is indicative of pin-holes in the MgO barrier[106]. We note that even though we do not use a TiO as buffer layer, we do still obtain a uniform, continuous MgO layer. The D_s shows strong n dependence and increases with increasing n by more than 300% in typical gate bias ranges. The n dependence of P is extracted from $\Delta R = \frac{P^2 \lambda e^{(-L/\lambda)}}{2w\sigma}$, showing very weak n dependence similar to the ΔR. In the CVD BLG, we observe a strong n dependence of the D_s as in CVD SLG. The ΔR and the P in CVD BLG show a distinct behavior on the hole side, but such differences are sample dependent. We attribute the relatively smaller ΔR and P in CVD BLG compared to CVD SLG to the quality of the barrier instead of the number of graphene layers.

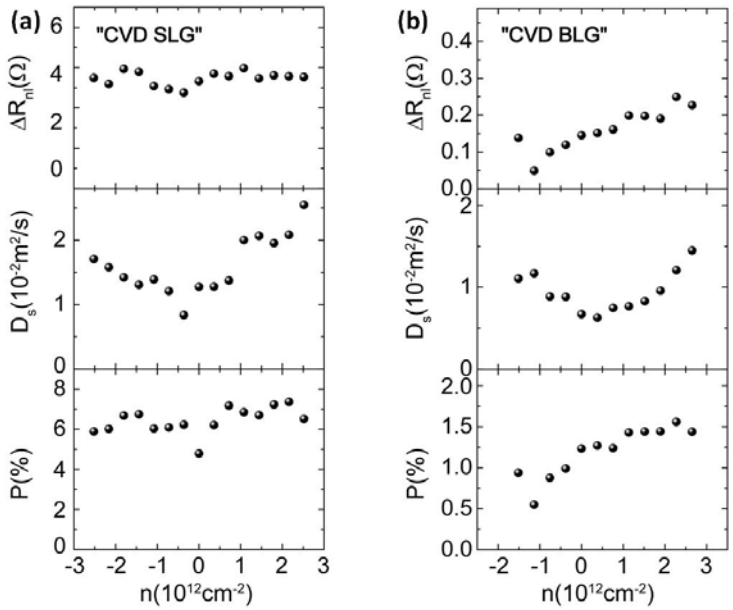

Figure 4-11. Charge carrier density dependent spin transport measurements in CVD single and bi-layer graphene: The carrier density dependence of spin signal, spin diffusion constant and spin polaraziation in CVD (a) single and (b) bi-layer graphene at room temperature.

4.4 Conclusion

In conclusion, we have demonstrated spin injection, spin transport and spin detection in Cu-CVD SLG and BLG samples. The key spin transport parameters such as τ_s and λ_s have been measured as a function of charge carrier density and temperature. They are comparable to our both exfoliated SLG and exfoliated BLG samples making Cu-CVD graphene a promising candidate for possible large scale spintronic applications. We have also discussed the importance of Cu-CVD graphene specific quasi-periodic arrays of nano-ripples in spin transport. While in current samples the local curvature is too small to enhance the spin-orbit coupling significantly, such quasi-periodic nano-ripple arrays may provide intriguing opportunities in controlling spin currents through spin-orbit coupling due to local curvature and local strain.

CHAPTER 5 Substrate Engineering for Graphene-based Heterostructures

While boron nitride substrates have been utilized to achieve high electronic mobilities in graphene field effect transistors, it is unclear how other layered 2D crystals influence the electronic performance of graphene. In this chapter, we studied the surface morphology of 2D boron nitride (BN), gallium selenide (GaSe), and transition metal dichalcogenides (tungsten disulfide (WS_2) and molybdenum disulfide (MoS_2)) crystals and their influence on graphene electronic transport. Atomic force microscopy analyses show that these crystals have improved surface roughness compared to conventional SiO_2 substrate. Graphene field effect transistors on BN, WS_2, and MoS_2 show better electronic quality than their SiO_2 counterparts. While WS_2 and MoS_2 have similar chemical, structural and electronic properties, graphene/WS_2 heterostructures have fourfold higher charge mobility than that of G/MoS_2, making WS_2 an attractive alternative to h-BN substrates. GaSe crystals are less inert to ambient conditions and the density of charge traps on its surface can be probed with graphene. Our results demonstrate the importance of choosing appropriate 2D crystals before building increasingly complex heterostructures.

5.1 Introduction

The extraordinary properties of graphene have brought other types of layered materials to the attention of the scientific community. Isolated new 2-D materials beyond graphene such as WS_2, MoS_2, and GaSe exhibit many exotic electronic[69], optical[70], [71], spintronics[72] and mechanical properties[73]. Recent development in the transfer of these ultra thin planar structures onto each other with precise control offers outstanding opportunities for fundamental and applied studies[80]. For example, the replacement of common SiO_2 substrate with ultra flat BN crystal resulted in a significant enhancement in

electronic mobility of graphene that allowed the observation of room temperature (RT) ballistic transport[74], [75] and fractional quantum Hall effect[76]. Combination of graphene with BN, WS_2 and MoS_2 crystals also help developed new memory and transistor concepts[77][107]. Recently, graphene and WS_2-based heterostructures have been demonstrated in highly flexible photovoltaic devices with extremely high external quantum efficiency[78]. WS_2 was also proposed to enhance the weak spin orbit coupling of graphene with a proximity effect[59]. Since graphene and transition metal dichalcogenides are the most active elements in these heterostructure devices, it is important to understand the impact of these crystals on the electronic properties of graphene before building increasingly complex heterostructures. In this chapter, we studied the surface morphology of conventional amorphous SiO_2, 2-D BN, GaSe, WS_2 and MoS_2 crystals and their influence on graphene electronic transport in order to investigate their potential for future graphene-based complex heterostructure devices.

5.2 Substrate

The observation of two orders of magnitude enhancement of electronic mobility in suspended graphene field effect transistors clearly demonstrates the sensitivity of electronic properties of graphene to the substrate induced scattering sources[25], [108], [109]. Since suspended devices introduce extra complications into the fabrication of devices and restricts the device geometry[25], substrate engineering to the graphene is subject of interest[59]. In addition to these, graphene based heterostructure devices have recently been built to improve the properties of graphene or add new functionalization to it[74]–[79]. However it is important to know the effect of these widely used crystals onto the transport properties of graphene.

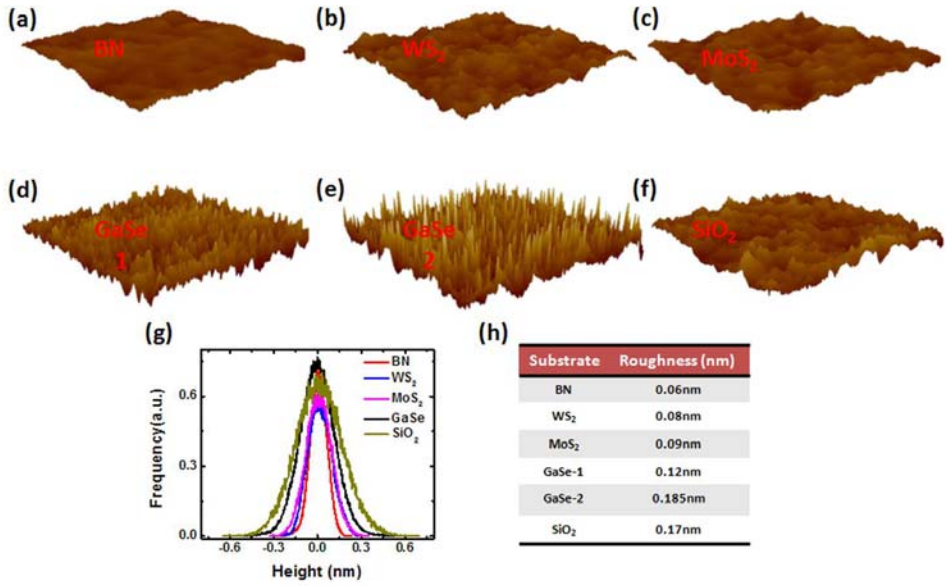

Substrate	Roughness (nm)
BN	0.06nm
WS_2	0.08nm
MoS_2	0.09nm
GaSe-1	0.12nm
GaSe-2	0.185nm
SiO_2	0.17nm

Figure 5-1. Topography images of various 2D crystals: Typical AFM scanning images of (a)BN, (b) WS_2, (c) MoS_2, (d-e) GaSe immediately after exfoliation and 1 day after exfoliation and (f) SiO_2. Height scale of the AFM image is 0-3 nm and scanning dimension is 1μmx1μm. (g-h) Height histogram and rms analysis of the images shown in panels (a-f) respectively.

To study the surface morphology of crystals, micromechanical exfoliation method is employed to deposit relatively thick crystals of BN[110], WS_2[111], MoS_2 (Structure Probe Inc.-SPI) and GaSe (HQ Graphene) on Si/SiO_2 wafers thanks to the weak van der Waals force between adjacent layers in each crystal. Dark field imaging technique is implemented to select the potential candidate flakes of a ~300 μm^2 clean surface area and a height of ~20nm. Figure 5-1 show the typical AFM images of BN, WS_2, and MoS_2 flakes after annealing in Ar/H_2 (9/1) gaseous mixture at 400°C for 6 hours to remove possible tape residues. We noticed that while these crystals are robust to ambient conditions, GaSe crystals corrode at under ambient conditions and corrode faster if the flakes are annealed or kept under strong intensity of light. This observation points that one has to be careful with the environmental control of GaSe-based

heterostructure devices. The AFM images of another GaSe flakes immediately after exfoliation and 1 day after exfoliation (kept in dry cabinet with a relative humidity of %30) without annealing are shown in Figure 5-1(d) and (e), respectively. The height histograms of the crystals are shown in Figure 5-1-(g) and corresponding root-mean-square roughness of corresponding crystals are summarized in Figure 5-1-(h). Figure 5-1-(f) is the AFM image of a conventional SiO_2 substrate for comparison purpose. BN has the flattest surface (~0.06nm) followed by WS_2 (~0.08nm), MoS_2 (~0.09nm), GaSe (~0.12nm), and SiO_2 (~0.17nm). The roughness of a GaSe crystal increases from 0.12 nm to 0.185 nm after only one day, becoming rougher than even SiO2. While rougher substrates create more ripples in graphene that affects the charge transport properties, the presence of charged traps in ultra flat substrate can also dramatically affect it. For instance, it has been demonstrated that the presence of potassium ion traps on mica surface limit the mobility of graphene FETs built on. Since the work functions of these 2D materials and graphene are similar, the charge neutrality point (CNP) of graphene is expected to be located at the center of band gap of these crystals, making them viable alternative substrate to SiO_2 for graphene field effect transistors (FET)[112]. In next section, we study the charge transport properties of graphene on these 2-D crystals as well as conventional SiO2 substrate.

5.3 Charge transport in graphene on various substrates

Graphene has been receiving tremendous attention since the seminal work done by Manchester group[22]. Since graphene can easily be identified on 300 nm SiO_2 substrate with a simple optical microscopy technique and the absence of any transferring technique onto another substrate limited the early charge transport studies only on SiO_2 substrate.

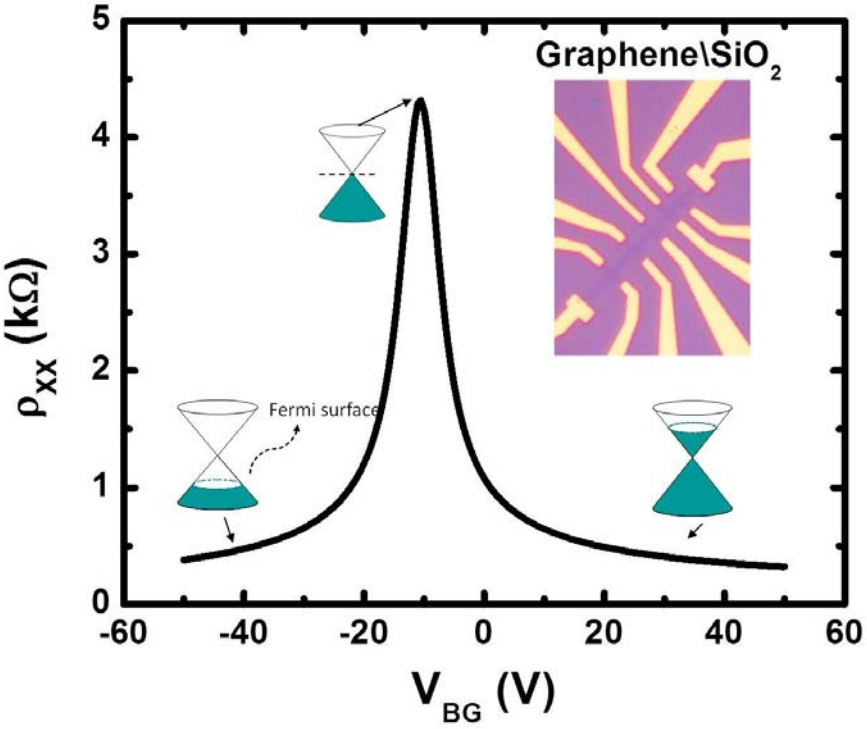

Figure 5-2. Resistivity measurement of a graphene field effect transistor on SiO_2 substrate as a function of back gate voltage at room temperature. Inset: A completed graphene Hall bar device on SiO_2 substrate. The schematics represent the positions of Fermi surface at different back gate voltages.

SiO_2 is a commonly used dielectric material with a dielectric constant of 3.9 and allows the application of an electric field perpendicular to the graphene plane[22]. Graphene has a unique band structure with a linear dispersion relation[51]. This unusual band structure leads to an exceptional electronic characteristic in graphene. The valance and conduction bands touch each other at K point in Brillouin zone and Fermi level is expected to be located at intersection point known as charge neutrality point without any doping[52]. The presence of electron hole puddles[113] and thermally generated carriers lead a finite resistance at CNP[114]. Figure 5-2 shows the back gate voltage dependence of graphene resistivity on such conventional SiO_2 substrate. The

application of an electric field tunes the charge carriers between electrons and holes. Positive (negative) back gate voltage through SiO_2 dielectric shifts the Fermi level to the conduction (valance) band and induces electron (hole) charge carriers. By changing the gate voltage, resistivity of graphene rapidly decreases away from the CNP. Charge carrier density can be tuned typically from ~ $1x10^{11}cm^{-2}$ to ~ $1x10^{13}cm^{-2}$ with varying the gate voltage[22]. The absence of a band gap in single layer graphene limits the integration of graphene into the transistor applications due to low on/off ratios[115].

Charge mobility is an important parameter for especially semiconductor materials. It demonstrates how quickly charge carriers can move under the influence of an applied electric field. Graphene has exceptionally high electronic mobilities compared to technologically used materials due to its unique electronic spectrum. The electronic mobility of graphene can be calculated with the derived version of Drude formula,$\mu = \frac{1}{e}\frac{d\sigma}{dn}$, where σ is the charge carrier conductivity, *e* and *n* are the electron charge and density of charge carriers. The mobility of sample shown in Figure 5-2 is calculated to be 7,000 $cm^2/V.s$ at high charge carriers. The electronic mobility in graphene on SiO_2 substrate found to vary from 5,000 to 10,000 $cm^2/V.s$ and insensitive to temperature. Density independent mobility that excludes the contribution from Coulomb scattering can be calculated with the following equation[80]:

$$\sigma^{-1} = \left((ne\mu) + \sigma_0\right)^{-1} + \rho_s \tag{5.1}$$

where σ_0 is the conductivity at CNP and ρ_s is the resistivity due to short range scattering. A density independent mobility of ~ 9,000 cm^2/Vs is extracted for the device shown in Figure 5-2. While these calculated mobilities are still remarkably high compared to common semiconductors[33], mobility of graphene was predicted to be exceeding 200,000 cm^2/Vs[116].

In contrast to perfect graphene, the experimental charge transport in graphene suffers from the structural defects[117], substrate induced Coulomb[80][84] and phonon scattering sources[44], ripples[118] and fabrication residues[119]. These scattering sources alter the electronic properties of graphene by reducing the electron free path in graphene. For instance, Chen et al. showed that doping of graphene with potassium adatoms decreases the mobility and minimum conductivity of graphene[41]. This interesting result suggests that Coulomb scattering sources are the main limiting factor for charge transport in graphene. The observation of extremely high electronic mobilities in suspended graphene points that the substrate induced scattering is the main limiting source for the charge transport in graphene[25], [108], [109]. Since the device yield is very low in such suspended devices, substrate engineering with less trapped charges and reduced surface roughness is a promising way to improve the electronic mobility of graphene.

Towards this, we first characterized the charge properties of a graphene device on atomically flat BN substrate. Compared to graphene on a SiO_2 substrate, graphene on a BN substrate has been shown to have smaller impurity doping level and higher charge mobilities which is attributed to reduced surface roughness and surface charge traps[74], [75], [80]. Figure 5-3-(a) shows the V_{BG} and temperature dependence of the graphene resistivity as determined from $\rho = {Rw}/{l}$ where w is the width of graphene channel and l is the spacing between electrodes. Several features of this plot distinguish it from its SiO_2 counterparts shown in Figure 5-2. First, CNP is almost at $V_{BG} \sim 0$. This shows that unlike graphene device on SiO_2, graphene on BN substrate is much more homogenous and the environmental doping is minimized. Resistivity of graphene is below 50 Ω at the carrier density of $2x10^{11}cm^{-2}$ and full width at half maximum resistivity peak is extremely small (~0.5V). These observations indicate that the sample has very high charge mobility. At the low density regime, a field effect mobility of ~ 300,000 cm^2/Vs (~ 190,000 cm^2/Vs) at 5K

(300K) is extracted using $\mu = \frac{1}{e}\frac{d\sigma}{dn}$. This result is consistent with values previously reported on such systems[74], [75], [80], [120].

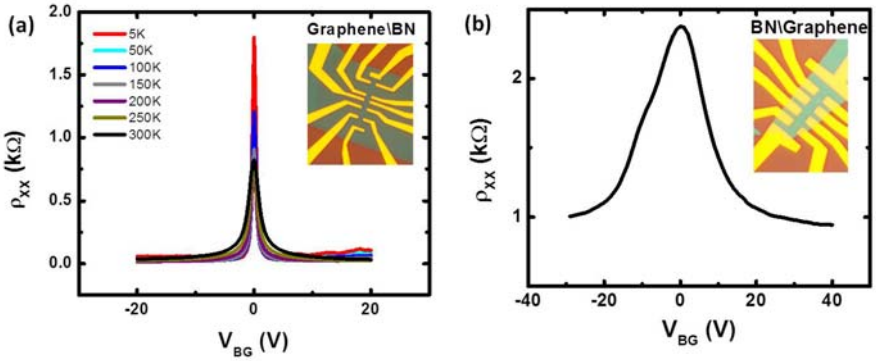

Figure 5-3. Charge transport in graphene\BN heterostructures: (a) Temperature dependent resistivity of a graphene field effect transistor on BN substrate as a function of back gate. Inset: A completed graphene Hall bar device on BN substrate. (b) Back gate voltage dependence of graphene resistivity at room temperature. Graphene device is sandwiched between SiO_2 substrate and a thin BN crystal. Inset: A completed graphene Hall bar device encapsulated with a BN crystal.

It has been demonstrated that the encapsulation of graphene between two thin BN flakes enhance the electronic quality further and allows the observation of ballistic charge transport even at room temperature[74], [75]. In order to be able to determine the effect of encapsulation on charge transport, we prepared a new device structure by transferring a thin BN on a graphene field effect transistor fabricated on SiO_2 substrate. Resistivity measurement as a function of back gate voltage in such device is shown in Figure 5-3-(b). In all measured devices, we observe an electronic mobility between 2,000 - 10,000 $cm^2/V.s$ at room temperature, similar to the graphene devices on SiO_2 substrates. This result shows that while capping BN layer may prevent the graphene device from the environmental doping[121], charge transport is still limited by the substrate induced scattering sources.

The transferring of graphene on atomically flat BN substrate creates pyramid shape bubbles at the interface of graphene and BN[85], [86]. This high density bubbles restricts the available area for the device fabrication. In this part, such bubbles are discussed. Compared to the Raman spectroscopy scan at flat graphene on BN, a shift of ~ 30cm^{-1} and ~ 60cm^{-1} is observed for G and 2D peaks respectively on bubble areas (Figure 5-4-(a)). This type of shift is associated to the presence of strain in graphene[122]. We estimate a strain of ~1.5% from the Raman analysis. In order to investigate the effect of bubbles on charge transport, graphene field effect transistor on BN substrate with locating the bubble in between voltage probes is fabricated as shown inset: Figure 5-4-(b). In all measured devices, in addition to Dirac Peak of graphene we observe a second "Dirac Peak" like feature. This extra peak might be originated from the curvature of graphene on bubble sides or the charge doping due to hydrocarbons under the bubble. While these bubbles may help realizing the strain induced pseudo magnetic field[123]–[125] in microscopic devices, it degrades the charge transport properties of graphene. For high electronic mobility samples, one has to avoid the bubbles during device fabrication.

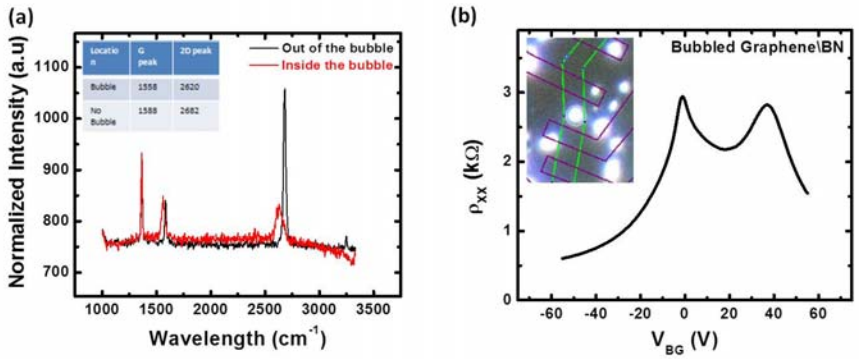

Figure 5-4. The characterization of bubble: (a) Raman spectrum of graphene on BN substrate. Red and black represents the spectrums taken at inside and outside of the bubbled graphene. (b) Resistivity measurements of graphene field effect transistor fabricated on BN substrate across a bubble as a function of back gate voltage at room temperature. Inset: Dark field image of etched

graphene (green line) before contacts are formed(purple line).The width of graphene channel is 1 μm.

Next, we measured the resistivity of graphene on a WS_2 substrate as a function of V_{BG} at RT (Figure 5-5-(a)). Graphene on a WS_2 crystal has a resistivity of only ~ 65Ωcm^{-2} at high charge carrier densities. Graphene resistivity in electron side is observed to be saturated above V_{BG} ~ 45V even though V_{BG} is continuously increased. We believe that the presence of defect vacancies in WS_2 substrate act as a sink to the electronic charges of graphene once the Fermi level aligns with these localized states. This observation is discussed in detail at Chapter 6. Hence we limit our mobility analysis to the hole doped region. Hole carrier mobilities of ~38,000 cm^2/Vs at 5x10^{11}cm^{-2} and 28,000 cm^2/Vs at 3x10^{11}cm^{-2} are calculated from the plot in Figure 5-5-(a). By using $\sigma^{-1} = \left((ne\mu) + \sigma_0\right)^{-1} + \rho_s$, a density independent mobility of 35,000 cm^2/Vs is extracted. Electronic mobility of graphene on WS_2 is four times higher than on SiO_2 substrate and this makes WS_2 an appealing substrate for graphene to reach high mobilities. Even though we consistently get high mobilities, the position of the CNP is sample dependent. For the present sample, the CNP is located at V_{BG} ~ 14V.

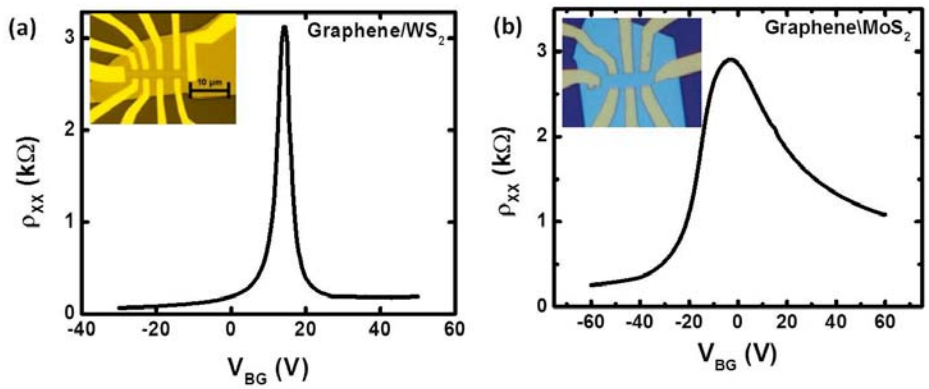

Figure 5-5. Charge transport measurement in graphene-based heterosrtuctures: (a&b) Resistivity measurements of graphene field effect transistors on WS_2 and

MoS_2 substrates as a function of back gate voltage at room temperature. Insets: Completed graphene Hall bar devices on WS_2 and MoS_2 substrate.

As a next step, we characterized a graphene FET device on a MoS_2 substrate at RT. In all measured MoS_2 devices, we observe very high asymmetry in between electron and hole conductivity (Fig.2.(b)) which is absent in graphene devices on WS2 substrate. While MoS_2 and WS_2 have comparable surface roughness as shown in section 5.2, we obtain smaller charge mobilities in graphene FET on MoS_2 substrate compared to that on WS_2 substrate. For the present device, a hole mobility of ~ 10,000 cm^2/Vs and an electron mobility of ~ 1,100 $cm^2/V.s$ are calculated away from CNP. The sheet resistance in hole conduction side is ~250 Ω which is higher than the value in BN and WS_2 based devices, but still comparable to SiO_2 substrates. A weak electron doping, possibly resulting from the impurities in MoS_2, is observed in the device.

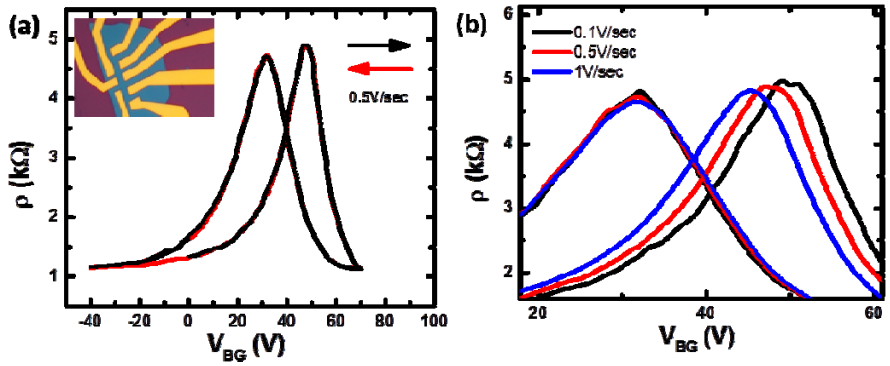

Figure 5-6. Charge transport characterization of graphene on GaSe substrate: (a) Resistivity measurement of graphene field effect transistor on GaSe substrate as a function of back gate voltage at 5K with forward and backward back gate voltage scans. (b) Resistivity of graphene on GaSe substrate as a function of back gate voltage with different back gate sweep rates.

Finally, we characterize the graphene Hall bar device on GaSe substrate. Figure 5-6-(a) shows the resistivity of graphene as a function of V_{BG} on GaSe substrate at 5 K. A field effect mobility of ~2,200 cm^2/Vs is extracted for this

sample. The CNP of graphene is observed to be highly doped (V_{BG} = 32 V). Similar low quality transport in ultra flat graphene device on mica substrate was associated to the presence of charge traps on substrate[126], [127]. We observe a huge hysteresis in graphene resistivity between forward and backward back gate voltage sweeps. Black arrow represents the forward back gate voltage sweep from -40V to 70V with a 0.5V/sec sweep rate and red arrow represents the backward back gate voltage sweep from 70V to -40V with the same sweep rate. Forward and backward sweeps completely overlap with each other as shown in Figure 5-6-(a). Resistivity of graphene device is measured with different back gate voltage sweep rates as shown in Figure 5-6-(b). While the position of CNP with forward back gate voltage scan is fixed at ~ 32V for all sweep rates, the position of CNP with backward sweeps depends on the sweep rate. For instance, hysteresis, the amount of shift in CNPs, is ~13.5V for 1V/sec, ~16V for 0.5V/sec and ~18V for 0.1V/sec. The change in the hysteresis with different sweep rates was associated to the presence of charge traps on substrate due to water[128], [129]. We attribute this hysteresis to the presence of charged traps on GaSe substrate in our system. Figure 5-7 shows the dark field images of a thin GaSe crystal just after exfoliation and with 20 seconds interval. The crystal corrodes very fast with the time. This induced contamination is most likely the cause of the observed hysteresis.

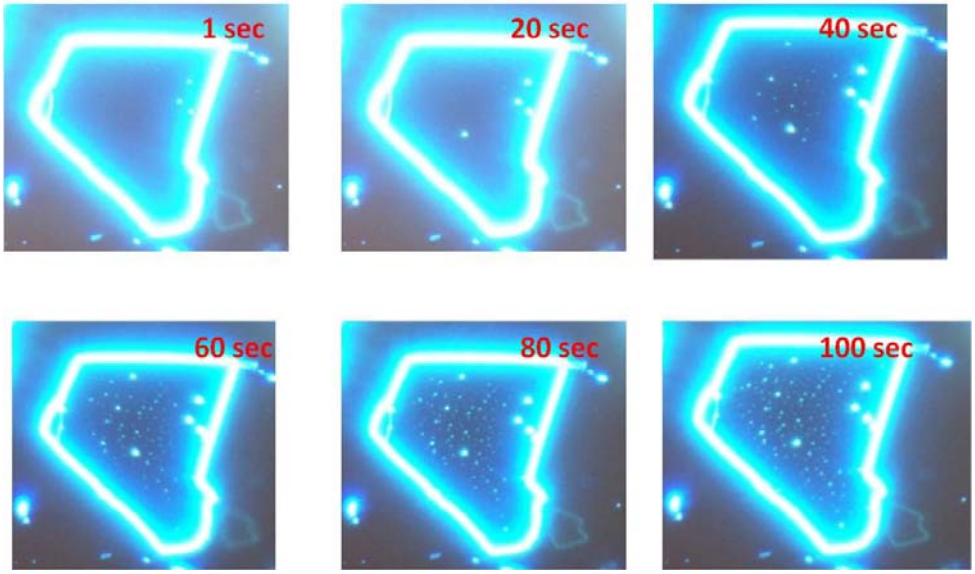

Figure 5-7. Optical image of GaSe: The dark field images of a GaSe crystal, captured just after exfoliation with 20 seconds interval. The size of flake is ~ 40 μm and thickness is ~14.5 nm.

In order to quantify the charged traps on substrate, we record the graphene resistivity while the V_{BG} is swept with forward and backward scans with different gate ranges. We observe that the hysteresis increases as back gate voltage range increases (Figure 5-8-(a)). For example the hysteresis at 50 V range is only ~ 2 V but it increases to ~37 V as the range increases to 90 V. The density of charge traps can be calculated by[129],

$$n_{tr} = \frac{C_g \Delta V}{e} \tag{5.1}$$

where ΔV is the shift of the CNP between forward and backward sweeps, C_g is the effective capacitance, ~ 718.5 e(μm)$^{-2}$V^{-1}, and e is the charge. We calculated a charge trap density of 1.45x10^{11} cm^{-2} for V_{BG}=50 V range and 2.6x10^{12} cm^{-2} for 90 V range. The observed hysteresis in our system still persists even when the sample 1- was measured at liquid helium temperatures. 2- had undergone vacuum treatment of 1.5x10^{-6} Torr for 72 hours, 3- was in situ annealed at 100

C for 6 hours under high vacuum conditions and 4- post annealed at 340 C with Ar/H_2 gaseous mixture in furnace. These observations exclude the water as a source of hysteresis. As confirmed by our dark field images (Figure 5-7) and recently discussed in a review by A. K. Geim et al[59], 2D GaSe flakes are not stable at ambient conditions and possibly creating the observed high density charged traps. The temperature dependent ρ vs V_{BG} shows that the charge trap density increases significantly from $1.15x10^{12}cm^{-2}$ to $2.6x10^{12}cm^{-2}$ as the sample temperature is increased from 5 K to 250 K under fixed V_{BG} range (70 V). Note that the position of the CNP with forward scan shifts ~10 V with increasing the temperature as shown in Figure 5-8-(b).

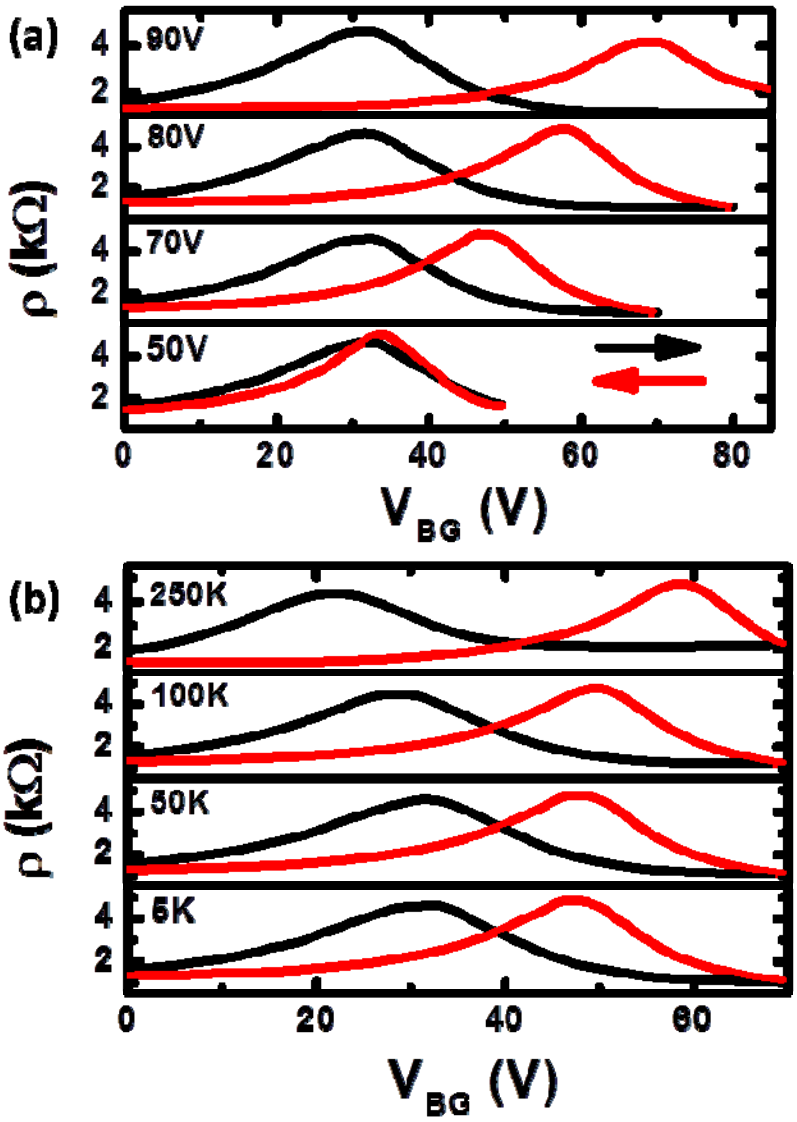

Figure 5-8. Charge transport characterization of graphene on GaSe substrate: (a) Resistivity of graphene on GaSe substrate as a function of different back gate voltage ranges at 5K. Black and red arrows represent the sweep directions from negative to positive and positive to negative. (b) Temperature dependent resistivity measurements in graphene on GaSe substrate as a function of back gate voltage.

5.4 Conclusion

In conclusion, we demonstrate that 2D crystals have flatter surfaces than conventional SiO_2 substrates. The mobility of graphene is highest in BN, followed by WS_2, MoS_2, and GaSe. Even though WS_2 has similar surface morphology with MoS_2, we observe higher mobilities in graphene devices on WS_2 than MoS_2. The observation of high density of charge traps on GaSe surface results in low mobility graphene. Last but not least important, the electronic mobility of graphene field effect transistor fabricated on bubbles have smaller charge mobilities compared to transistor fabricated on flat area. These results demonstrate that the transport properties of graphene strongly depend on the underlying substrate and address the importance of choosing appropriately the active 2D crystals for heterostructure devices.

CHAPTER 6 Spin-Orbit Proximity Effect in Graphene

The development of a spintronics device requires the manipulation of spin polarized current, ideally with electric field. While observation of exceptionally long spin relaxation lengths make graphene an intriguing material for spintronics studies, modulation of spin currents by gate field is almost impossible due to negligibly small intrinsic spin orbit coupling (SOC) of graphene. In this work, we create an artificial interface between monolayer graphene and few-layers semiconducting WS_2. We show that in such devices graphene acquires a SOC as high as 17meV, three orders of magnitude higher than its intrinsic value, without modifying any of the structural properties of the graphene. Such proximity SOC leads to the spin Hall effect even at room temperature and opens the doors for spin FETs. We show that intrinsic defects in WS_2 play an important role in this proximity effect and that graphene can act as a probe to detect defects in semiconducting surfaces.

6.1 Introduction

Graphene is a promising material for both fundamental spin based transport phenomena and low power consuming spin based device applications[27], [130]. Among the first predictions for graphene was the topological insulator with spin polarized edge states[131]. Furthermore, room temperature (RT) ballistic charge transport[74], [75] and gate-tunability[22] make graphene an ideal material for realizing Datta-Das type spin field effect transistors (FETs)[132]. However, graphene's extremely weak intrinsic spin-orbit coupling (SOC)[23], [133] makes the experimental observation of these phenomena very challenging. Previous studies have shown that the weak hydrogenation of graphene can significantly enhance the SOC[50], [105]. However, chemical functionalization introduces disorder and severely limits charge mobility and

hence, the spin relaxation length[50], [134]. Equally important, the hybridization between hydrogen and carbon induces a Rashba type SOC by introducing sp_3 defects thereby breaking the inversion symmetry of the lattice[135]. The decoration of the graphene surface with heavy metal adatoms such as gold (Au), indium (In) or thallium (Tl) has also been proposed to increase the spin orbit coupling[136], [137]. However, also this approach introduces disorder and hence, equally limits both charge and spin transport properties[138].

These challenges have recently brought to light other 2D crystals such as transition metal dichalcogenides (TMDC). TMDCs have band gaps in a technologically attractive energy range (~1-2 eV) and orders of magnitude higher SOC than graphene[139]. This, combined with spin split bands makes them an almost ideal material for spintronics. However, the presence of unavoidable defects in TMDCs typically limits their electron mobilities to $\mu \sim 100\ cm^2/V.s$[69]. Hence, we expect a spin relaxation length even lower than in weakly hydrogenated graphene. This limits the prospects of practical spin devices based on TMDCs. In this chapter, we show that by utilizing the proximity effect between graphene and TMDCs one can keep the extraordinary high mobilities of crystalline graphene and at the same time enhance its SOC to allow electric field controllable spin currents at room temperature.

6.2 Characterization of WS_2 crystal

6.2.1 Growth and XPS of WS_2 crystal

Bulk crystals of 2H-WS_2 were grown by the chemical vapor transport (CVT) method using iodine as the transport agent. As-received WS_2 powder (Alfa Aesar, 99.9 purity %) was sealed in an ampoule of fused quartz. The ampoule was kept in a temperature gradient from 875 to 935 C in a dual zone furnace for 1 week. WS_2 crystals grew on the cold end of the ampoule.

X-ray photoelectron spectroscopy (XPS) measurements were performed by using non monochromatic Mg *Ka* radiation (1253.6eV). Figure 6-1-(a) shows the survey scan of a WS_2 crystal. Along with W and S core levels, O_{1s} and C_{1s} peaks are also observed. Next, we focus on the XPS spectra of W_{4f} and S_{2p} core levels (Figure 6-1-(b)). The W_{4f} core level peak could be fitted to two sets of doublets corresponding to W (+6) and W (4+) oxidation states. The presence of W (+6) oxidation states indicates that tungsten disulphide has undergone oxidation. The observed peak position for $W_{4f7/2}$ for the +6 and +4 oxidations states matches with those reported in the literature[140]. The S_{2p} peak could be fitted to only one set of doublet corresponding to S-W bonding.

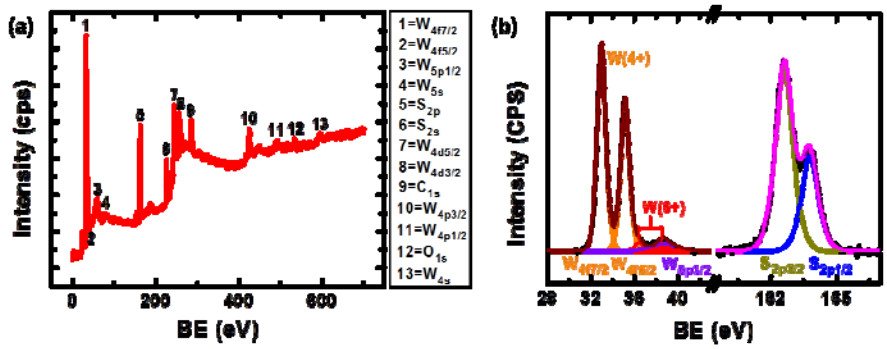

Figure 6-1. XPS of WS_2 crystal: (a) XPS survey scan of WS2 crystal acquired with Mg Ka line. (b) High resolution XPS of W_{4f} and S_{2p} core levels.

The stoichiometry of WS_2 crystal was obtained by using:

$$\frac{[W]}{S} = \frac{\sigma_{S2p}(h\nu)}{\sigma_{W4f}(h\nu)} x \frac{\lambda_{S2p}}{\lambda_{W4f}} x \frac{I_{W4f}}{I_{S2p}} \tag{6.1}$$

where $\sigma_{S2p}(h\nu)$ and $\sigma_{W4f}(h\nu)$ are photo-ionization cross sections of the 2p and 4f core level of sulphur and tungsten, respectively. The values of $\sigma_{S2p}(h\nu)$ and $\sigma_{W4f}(h\nu)$ were estimated to be 0.045 and 0.18 Mb, respectively, from reference[141]. I_{S2p} and I_{W4f} are the intensities of the photoelectron peaks of the

S_{2p} and $W4_f$ levels, respectively, which were obtained from Figure 6-1-(b). λ_{S2p} and λ_{W4f} are inelastic mean free paths (IMFP) of the photoelectrons with kinetic energies that correspond to the S and W core levels, respectively. The values of λ_{S2p} and λ_{W4f} were estimated to be 1.29 nm and 1.36 nm respectively using the Seah and Dench method[142]. With these values the [W]/[S] ratio was estimated to be 0.57. This means that sulphur vacancies are present in the WS_2 crystal.

6.2.2 AFM and Raman characterization

First WS_2 flakes are prepared on SiO_2 substrates with mechanically exfoliation technique and then annealed in a gaseous mixture of Ar / H_2 (9/1) at 350 C for 3 hours to ensure the surface is free of residues. Figure6-2-(a) shows the typical optical and AFM images of few layers WS_2 with 12 nm thickness after the annealing process. The thickness of WS_2 substrates used in this study varied from 5 nm to 15 nm. The surface topography shows that the surface roughness in WS_2 is comparable to that of BN[80].

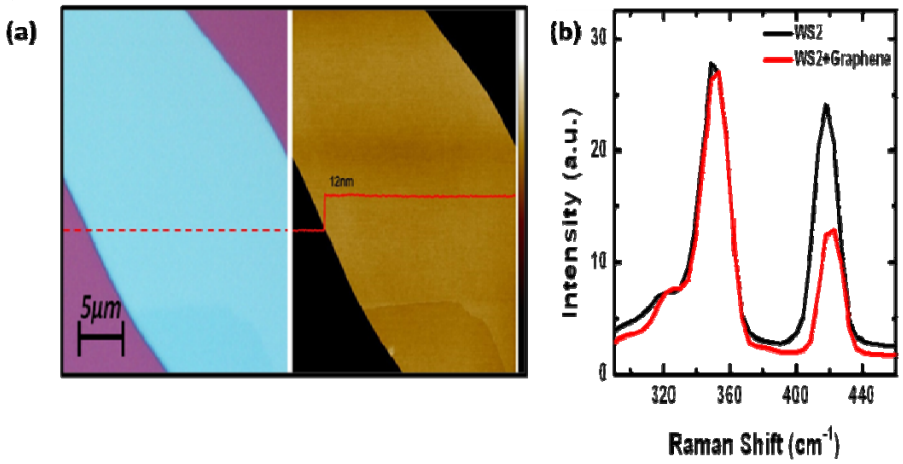

Figure 6-2. AFM and Raman characterization of WS2 crytsal: (a) Optical and AFM images of a representative WS_2 flake. Color scale of the AFM image represents 0-20 nm.(b) Raman spectrum of few layers WS_2 with and without graphene.

Figure 6-2-(b) shows the typical Raman spectra of few layers WS_2 before and after graphene transfer. An excitation wavelength of 532 nm is used. The Raman spectrum is dominated by two peaks at 351 cm^{-1} and 418 cm^{-1} similar to those reported in reference[143]. The peak at 351 cm^{-1} is the overlapping of a first-order mode (E^1_{2g} (Γ)) and second order mode that is activated by disorder (2LA (M)). The peak at 418 cm^{-1} is due to another first order mode at the Brilliouin zone, A_{1g} (Γ). Unlike the peak at 351 cm^{-1}, the intensity of the peak at 418 cm^{-1} is reduced slightly after the graphene transfer. The laser power in this measurement is kept below 0.2mW to avoid any damage to the flakes.

6.3 Charge transport in graphene-WS_2 heterostructures

We followed the recipe shown in chapter 3 to fabricate the graphene/WS_2 heterostructure devices. Standard dry transfer method is implemented to transfer single layer graphene (SLG) onto atomically flat few layers of WS_2[74]. Typical channel lengths and widths in our Hall bar devices are l = 3μm and w = 1μm respectively. A pair of electrodes is also created directly on WS_2. An optical image of a typical final device is shown in Figure 6-3-(b). Experiments were carried out in two different measurement configurations. In the conventional local four terminal measurement configuration (Hall bar), current I_{16} flows between contact 1 and contact 6 and a local voltage drop is measured between contact 2 and contact 4. In the non-local measurement configuration (H bar), the current I_{23} flows between the pair of contact 2 and contact 3 and a non-local voltage V_{45} is recorded across the neighboring pair of contact 4 and contact 5 (Figure 6-3-(c)). All measurements were performed with standard ac lock-in technique at low frequencies in vacuum as a function of magnetic (B), back gate voltage (V_{BG}) at both room temperature (RT) and liquid Helium temperatures. In total, we have characterized 10 Graphene/WS_2 devices. Here I discuss mainly 2 representative devices and unless otherwise stated, the results shown are from device B.

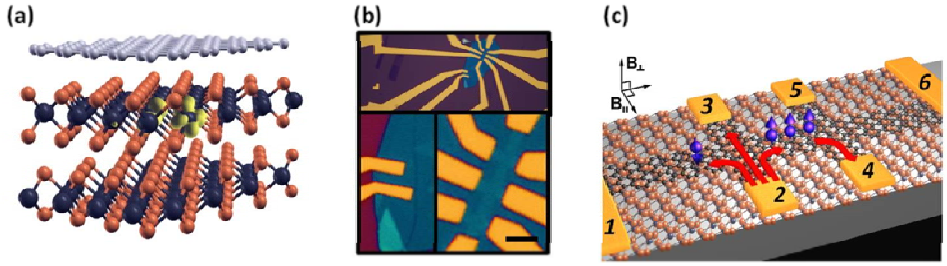

Figure 6-3. Device fabrication and systematics of graphene/WS_2 heterostructures: (a) Schematics representation of a multilayer WS_2/Graphene heterostructure device. The highest unoccupied state of the sulphur vacancy is depicted in yellow, highlighting on the W atoms closest to the vacancy. W, S and C atoms are represented by dark gray, orange and light gray spheres, respectively. (b) Optical micrograph of a completed device with multiple Hall bar junctions on G/ WS_2 heterostructure and a two terminal device on WS_2. The scale bar is 2μm. (c) Schematics for the local and non-local measurement configurations.

Figure 6-4-(a) shows the conductivity of graphene on WS_2 substrate as a function of V_{BG} at 1.5K. Several features immediately distinguish the transport of this device from those on SiO_2[22]. While conductivity is remarkably linear in V_{BG} on hole side, sample exhibits a V_{BG} independent conductivity above a threshold back gate voltage, V_{TH} ~18V on electron side. A similar behavior has been observed in all graphene on WS_2 devices and is absent e.g. in graphene on BN devices. The sample shows a narrow resistivity peak, a signature of high charge mobility. A field effect mobility of ~ 18,000 cm^2/V.s at low densities is extracted using $\mu = {}^{d\sigma}/_{dne}$. Our devices reach electronic mobilities as high as 50.000 cm^2/ Vs, comparable to what has been reported on BN substrates[80], [120]. These results demonstrate that atomically flat 2-D TMDCs are promising substrates for graphene to achieve high mobilities. Next, we discuss perpendicular magnetic field ($B_\perp$) dependent measurements as shown in Figure 6-4-(b&c). From Hall effect measurements at low fields, we see that the origin of the conductance saturation on the electron side is due to the saturation of the

charge density at ~ $7x10^{11}$ cm^{-2} (Inset-Figure 6-4-(c)). In high $B_\perp$ fields, this surprising result even alters the well known Landau level (LL) fan diagram of graphene. This is clearly seen in the fan diagram where the longitudinal resistance, R_{XX}, is recorded on a color plot as a function of both V_{BG} and the perpendicularly applied $B_\perp$ (Figure 6-4-(b)). For example, at $B_\perp$ =4.5T, R_{XX} vs V_{BG} shows the regular integer quantum hall effect on the hole side with filling factor ν=2, 6, 10, 14, 18, 22. However, on the electron side only the quantization for the first two LLs is observed. Since the LLs in graphene are not equally spaced in energy, it is possible to lock the graphene resistance even at the first LL for | $B_\perp$| > 10T (Figure (6-4-(c)), making such graphene/WS_2 heterostructure potentially a suitable device for quantum resistance metrology[54]. The observed phenomenon allows for sustaining a nondissipative current over a large back gate range, resulting in an unusual robust quantization of the resistance.

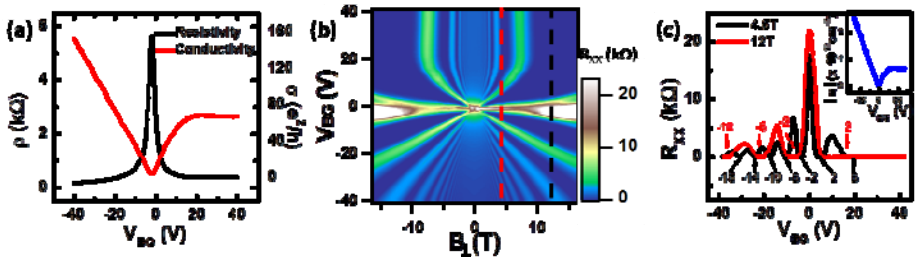

Figure 6-4. Electronic transport measurement in graphene on WS_2 substrate: (a) Local resistivity (black lines) and conductivity (red line) measurement as a function of back gate voltage at 1.5 K. (b) Landau fan diagram of longitudinal resistance as a function of magnetic field and back gate voltage. (c) Corresponding plots of longitudinal resistance as a function of back gate voltage at constant magnetic fields. (Black and red lines represent 4.5 T and 12 T respectively.) Inset: Carrier concentration as a function of applied back gate voltage.

In order to rule out any shunting of this current through WS_2, we performed two terminal resistance measurement directly across WS_2, without graphene (Figure 6-3-(b)). WS_2 showed an insulating response under a bias voltage of 0.1V with a gate sweep from 40V to -40V (Figure 6-5-(a)). In fact, we expect a sudden drop of graphene resistance if Fermi level would reach the conduction band of WS_2. Demonstration of such an insulating response makes 2-D TMDCs a promising substrate for general graphene studies which require high mobilities. Finally, we prepared a graphene field effect transistor on WS_2 substrate and the sample is coated with PVDF dielectric to apply an electric field with a top gate contact. Figure 6-5-(b) shows the conductivity of graphene in such device. Saturation in conductivity is observed and associated to the proximity effect of WS2 onto graphene.

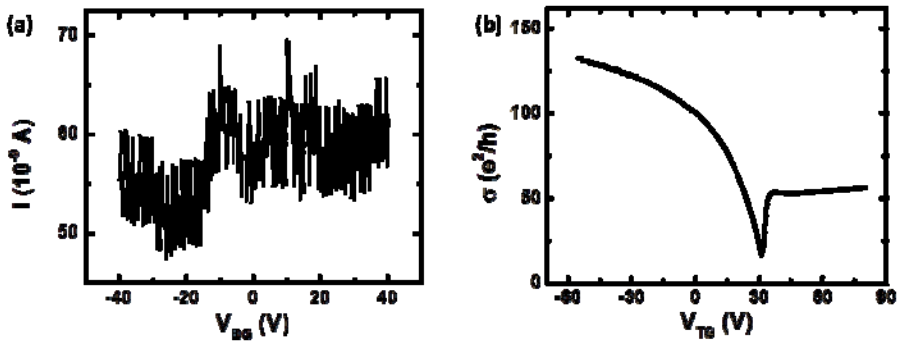

Figure 6-5. (a) Two terminal resistance measurement in few layers of WS2 flake at 1.5K. (b) Conductivity measurement of graphene on WS_2 substrate as a function of top gate voltage through a PVDF top dielectric.

Finally, we check the physical characteristics of charge carriers in graphene. The resistivity of graphene is characterized as a function of $B_\perp$ and V_{BG} at fixed temperatures. The measurements are repeated for temperatures from 1.5K to 90K with a 15K step. Figure 6-6-(a&b) shows such Landau fan diagrams of the longitudinal resistance at 15K and 30K. The amplitude of SdH oscillations is extracted from these color plots at fixed V_{BG} ranges with a step of ΔV=10. Figure 6-6-(c)shows such plot at V_{BG} = -20V. The amplitude of SdH

oscillations can be described by the following expression to extract effective mass of charge carriers:

$$T/\sinh(4\pi^3 T m_*/heB) \tag{6.2}$$

where T is the temperature, m_* is the effective mass and h is the Planck constant[144]. The gate dependence of m_* and carrier concentration is shown in Figure 6-6-(d). While m_* increases slightly in V_{BG} on the hole side, similar to the previous report[145], it saturates above a threshold voltage on electron side.

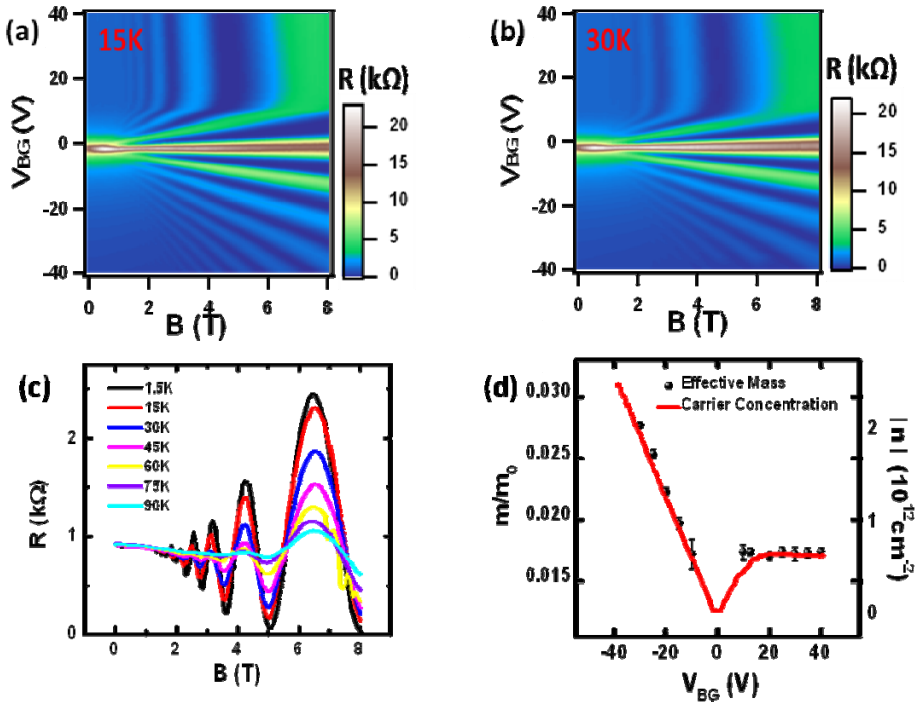

Figure 6-6. Electronic transport measurement in graphene on WS_2 substrate: (a&b) Landau fan plots of longitudinal resistance at 15K and 30K, (c) Amplitude of SdH oscillation as a function magnetic field at different temperature values. (d) Calculated effective mass and carrier concentration as a function of back gate voltage.

6.4 Spin Hall effect in graphene-WS2 heterostructure

We now turn our attention to non-local transport measurements. This measurement technique is a powerful tool to detect spin dependent transport phenomena that otherwise escape notice. Recently, this configuration has been for example used to detect Zeeman interaction induced spin currents in graphene in the presence of an externally applied perpendicular magnetic field[146], [147]. Balakrishnan *et al*, also implemented this geometry to demonstrate an enhancement of SOC in hydrogenated graphene by measuring spin precession in an in-plane magnetic field[50]. We first discuss the RT non-local measurement of a graphene on SiO_2 device of comparable mobility ($\mu \approx$ 13.000 cm^2/V.s) (Figure 6-7-(a)). For such devices the non-local resistance is symmetric around the Dirac peak and its magnitude over the entire back gate bias range can be fully accounted for by an Ohmic leakage contribution[49], $\sim \rho e^{-\pi L/w}$ (dashed dotted fit to the data). In contrast, graphene on WS_2 substrates (Devices B and C, Figure 6-7-(b&c)) shows a non-local signal which cannot be accounted for by an Ohmic contribution neither quantitatively nor qualitatively. First, the magnitude of the observed non-local signal is almost an order of magnitude larger than in graphene on SiO_2 samples. More importantly, we observe a strong electron-hole asymmetry in non-local resistance, which is completely absent in both graphene on SiO_2 and even in graphene on BN substrates (not shown). For instance, device B and device C have a non-local signal difference ΔR between the hole side and electron side of $\Delta R \sim 8\Omega$ and $\Delta R \sim 20\Omega$, respectively. We find that there is a sample to sample variation of the non-local signal due to the variation in amount of the disorder in each sample, however the electron-hole asymmetry in the non-local signal is observed in all our graphene-WS_2 devices. As shown in Figure 6-8-(a&b), we observe a significantly reduced background signal in the samples had been annealed longer. Black line represents the Ohmic contribution. For $V<V_{TH}$ the non-local signal is fully accounted for by the later. However, for $V> V_{TH}$ we see

a strong enhancement of the non-local signal. This asymmetry rules out both local heating effects and Ohmic contributions and shows that for $V>V_{TH}$ can only be due proximity induced SOC enhancement. The observed fluctuation in the non-local signal near the Dirac Point is attributed to the presence of charge puddles. Equally important, the onset of the asymmetry coincides with V_{TH} at which the local conductivity saturates. Note that even there is a background signal, asymmetry does rule out thermal effects as discussed in Reference [146] as the dominant effect.

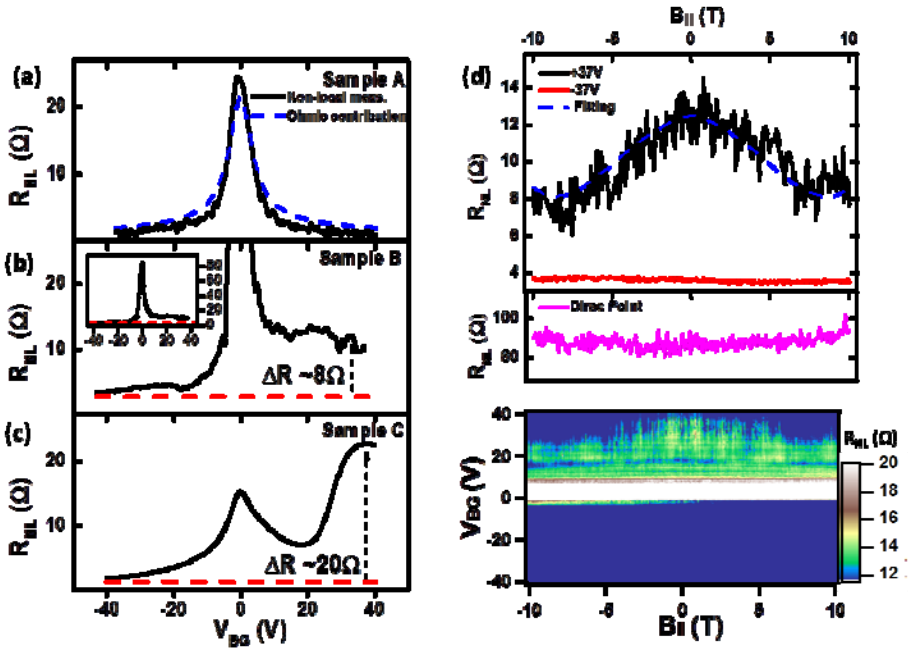

Figure 6-7. Spin transport measurement in graphene on WS_2 substrate: (a) Nonlocal resistance measurement as a function of back gate voltage at RT in a reference graphene/SiO_2 device, Sample A, (red line) with its calculated Ohmic contribution (black line). (b-c) Nonlocal measurement for Sample B and Sample C at 1.5K and RT respectively. (d) Fan diagram of nonlocal resistance as a function of in-plane magnetic field and back gate voltage. Color scale bar is adjusted to show between 12-20 Ω for clarification. Corresponding plots of non-local resistance as a function of in plane magnetic field at constant back

gate voltages.(Black, pink and red lines represent the back gate voltages of 37 V , 2V (D.P.) and 37 V respectively.)

To determine the origin of the non-local signal, we applied a magnetic field $B_{||}$ in the plane of the device parallel to the current flow direction. Such Hanle spin precession measurements for device B as a function of V_{BG} are summarized in Figure-6-7-(d). Also here we see a clear electron-hole asymmetry. The critical gate voltage at which the field dependence of the non-local signal changes dramatically coincides again with V_{TH} at which the conductance saturation is observed. For all $V_{BG} < V_{TH}$, the non-local signal is magnetic field independent. Two representative R_{NL} vs $B_{||}$ traces at $V_{BG} = -37$ V and $V_{BG} = 2$ V (DP) are shown in Figure-6-7-(d). On the other hand For all $V_{BG} > V_{TH}$, the nonlocal signal shows a maximum at zero magnetic field and decreases with increasing $|B_{||}|$ with the onset of an oscillatory behavior clearly visible for $|B_{||}| > 8$ T. Remarkably, the maximum observed change of the non-local signal $\Delta R = 8\Omega$ as a function of field is comparable to the difference observed in the non-local signal ΔR as a function of V_{BG} (Figure-6-7-(b)). It is important to note that in this measurement configuration only a spin current can give rise to a magnetic field dependent signal[18]. Thus, the observation of oscillatory magnetic field dependent signal directly proves the spin origin of the non-local signal. In samples with higher mobilities, we even observe a full oscillation cycle as shown in Figure 6-8- (c). We are now ready to extract the spin transport parameters of our devices. For this we fit the field dependence of the nonlocal signal using the following equation[49]:

$$R_{NL} = \frac{1}{2}\gamma^2 \rho w Re\left[\left(\sqrt{1 + iw_B\tau_s}/\lambda_s e^{-\left(\sqrt{1+iw_B\tau_s}/\lambda_s\right)|L|}\right)\right] \tag{6.3}$$

where γ is the spin Hall coefficient, w the width of the channel, ρ is the resistivity of the channel, ω_B is the Larmor frequency, τ_s is the spin relaxation

time, and λ_s is the spin relaxation length. We obtain λ_s = 2 μm, τ_s of 5 ps. The strongly reduced τ_s when compared with τ_s of even hydrogenated spin valves[134] (~ 0.7ns) is direct consequence of the colossal enhancement of SOC.

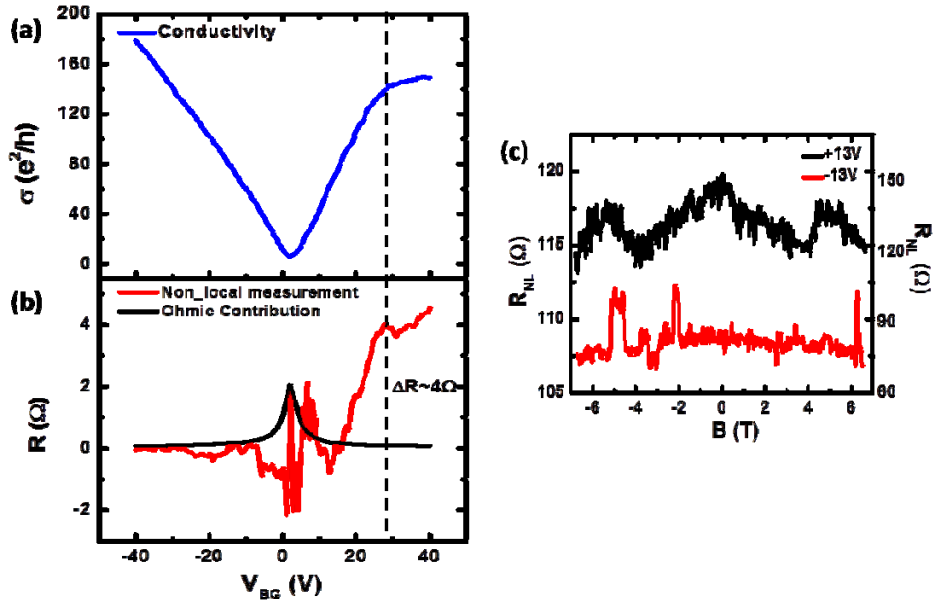

Figure 6-8. Spin transport measurement in graphene on WS_2 substrate: (a,b) Local conductivity and non-local resistance measurement of graphene on WS_2 substrate. Black curve in (b) represents the Ohmic contribution to the non-local signal. The threshold voltage for this sample is at 29V. c - Non-local signal as a function of in plane magnetic field at back gate voltages of 13V -13V. The threshold voltage for this sample is at 10V (not shown).

Next, we calculate the proximity SOC strength Δ_{SO}. Since the dominant dephasing mechanism in SLG is Elliott-Yafet type[27], [45] we have $\Delta_{SO} = \varepsilon_F\sqrt{(\tau_P/\tau_S)}$ where ε_F is the Fermi energy and τ_P is the momentum relaxation time, $\tau_P = h\sigma/2e^2v_F\sqrt{(\pi n)}$. Thus, we obtain a proximity SOC of 17.6 meV which is even higher than that achieved by hydrogenating graphene[50]. With

this, we identify the SHE and inverse SHE as the origin of the observed non-local signal. The latter is only possible because of the three order of magnitude enhancement of the intrinsic SOC graphene when in proximity with WS_2.

We also utilize dc technique to perform the non-local transport measurements. Before starting this measurement, the sample is characterized first with ac technique. As shown in Figure 6-9- (a), the sample shows the saturation of conductivity above threshold voltage (V_{TH} ~20V) at electron side. A field effect mobility of ~50,000 $cm^2/V.s$ is extracted near the Dirac point. From the non-local measurements, we observe a non-local signal once $V_{BG} > V_{TH}$ (Figure 6-9-(b)). While the background signal at Dirac point is reduced compared to the previously shown samples, the signal is higher than the estimated Ohmic contribution. As shown in Figure 6-9- (c), the spin precession effect near Dirac point is missing that's why the signal at Dirac point can not be associated to spin dependent signal. An oscillating signal with applied in-plane magnetic field is only observed at $V_{BG} > V_{TH}$ where we observe the non-local signal from gate dependent measurements as well. This confirms that the origin of signal is spin transport at $V_{BG} > V_{TH}$.

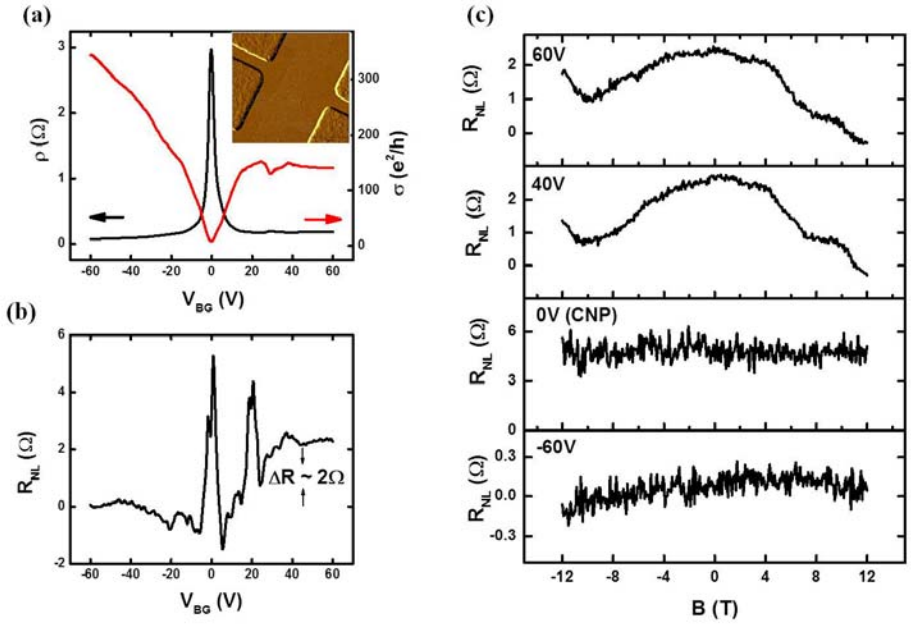

Figure 6-9. (a) Resistivity and conductivity of graphene as a function of V_{BG} at 2K. Inset shows the AMF picture of graphene channel on WS_2 substrate. (b) Non-local resistance as a function of V_{BG}. (c) Non-local resistance as a function of in-plane applied magnetic field at V_{BG} = 60V, 40V, CNP and -60V.

Next, we utilize dc technique to perform the non-local transport measurements in the sample shown in Figure 6-9. Dc response of the non-local voltage above V_{TH} (V_{BG} = 60V) is shown in Figure 6-10- (a). The linear dependence of measured voltage with applied current bias (both current polarities) excludes the Joule heating as the source of signal. The V-I is also linear under externally applied in-plane magnetic fields (Inset Figure 6-10- (a)). Signal decreases as the magnetic field increases and this is consistent with Figure 6-9- (c). Finally, we show the spin precession results detected by a fixed current bias of 1.5 μA (Figure 6-10- (b)). We observe the change in non-local signal as in-plane magnetic field is scanned. The magnitude and behavior of signal is similar to ac measurements shown in Figure 6-9- (c) and previous meausurements. These results exclude Joule heating as the source of signal.

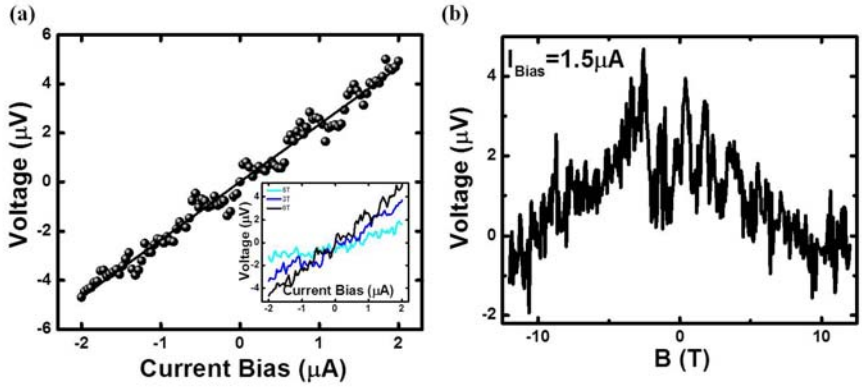

Figure 6-10. (a) Current bias dependence of non-local signal. Inset shows the current bias and magnetic field dependence of non-local signal. (b) Spin precession measurement with a fixed current bias at 1.5 μA.

While the overall behavior of the non-local resistance as a function of V_{BG} is similar in all characterized samples, we see sample-to-sample variation in the amplitude of non-local signal especially near Dirac peak. A detailed summary of measured samples is shown in Figure 6-11. While sample #3 and #5 have signals at Dirac point comparable to the estimated Ohmic contribution, we observe a non-local resistance near Dirac peak which is higher than the estimated Ohmic contribution in most of the measured devices. The absence of spin precession signal near Dirac point suggests that the signal near Dirac peak is artifact. There is no correlation between the signal at Dirac peak and mobility. Further studies are required to explain the origin of signal near Dirac point. However, as discussed previously, the spin contribution to R_{NL} can be easily estimated in our devices, since the observed proximity effect exhibits a strong electron hole asymmetry. For $V_{BG} > V_{TH}$ we again see a strong enhancement of the non-local signal.

Sample	Mobility ($cm^2/V.s$)	Calculated Ohmic Contribution at DP (Ω)	Non-local signal at DP (Ω)	Spin signal (△ R) (Ω)
#1	49,500	0.72	5.25	2
#2	43,500	1.02	4	0.7
#3	35,000	1.05	1.1	0.25
#4	24,750	1.41	86	8
#5	22,140	1.96	2	4
#6	21,000	0.5	5.6	7
#7	18,000	1.21	15.2	20
#8	15,000	0.8	2	4
#9 (Not annealed)	12,000	0.97	6.4	1.5

Figure 6-11. The summary of measured samples. While the spin signal presents in all samples, the non-local signal at Dirac point has sample to sample variation.

The presence of weak localization (weak anti-localization) can be experimentally realized with a positive (negative) magneto conductance at low magnetic field range[55]. Graphene has been shown to have weak localization behavior[148]. The demonstration of weak anti-localization in semiconductors with high SOC materials makes these measurements ideal tool to determine the strength of SOC in materials[57]. We have performed magneto transport measurements in graphene FET on WS_2 substrate at 50mK temperature. As shown in Figure 6-9, we observe weak localization at Vbg<Vth. Once back gate voltage exceeds the V_{TH}, we observe weak anti-localization behavior. This is signature of an enhancement of SOC at Vbg>Vth, consistent with our spin precession measurements.

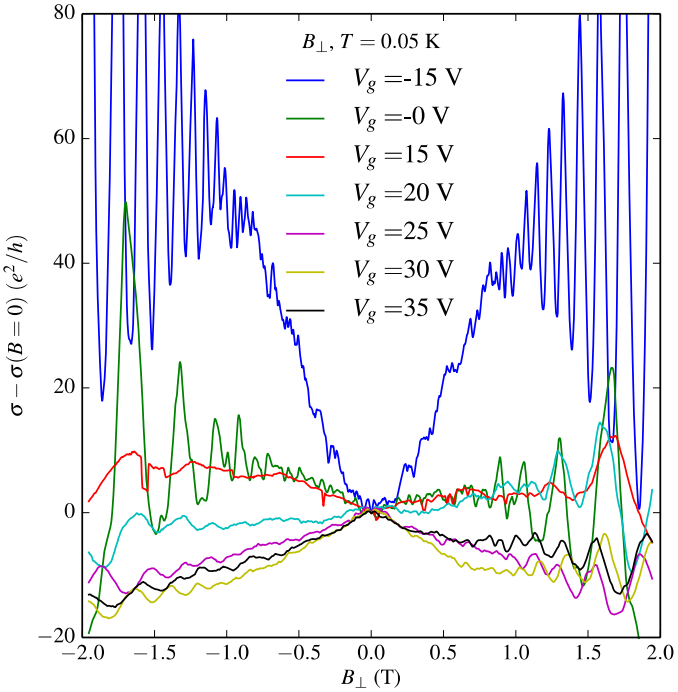

Figure 6-12. Quantum interference effect in graphene on WS_2 substrate: Normalized conductivity of graphene under perpendicularly applied magnetic field at 50mK at different back gate voltages.

Finally, we discuss the origin of the proximity effect in more detail. Recently single sulphur vacancies have been observed in MoS_2 flakes by using an atomic resolution direct imaging technique[149]. Similar structural defects are also expected for WS_2 crystals. As discussed in section 6.2, the analysis of XPS spectra of W_{4f} and S_{2p} show that the stoichiometry of crystal [W/S] is 0.57. This result shows that there are localized states in the gap of WS_2, originating from sulphur vacancies. As a next step, we performed ab initio fully relativistic density functional theory (DFT) calculations to discuss the relevance of these states on the observed phenomena[150]. Our calculations for the band structure of the graphene/WS2 interface show that the Dirac point of graphene is within the WS_2 band gap (Figure 6-10). The band structure of the interface is nearly a superposition of the band structures of the two moieties. The lowest conduction

band of WS_2 is practically unchanged by the presence of graphene, and its position relative to the Fermi level differ less than 0.1eV from those obtained by the alignment of the vacuum level for the two independent systems. Note that the proximity of WS_2 without vacancies does not induce any significant SOC. A sulphur vacancy (V_S) on the other hand introduces a double unoccupied state in the top half of the band gap of bulk WS_2 (Figure 6-10), as close as ~ 0.1eV to the Fermi level of graphene. In fact, using $\varepsilon_f = \hbar v_f \sqrt{\pi n}$ where v_f is the Fermi velocity (0.9×10^6 m /s) and n is the carrier concentration (7×10^{11} cm^{-2}) at V_{TH} we obtain $\varepsilon_f \sim$ 0.09 eV at V_{TH} in good agreement with our theoretical estimate. The mid gap states originate on the vacancy dangling bonds and are localized on W. They have an unusually large spin splitting of about ΔE_{SO} ~ 0.2eV to which we assign the origin of the proximity SOC observed. The graphene electrons move from graphene to the vacancy states in WS_2 by quantum tunneling. This tunneling relies on the proximity of the wavefunction of the vacancy states to the graphene, which is characterized by hybridization energy V_H. From second order perturbation theory ($\Delta E_{SO} \approx {V_H}^2/\Delta_{SO}$), the hybridization energy is estimated to be 0.059 eV.

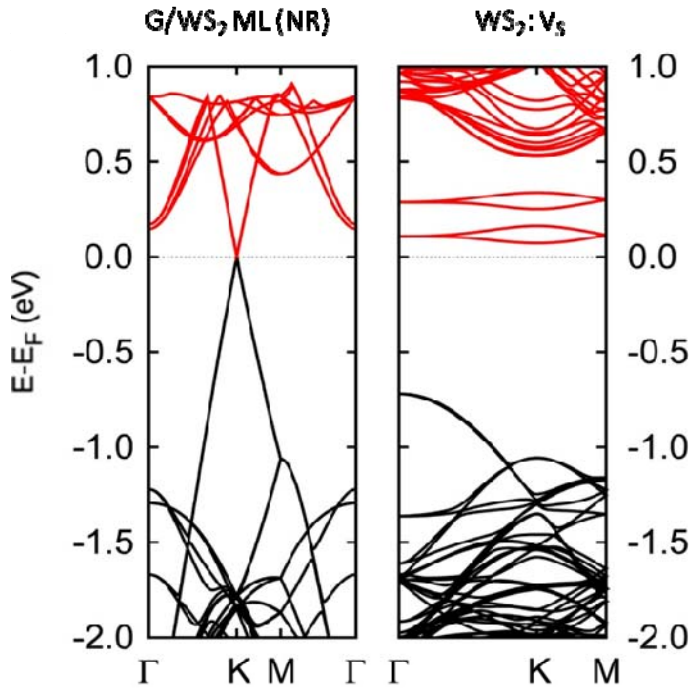

Figure 6-13. Bandstructures for the interface between graphene and monolayer WS_2 and sulphur vacancy in bulk WS_2. In the latter, a rigid shift of 0.2 eV has been applied to the unoccupied states to correct the bandgap to the experimental value.

While the XPS measurements shown performed on the crystal just after the growth, the annealing process in forming gas during the device fabrication might also have significant effect on the creation of vacancies in substrate. In order to exclude the annealing process as the source of vacancies, we repeated the experiment in non-annealed samples.

We fabricated a new sample without involving any annealing step. Figure 6-14-(a) shows the optical and AFM images of the sample after graphene is transferred onto WS_2 substrate. Heterostructure has high density bubbles at the interface and they can't be removed since the annealing step is skipped. Figure Figure 6-14-(b) shows the resistivity and conductivity of graphene as a function of V_{BG}. A mobility of ~ 5,000 (12,000) $cm^2/V.s$ is extracted at high (low) charge carrier concentrations. The mobility is limited due to presence of

bubbles at the interface, as well as polymer residues on graphene. The saturation of conductivity above threshold voltage (V_{TH}) is also observed in this non-annealed sample. Similar to the annealed sample shown previously, the saturation of conductivity above V_{TH} still exists even externally magnetic field is applied (Figure 6-14-(c)). A finite non-local signal is also observed in this non-annealed sample (Figure 6-14-(d)).These results prove that sulphur vacancies form during the growth process and they are unavoidable.

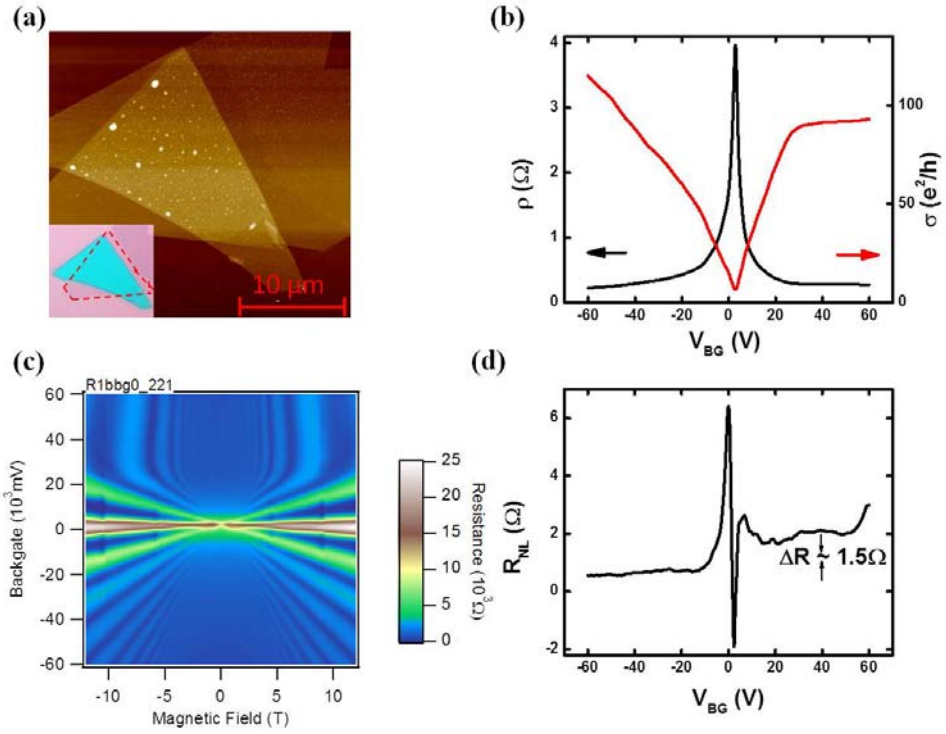

Figure 6-14. (a) Optical and AFM images of a transferred graphene on WS_2 substrate. Red dashed lines represent the border of graphene flake for better clarify. (b) Resistivity and conductivity of graphene as a function of back gate voltage at 2K. (c) Landau fan plot of longitudinal resistance as a function of back gate voltage and magnetic field. (d) Non-local spin signal measurement in non-annealed sample.

6.5 Conclusion

In conclusion, we have demonstrated that graphene is very sensitive to the defects in the underlying WS_2 substrate. These structural defects enhance the weak SOC of graphene while preserving the extraordinary electronic properties. Since all TMDCs have similar structures and properties, this proximity effect is expected to be present in a wide range of different crystals. Our results open a new avenue for the realization of many exotic phenomena such as the quantum SHE.

CHAPTER 7 Summary and Future Work

Having very small spin orbit coupling and negligible hyperfine interaction makes the graphene an interesting material for spintronics studies[23]. The observation of room temperature micron-size spin relaxation lengths in exfoliated graphene based spin valve devices with a unique gate tunability property got the attention of spintronics community[37], [92]. The correlation between the charge and spin transport properties of single layer graphene points that Elliott-Yafet type spin scattering mechanism is dominant in single layer graphene[27], [45]. Surprisingly, the experiments we performed on exfoliated bilayer graphene shows an inverse scaling between momentum relaxation time and spin relaxation time. Such behavior is the signature of the dominant D'yakonov-Perel type spin scattering mechanism[27], [46], [47]. While these observations are critical for understanding the spin transport in graphene and helps creating the new strategies to enhance the spin transport properties of graphene, exfoliated graphene has scalability problem for its integration into real applications[58]. Towards this, we prepared CVD graphene based spin valve devices to study the spin transport properties of artificially grown large size graphene. After transferring of CVD graphene onto Si/SiO2 wafer, electron beam lithography technique is used for patterning of the contacts. MgO tunnel barriers for combating the conductivity mismatch problem and Co ferromagnetic contacts for spin generation are deposited with electron beam evaporation technique. While CVD graphene has structural difference compared to exfoliated graphene such as high density of ripples[28], wrinkles, transfer residues, grain boundaries[43], [58] etc, we observe very clear spin signal in CVD single and bi-layer graphene based spin valve devices[27]. The spin scattering mechanisms in CVD grown single and bi-layer graphene are the same with their exfoliated counterparts. The observation of long spin relaxation lengths in CVD graphene makes the integration of graphene into spintronics application possible.

The effective spin injection into graphene and the understanding of the striking difference between theoretically predicted and experimentally observed spin relaxation length values are yet waiting to be solved. The initial spin transport devices utilized the Al_2O_3 tunnel barriers to inject spin current into graphene[37]. The spin injection efficiency was limited to ~ 10% in these devices. In this thesis, we replaced the amorphous Al_2O_3 barrier with ultra flat MgO barrier. Similar to Al_2O_3 tunnel barrier devices, spin injection into graphene suffer from the presence of pinholes in MgO barrier. While Kawakami group showed that the addition of a TiO_2 buffer layer allows continues, flat MgO growth[106] (spin injection up to ~31% was shown), it is still challenging to have pin-hole free, reproducible high quality tunnel barrier. It is important to create high quality spin interface for efficient spin injection to graphene with least amount of spin dependent scattering at the ferromagnetic material and graphene interface.

The identification of Elliott-Yafet type spin scattering mechanism in single layer graphene suggests that an enhancement in the electronic quality of graphene will enhance the spin transport properties of graphene[27], [30], [45]. Towards this, van Wees group performed the spin transport experiments in suspended graphene device[151]. While the electronic quality is enhanced significantly in such devices, the extracted spin transport parameters are comparable to what has been observed on conventional SiO_2 substrates[37]. It is discussed that such low spin transport property is arising due to the fact that spin scattering at the supported contact area is masking the spin transport properties of the suspended area. The second attempt to achieve high quality spin transport was to fabricate the graphene-based spin valve devices on ultra flat hexagonal boron nitride substrate[152]. This attempt also failed due to the missing final annealing step which is crucial to get high quality electronic property by removing the fabrication contamination. Annealing damages the performance of the ferromagnetic contacts.

Recently, Columbia group created ultra high mobility graphene-based heterostructure devices without exposing the surface of graphene to any polymer during device fabrication[75]. High quality side contacts are formed at the 1D edge of a 2D graphene layer. The observation of low temperature ballistic transport over distances longer than 15 μm in such devices without requiring any annealing steps makes them an ideal platform to enhance the spin transport properties of graphene. Otani has calculated the non-local spin signal in a nonmagnetic material (Cu) injected and detected with transparent ferromagnetic contacts (Py) as[153]

$$\frac{\Delta V}{I} = R_{NL} = \frac{P_{FM}^2 R_{SFM}^2}{2R_{SFM} \exp\left(\frac{L}{\lambda_{NM}}\right) + R_{SNM} \sinh\left(\frac{L}{\lambda_{NM}}\right)} \tag{7.1}$$

where $P_{FM}$is the spin polarization factor of FM, L is the separation between injector and detector FM contacts and R_{SNM} and R_{SFM} are the spin resistances of NM and FM respectively. R_S can be described as

$$R_S = \frac{2\rho\lambda}{(1-P^2)A} \tag{7.2}$$

where A is the effective cross-sectional area between NM/ FM interface. As can be seen in equation 7-2, the small value of A causes an enhancement in non-local spin valve signal. In fact, spin injection to graphene with transparent contact has already been shown. In this heterostructure device, it is possible to solve two major problems of graphene spintronics: 1- Effective spin injection with extremely reduced interface area by depositing the side contacts and 2- Spin transport in ballistic regime.

Towards this, a BN/G/BN heterostructure device is fabricated with following the recipe shown in Reference [75]. The structure is etched in ribbon shape and side contacts are fabricated with ferromagnetic Co contacts followed by 5nm

Au capping layer. The device fabrication steps are shown in Figure 7-1 (a-c). The device has ~2kΩ contact resistance and the working contact yield is 100%. The room temperature mobility for the multilayer graphene based device shown in Figure 7-1-(a) is ~30,000 cm^2/Vs (Figure 7-1-(d)). The spin precession measurements in two probe local and four probe non-local configurations are performed. We observe an oscillatory behavior in non-local signal as a function of magnetic field in both measurement configurations, showing that spin injection through side contact without any tunnel barrier is successful. The further measurements and analyses will be performed for such devices.

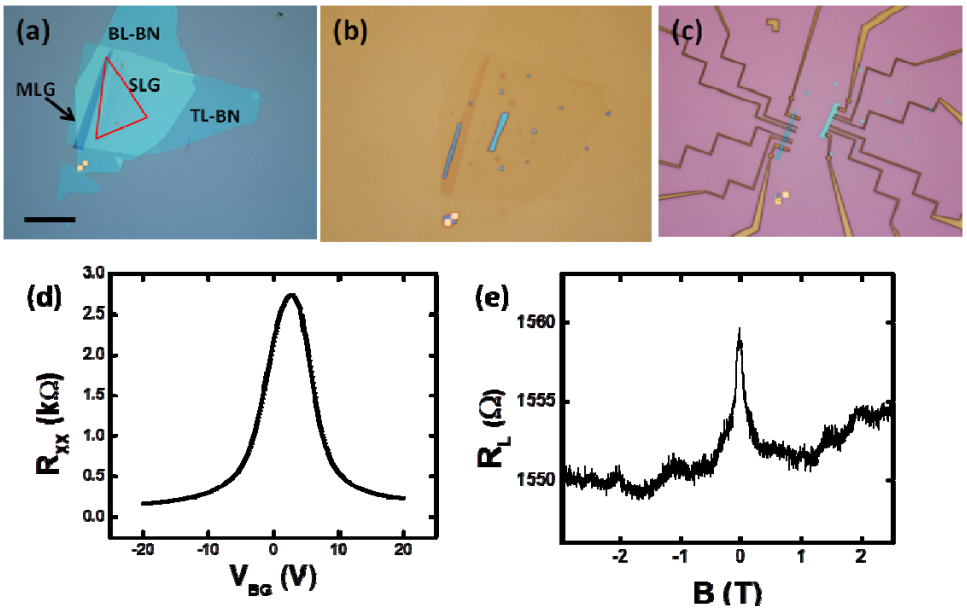

Figure 7-1. Side contact spin valve device: (a) The optical picture of BN/Graphene/BN heterostrusture after the transfer process. Single and multi-layer graphene (SLG and MLG respectively) are encapsulated between a bottom layer boron nitride (BL-BN) and a top layer boron nitride (TL-BN) crystals. The scale bar is 5um. (b) The bubble free graphene area is etched. (c) The final device after 30nm Co and 5nm Au contacts are formed. (d) Resistivity of graphene as a function of back gate voltage at room temperature. (e) Spin precession experiment in two terminal local geometry.

The negligibly small intrinsic spin orbit coupling (SOC) in graphene makes the realization of many interesting phenomena such as quantum spin Hall effect[131] and Datta-Das type spin transistor[132] practically impossible. Thus, an enhancement of graphene's SOC without degrading its exceptionally high charge mobility is crucial for the realization of such interesting phenomena. Towards this, we attempted to enhance the weak spin orbit coupling of graphene through a proximity effect. By transferring graphene on WS_2 substrate, we showed for the first time the spin-orbit proximity effect in graphene. We demonstrated a three order of magnitude enhancement of the SOC from its intrinsic low values of ~ 24 μeV to ~ 18 meV, while simultaneously preserving the exceptional electronic properties of pristine graphene**.** We also demonstrated, for the first time, that in such graphene/WS_2 ultrathin heterostructure the enhancement of the SOC gives rise to the SHE even at room temperature. Our detailed theoretical and experimental analyses showed that the origin of the proximity effect is intrinsic, unavoidable defects in the WS_2 substrate. These defects not only strongly enhance the SOC but also act as a sink for electronic charges of graphene once the Fermi level aligns with these localized states, resulting in gate bias independent graphene conductivity.

The realization of such high spin orbit coupling in high quality electronic device with micron size spin relaxation length opens the door for many interesting experiments.

1- The manipulation of spin current in top gated graphene-based spin field effect transistor devices fabricated on WS_2 substrate is possible thanks to the enhanced SOC strength and electronic mobility.

2- Graphene is the first model system predicted to be a topological insulator. However the weak spin orbit coupling of graphene makes the realization of such quantum phenomena impossible. It is recently discussed that the graphene layer sandwiched in between thin layer of Bi_2Te_3 can enhance the SOC significantly and more importantly

topological insulator behavior can be observed at experimentally accessible temperatures[154]. The experimental approach done with graphene/WS_2 heterostructures can be utilized to make such interesting experiment.

3- The transport measurement we performed in graphene onWS_2 substrate shows that sulphur vacancy is the origin of the observed proximity effect. The density of such sulphur vacancy can be engineered with a simple electron beam irradiation[149] and its effect on spin-orbit strength can be investigated. Moreover, the same experiment can be performed in graphene on single layer WS_2 to see the behavior of proximity in smaller density of sulphur vacancy.

Bibliography

[1] I. M. Ross, “The invention of the transistor,” *Proc. IEEE*, vol. 86, no. 1, pp. 7–28, 1998.

[2] W. Gerlach and O. Stern, “Das magnetische Moment des Silberatoms,” *Zeitschrift fur Phys.*, vol. 9, no. 1, pp. 353–355, 1922.

[3] G. and S. G. Uhlenbeck, *Nature*, vol. 117, p. 264, 1926.

[4] G. and S. G. Uhlenbeck, *Naturwissenschaften*, vol. 47, p. 264, 1925.

[5] S. A. Wolf, D. D. Awschalom, R. A. Buhrman, J. M. Daughton, S. von Molnár, M. L. Roukes, A. Y. Chtchelkanova, and D. M. Treger, “Spintronics: a spin-based electronics vision for the future.,” *Science*, vol. 294, no. 5546, pp. 1488–95, 2001.

[6] *Semiconductor Spintronics and Quantum Computation*. Springer, 2002, p. 315.

[7] W. Thomson, *Proc. R. Soc*, vol. 8, p. 546, 1857.

[8] W. Thomson, *Trans. R. Soc. London*, vol. 146, no. 649, 1856.

[9] M. N. Baibich, J. M. Broto, A. Fert, F. N. Van Dau, and F. Petroff, “Giant Magnetoresistance of (001)Fe/(001)Cr Magnetic Superlattices,” *Phys. Rev. Lett.*, vol. 61, no. 21, pp. 2472–2475, 1988.

[10] G. Binasch, P. Grünberg, F. Saurenbach, and W. Zinn, “Enhanced magnetoresistance in layered magnetic structures with antiferromagnetic interlayer exchange,” *Phys. Rev. B*, vol. 39, no. 7, pp. 4828–4830, 1989.

[11] C. H. Tsang, R. E. Fontana, T. Lin, D. E. Heim, B. A. Gurney, and M. L. Williams, “Design, fabrication, and performance of spin-valve read

heads for magnetic recording applications," *IBM J. Res. Dev.*, vol. 42, no. 1, pp. 103–116, 1998.

[12] T. Miyazaki and N. Tezuka, "Giant magnetic tunneling effect in Fe/Al2O3/Fe junction," *Journal of Magnetism and Magnetic Materials*, vol. 139, no. 3. pp. L231–L234, 1995.

[13] J. S. Moodera, L. R. Kinder, T. M. Wong, and R. Meservey, "Large Magnetoresistance at Room Temperature in Ferromagnetic Thin Film Tunnel Junctions," *Phys. Rev. Lett.*, vol. 74, no. 16, pp. 3273–3276, 1995.

[14] A. G. and G. E. P. Aronov, "No Title," *Fiz. Tekh. Poluprovodn.*, vol. 10, no. 1177, p. 1177, 1976.

[15] M. Johnson and R. H. Silsbee, "Interfacial charge-spin coupling: Injection and detection of spin magnetization in metals," *Phys. Rev. Lett.*, vol. 55, no. 17, pp. 1790–1793, 1985.

[16] F. J. Jedema, A. T. Filip, and B. J. van Wees, "Electrical spin injection and accumulation at room temperature in an all-metal mesoscopic spin valve.," *Nature*, vol. 410, no. 6826, pp. 345–8, 2001.

[17] F. Jedema, M. Nijboer, A. Filip,, and B. van Wees, "Spin injection and spin accumulation in all-metal mesoscopic spin valves," *Phys. Rev. B*, vol. 67, no. 8, p. 085319, 2003.

[18] F. J. Jedema, H. B. Heersche, A. T. Filip, J. J. A. Baselmans, and B. J. van Wees, "Electrical detection of spin precession in a metallic mesoscopic spin valve.," *Nature*, vol. 416, no. 6882, pp. 713–6, 2002.

[19] G. Schmidt, D. Ferrand, L. Molenkamp, A. Filip, and B. van Wees, "Fundamental obstacle for electrical spin injection from a ferromagnetic

metal into a diffusive semiconductor," *Phys. Rev. B*, vol. 62, no. 8, pp. R4790–R4793, 2000.

[20] I. Appelbaum, B. Huang, and D. J. Monsma, "Electronic measurement and control of spin transport in silicon.," *Nature*, vol. 447, no. 7142, pp. 295–8, 2007.

[21] S. P. Dash, S. Sharma, R. S. Patel, M. P. de Jong, and R. Jansen, "Electrical creation of spin polarization in silicon at room temperature.," *Nature*, vol. 462, no. 7272, pp. 491–4, 2009.

[22] K. S. Novoselov, A. K. Geim, S. V Morozov, D. Jiang, Y. Zhang, S. V Dubonos, I. V Grigorieva, and A. A. Firsov, "Electric field effect in atomically thin carbon films.," *Science*, vol. 306, no. 5696, pp. 666–9, 2004.

[23] D. H. Hernando, F. Guinea, and A. Brataas "Spin-orbit coupling in curved graphene, fullerenes, nanotubes, and nanotube caps.""Phys. Rev. B 74, 155426 (2006).

[24] B. Trauzettel, D. V. Bulaev, D. Loss, and G. Burkard, "Spin qubits in graphene quantum dots," *Nat. Phys.*, vol. 3, no. 3, pp. 192–196, 2007.

[25] K. I. Bolotin, K. J. Sikes, Z. Jiang, M. Klima, G. Fudenberg, J. Hone, P. Kim, and H. L. Stormer, "Ultrahigh electron mobility in suspended graphene," *Solid State Communications*, vol. 146, no. 9. pp. 351–355, 2008.

[26] B. Dlubak, M.-B. Martin, C. Deranlot, B. Servet, S. Xavier, R. Mattana, M. Sprinkle, C. Berger, W. A. De Heer, F. Petroff, A. Anane, P. Seneor, and A. Fert, "Highly efficient spin transport in epitaxial graphene on SiC," *Nat. Phys.*, vol. 8, no. 7, pp. 557–561, 2012.

[27] A. Avsar, T.-Y. Yang, S. Bae, J. Balakrishnan, F. Volmer, M. Jaiswal, Z. Yi, S. R. Ali, G. Güntherodt, B. H. Hong, B. Beschoten, and B. Özyilmaz, "Toward wafer scale fabrication of graphene based spin valve devices.," *Nano Lett.*, vol. 11, no. 6, pp. 2363–8, 2011.

[28] G.-X. Ni, Y. Zheng, S. Bae, H. R. Kim, A. Pachoud, Y. S. Kim, C.-L. Tan, D. Im, J.-H. Ahn, B. H. Hong, and B. Ozyilmaz, "Quasi-periodic nanoripples in graphene grown by chemical vapor deposition and its impact on charge transport.," *ACS Nano*, vol. 6, no. 2, pp. 1158–64, 2012.

[29] J. M. Wofford, S. Nie, K. F. McCarty, N. C. Bartelt, and O. D. Dubon, "Graphene Islands on Cu Foils: The Interplay between Shape, Orientation, and Defects." *Nano Lett.*, vol. 10, pp. 4890-4896, 2010.

[30] M. Popinciuc, C. Jozsa, P. J. Zormer, N. Tombros, A. Veligura, H. T. Jonkman, and B. J. van Wees, "Electronic spin transport in graphene field-effect transistors." Phys. Rev. B 80, 214427 (2009).

[31] F. J. Jedema, "PhD thesis" 2002.

[32] N. Tombros, "PhD thesis" 2008.

[33] D. R. Cooper, B. D'Anjou, N. Ghattamaneni, B. Harack, M. Hilke, A. Horth, N. Majlis, M. Massicotte, L. Vandsburger, E. Whiteway, and V. Yu, "Experimental review of graphene" 2011.

[34] J. Balakrishnan, "PhD thesis" 2014.

[35] A. Campbell, I. A. and Fert, "Chapter 9" in in *Ferromagnetic Materials*, 1982, p. 747.

[36] B. Leven and G. Dumpich, “Resistance behavior and magnetization reversal analysis of individual Co nanowires,” *Phys. Rev. B*, vol. 71, no. 6, p. 064411, 2005.

[37] N. Tombros, C. Jozsa, M. Popinciuc, H. T. Jonkman, and B. J. van Wees, “Electronic spin transport and spin precession in single graphene layers at room temperature.,” *Nature*, vol. 448, no. 7153, pp. 571–4, 2007.

[38] R. J. Elliott “Theory of the Effect of Spin-Orbit Coupling on Magnetic Resonance in Some Semiconductors.” Phys. Rev. 96, 266, 1954.

[39] M. I. D’Yakonov and V. I. Perel’, “Spin Orientation of Electrons Associated with the Interband Absorption of Light in Semiconductors,” *Sov. J. Exp. Theor. Phys.*, vol. 33, 1971.

[40] G.L. Bir, A.G. Aronov, G.E. Pikus “Spin relaxation of electrons due to scattering by holes,” Journal of Experimental and Theoretical Physics,vol.42, no. 4, p. 705, 1975.

[41] J.-H. Chen, C. Jang, S. Adam, M. S. Fuhrer, E. D. Williams, and M. Ishigami, “Charged-impurity scattering in graphene,” *Nat. Phys.*, vol. 4, no. 5, pp. 377–381, 2008.

[42] C. Ertler, S. Konschuh, M. Gmitra, and J. Fabian “Electron spin relaxation in graphene: The role of the substrate.” Phys. Rev. B 80, 041405, 2009.

[43] X. Li, C. W. Magnuson, A. Venugopal, J. An, J. W. Suk, B. Han, M. Borysiak, W. Cai, A. Velamakanni, Y. Zhu, L. Fu, E. M. Vogel, E. Voelkl, L. Colombo, and R. S. Ruoff, “Graphene films with large domain size by a two-step chemical vapor deposition process.,” *Nano Lett.*, vol. 10, no. 11, pp. 4328–34, 2010.

[44] K. I. Bolotin, K. J. Sikes, J. Hone, H. L. Stormer, and P. Kim, "Temperature-Dependent Transport in Suspended Graphene," *Phys. Rev. Lett.*, vol. 101, no. 9, p. 096802, 2008.

[45] C. Jozsa, T. Maassen, M. Popinciuc, P. J. Zomer, A. Veligura, H. T. Jonkman, and B. J. van Wees, "Linear scaling between momentum and spin scattering in graphene." Phys. Rev. B 80, 241403, 2009.

[46] T.-Y. Yang, J. Balakrishnan, F. Volmer, A. Avsar, M. Jaiswal, J. Samm, S. R. Ali, A. Pachoud, M. Zeng, M. Popinciuc, G. Güntherodt, B. Beschoten, and B. Özyilmaz, "Observation of Long Spin-Relaxation Times in Bilayer Graphene at Room Temperature," *Phys. Rev. Lett.*, vol. 107, no. 4, p. 047206, 2011.

[47] W. Han and R. K. Kawakami, "Spin Relaxation in Single-Layer and Bilayer Graphene," *Phys. Rev. Lett.*, vol. 107, no. 4, p. 047207, 2011.

[48] S. Takahashi and S. Maekawa, "Spin current, spin accumulation and spin Hall effect," *Sci. Technol. Adv. Mater.*, vol. 9, no. 1, p. 014105, 2008.

[49] D. Abanin, A. Shytov, L. Levitov, and B. Halperin, "Nonlocal charge transport mediated by spin diffusion in the spin Hall effect regime," *Phys. Rev. B*, vol. 79, no. 3, p. 035304, 2009.

[50] J. Balakrishnan, G. Kok Wai Koon, M. Jaiswal, A. H. Castro Neto, and B. Özyilmaz, "Colossal enhancement of spin–orbit coupling in weakly hydrogenated graphene," *Nat. Phys.*, vol. 9, no. 5, pp. 284–287, 2013.

[51] P. Wallace, "The Band Theory of Graphite," *Phys. Rev.*, vol. 71, no. 9, pp. 622–634, 1947.

[52] A. H. Castro Neto, N. M. R. Peres, K. S. Novoselov, and A. K. Geim, "The electronic properties of graphene," *Rev. Mod. Phys.*, vol. 81, no. 1, pp. 109–162, 2009.

[53] S. Adam and S. Das Sarma, "Boltzmann transport and residual conductivity in bilayer graphene," *Phys. Rev. B*, vol. 77, no. 11, p. 115436, 2008.

[54] T. J. B. M. Janssen, A. Tzalenchuk, S. L. Avila, S. Kubatkin, and V. I. Falko,"Quantum resistance metrology using graphene"Reports on Progress in Physics, 76, 104501, 2013.

[55] F. V. Tikhonenko, A. A. Kozikov, A. K. Savchenko, and R. V. Gorbachev, "Transition between Electron Localization and Antilocalization in Graphene," *Phys. Rev. Lett.*, vol. 103, no. 22, p. 226801, 2009.

[56] F. V. Tikhonenko, A. A. Kozikov, A. K. Savchenko, and R. V. Gorbachev, "Transition between Electron Localization and Antilocalization in Graphene," *Phys. Rev. Lett.*, vol. 103, no. 22, p. 226801, 2009.

[57] W. Ning, H. Du, F. Kong, J. Yang, Y. Han, M. Tian, and Y. Zhang, "One-dimensional weak antilocalization in single-crystal Bi2Te3 nanowires.," *Sci. Rep.*, vol. 3, p. 1564, 2013.

[58] X. Li, W. Cai, J. An, S. Kim, J. Nah, D. Yang, R. Piner, A. Velamakanni, I. Jung, E. Tutuc, S. K. Banerjee, L. Colombo, and R. S. Ruoff, "Large-area synthesis of high-quality and uniform graphene films on copper foils.," *Science*, vol. 324, no. 5932, pp. 1312–4, 2009.

[59] A. K. Geim and I. V Grigorieva, "Van der Waals heterostructures.," *Nature*, vol. 499, no. 7459, pp. 419–25, 2013.

[60] R. R. Nair, P. Blake, A. N. Grigorenko, K. S. Novoselov, T. J. Booth, T. Stauber, N. M. R. Peres, and A. K. Geim, "Fine structure constant defines visual transparency of graphene.," *Science*, vol. 320, no. 5881, p. 1308, 2008.

[61] P. Blake, E. W. Hill, A. H. Castro Neto, K. S. Novoselov, D. Jiang, R. Yang, T. J. Booth, and A. K. Geim, "Making graphene visible," *Appl. Phys. Lett.*, vol. 91, no. 6, p. 063124, 2007.

[62] C. J. Docherty, C.-T. Lin, H. J. Joyce, R. J. Nicholas, L. M. Herz, L.-J. Li, and M. B. Johnston, "Extreme sensitivity of graphene photoconductivity to environmental gases.," *Nat. Commun.*, vol. 3, p. 1228, 2012.

[63] W. G. Cullen, M. Yamamoto, K. M. Burson, J. H. Chen, C. Jang, L. Li, M. S. Fuhrer, and E. D. Williams, "High-Fidelity Conformation of Graphene to SiO2 Topographic Features," *Phys. Rev. Lett.*, vol. 105, no. 21, p. 215504, 2010.

[64] A. C. Ferrari and D. M. Basko, "Raman spectroscopy as a versatile tool for studying the properties of graphene.," *Nat. Nanotechnol.*, vol. 8, no. 4, pp. 235–46, 2013.

[65] C. Berger, Z. Song, T. Li, X. Li, A. Y. Ogbazghi, R. Feng, Z. Dai, A. N. Marchenkov, E. H. Conrad, P. N. First, and W. A. de Heer, "Ultrathin Epitaxial Graphite: 2D Electron Gas Properties and a Route toward Graphene-based Nanoelectronics," *J. Phys. Chem. B*, vol. 108, no. 52, pp. 19912–19916, 2004.

[66] S. Bae, H. Kim, Y. Lee, X. Xu, J.-S. Park, Y. Zheng, J. Balakrishnan, T. Lei, H. R. Kim, Y. Il Song, Y.-J. Kim, K. S. Kim, B. Ozyilmaz, J.-H. Ahn, B. H. Hong, and S. Iijima, "Roll-to-roll production of 30-inch

graphene films for transparent electrodes.," *Nat. Nanotechnol.*, vol. 5, no. 8, pp. 574–8, 2010.

[67] Y. Zhu, S. Murali, W. Cai, X. Li, J. W. Suk, J. R. Potts, and R. S. Ruoff, "Graphene and graphene oxide: synthesis, properties, and applications.," *Adv. Mater.*, vol. 22, no. 35, pp. 3906–24, 2010.

[68] Y. Hao, M. S. Bharathi, L. Wang, Y. Liu, H. Chen, S. Nie, X. Wang, H. Chou, C. Tan, B. Fallahazad, H. Ramanarayan, C. W. Magnuson, E. Tutuc, B. I. Yakobson, K. F. McCarty, Y.-W. Zhang, P. Kim, J. Hone, L. Colombo, and R. S. Ruoff, "The role of surface oxygen in the growth of large single-crystal graphene on copper.," *Science*, vol. 342, no. 6159, pp. 720–3, 2013.

[69] B. Radisavljevic, A. Radenovic, J. Brivio, V. Giacometti, and A. Kis, "Single-layer MoS2 transistors.," *Nat. Nanotechnol.*, vol. 6, no. 3, pp. 147–50, 2011.

[70] K. Roy, M. Padmanabhan, S. Goswami, T. P. Sai, G. Ramalingam, S. Raghavan, and A. Ghosh, "Graphene-MoS2 hybrid structures for multifunctional photoresponsive memory devices.," *Nat. Nanotechnol.*, vol. 8, no. 11, pp. 826–30, 2013.

[71] W. J. Yu, Y. Liu, H. Zhou, A. Yin, Z. Li, Y. Huang, and X. Duan, "Highly efficient gate-tunable photocurrent generation in vertical heterostructures of layered materials.," *Nat. Nanotechnol.*, vol. 8, no. 12, pp. 952–8, 2013.

[72] H. Yuan, M. S. Bahramy, K. Morimoto, S. Wu, K. Nomura, B.-J. Yang, H. Shimotani, R. Suzuki, M. Toh, C. Kloc, X. Xu, R. Arita, N. Nagaosa, and Y. Iwasa, "Zeeman-type spin splitting controlled by an electric field," *Nat. Phys.*, vol. 9, no. 9, pp. 563–569, 2013.

[73] K. S. Novoselov and A. H. Castro Neto, "Two-dimensional crystals-based heterostructures: materials with tailored properties," *Phys. Scr.*, vol. T146, no. T146, p. 014006, 2012.

[74] A. S. Mayorov, R. V Gorbachev, S. V Morozov, L. Britnell, R. Jalil, L. A. Ponomarenko, P. Blake, K. S. Novoselov, K. Watanabe, T. Taniguchi, and A. K. Geim, "Micrometer-scale ballistic transport in encapsulated graphene at room temperature.," *Nano Lett.*, vol. 11, no. 6, pp. 2396–9, 2011.

[75] L. Wang, I. Meric, P. Y. Huang, Q. Gao, Y. Gao, H. Tran, T. Taniguchi, K. Watanabe, L. M. Campos, D. A. Muller, J. Guo, P. Kim, J. Hone, K. L. Shepard, and C. R. Dean, "One-dimensional electrical contact to a two-dimensional material.," *Science*, vol. 342, no. 6158, pp. 614–7, 2013.

[76] C. R. Dean, A. F. Young, P. Cadden-Zimansky, L. Wang, H. Ren, K. Watanabe, T. Taniguchi, P. Kim, J. Hone, and K. L. Shepard, "Multicomponent fractional quantum Hall effect in graphene," *Nat. Phys.*, vol. 7, no. 9, pp. 693–696, 2011.

[77] M. S. Choi, G.-H. Lee, Y.-J. Yu, D.-Y. Lee, S. H. Lee, P. Kim, J. Hone, and W. J. Yoo, "Controlled charge trapping by molybdenum disulphide and graphene in ultrathin heterostructured memory devices.," *Nat. Commun.*, vol. 4, p. 1624, 2013.

[78] L. Britnell, R. V Gorbachev, R. Jalil, B. D. Belle, F. Schedin, A. Mishchenko, T. Georgiou, M. I. Katsnelson, L. Eaves, S. V Morozov, N. M. R. Peres, J. Leist, A. K. Geim, K. S. Novoselov, and L. A. Ponomarenko, "Field-effect tunneling transistor based on vertical graphene heterostructures.," *Science*, vol. 335, no. 6071, pp. 947–50, 2012.

[79] L. Britnell, R. M. Ribeiro, A. Eckmann, R. Jalil, B. D. Belle, A. Mishchenko, Y.-J. Kim, R. V Gorbachev, T. Georgiou, S. V Morozov, A. N. Grigorenko, A. K. Geim, C. Casiraghi, A. H. Castro Neto, and K. S. Novoselov, "Strong light-matter interactions in heterostructures of atomically thin films.," *Science*, vol. 340, no. 6138, pp. 1311–4, 2013.

[80] C. R. Dean, A. F. Young, I. Meric, C. Lee, L. Wang, S. Sorgenfrei, K. Watanabe, T. Taniguchi, P. Kim, K. L. Shepard, and J. Hone, "Boron nitride substrates for high-quality graphene electronics.," *Nat. Nanotechnol.*, vol. 5, no. 10, pp. 722–6, 2010.

[81] L. Britnell, R. V Gorbachev, R. Jalil, B. D. Belle, F. Schedin, M. I. Katsnelson, L. Eaves, S. V Morozov, A. S. Mayorov, N. M. R. Peres, A. H. C. Neto, J. Leist, A. K. Geim, L. A. Ponomarenko, and K. S. Novoselov, "Electron tunneling through ultrathin boron nitride crystalline barriers.," *Nano Lett.*, vol. 12, no. 3, pp. 1707–10, 2012.

[82] W. Jin, P.-C. Yeh, N. Zaki, D. Zhang, J. T. Sadowski, A. Al-Mahboob, A. M. van der Zande, D. A. Chenet, J. I. Dadap, I. P. Herman, P. Sutter, J. Hone, and R. M. Osgood, "Direct Measurement of the Thickness-Dependent Electronic Band Structure of MoS2 Using Angle-Resolved Photoemission Spectroscopy," *Phys. Rev. Lett.*, vol. 111, no. 10, p. 106801, 2013.

[83] W. Y. Di Xiao, Gui-Bin Liu, Wanxiang Feng, Xiaodong Xu, "Coupled Spin and Valley Physics in Monolayers of MoS2 and Other Group-VI Dichalcogenides." Phys. Rev. Lett. 108, 196802, 2012.

[84] J.-H. Chen, C. Jang, S. Xiao, M. Ishigami, and M. S. Fuhrer, "Intrinsic and extrinsic performance limits of graphene devices on SiO2.," *Nat. Nanotechnol.*, vol. 3, no. 4, pp. 206–9, 2008.

[85] W. Pan, J. Xiao, J. Zhu, C. Yu, G. Zhang, Z. Ni, K. Watanabe, T. Taniguchi, Y. Shi, and X. Wang, "Biaxial compressive strain engineering in graphene/boron nitride heterostructures.," *Sci. Rep.*, vol. 2, p. 893, 2012.

[86] S. J. Haigh, A. Gholinia, R. Jalil, S. Romani, L. Britnell, D. C. Elias, K. S. Novoselov, L. A. Ponomarenko, A. K. Geim, and R. Gorbachev, "Cross-sectional imaging of individual layers and buried interfaces of graphene-based heterostructures and superlattices.," *Nat. Mater.*, vol. 11, no. 9, pp. 764–7, 2012.

[87] A. K. Geim, "Graphene: status and prospects.," *Science*, vol. 324, no. 5934, pp. 1530–4, 2009.

[88] W. Han, K. Pi, W. Bao, K. M. McCreary, Y. Li, W. H. Wang, C. N. Lau, and R. K. Kawakami, "Electrical detection of spin precession in single layer graphene spin valves with transparent contacts," *Appl. Phys. Lett.*, vol. 94, no. 22, p. 222109, 2009.

[89] M. Shiraishi, M. Ohishi, R. Nouchi, N. Mitoma, T. Nozaki, T. Shinjo, and Y. Suzuki, "Robustness of Spin Polarization in Graphene-Based Spin Valves," *Adv. Funct. Mater.*, vol. 19, no. 23, pp. 3711–3716, 2009.

[90] H. C. Koo, J. H. Kwon, J. Eom, J. Chang, S. H. Han, and M. Johnson, "Control of spin precession in a spin-injected field effect transistor.," *Science*, vol. 325, no. 5947, pp. 1515–8, 2009.

[91] P. Michetti, P. Recher, and G. Iannaccone, "Electric field control of spin rotation in bilayer graphene.," *Nano Lett.*, vol. 10, no. 11, pp. 4463–9, 2010.

[92] H. Dery, B. Ciftcioglu, Y. Song, H. Wu, M. Huang, R. Kawakami, J. Shi, I. Krivorotov, I. Zutic, and L. J. Sham, "Spintronics search engines," in *69th Device Research Conference*, 2011, pp. 147–148.

[93] A. Ferreira, X. Xu, C.-L. Tan, S.-K. Bae, N. M. R. Peres, B.-H. Hong, B. Özyilmaz, and A. H. Castro Neto, "Transport properties of graphene with one-dimensional charge defects," *EPL (Europhysics Lett.*, vol. 94, no. 2, p. 28003, 2011.

[94] S. Lee, K. Lee, and Z. Zhong, "Wafer scale homogeneous bilayer graphene films by chemical vapor deposition.," *Nano Lett.*, vol. 10, no. 11, pp. 4702–7, 2010.

[95] N. Petrone, C. R. Dean, I. Meric, A. M. van der Zande, P. Y. Huang, L. Wang, D. Muller, K. L. Shepard, and J. Hone, "Chemical vapor deposition-derived graphene with electrical performance of exfoliated graphene.," *Nano Lett.*, vol. 12, no. 6, pp. 2751–6, 2012.

[96] X. Li, C. W. Magnuson, A. Venugopal, J. An, J. W. Suk, B. Han, M. Borysiak, W. Cai, A. Velamakanni, Y. Zhu, L. Fu, E. M. Vogel, E. Voelkl, L. Colombo, and R. S. Ruoff, "Graphene films with large domain size by a two-step chemical vapor deposition process.," *Nano Lett.*, vol. 10, no. 11, pp. 4328–34, 2010.

[97] S. Yuasa, T. Nagahama, A. Fukushima, Y. Suzuki, and K. Ando, "Giant room-temperature magnetoresistance in single-crystal Fe/MgO/Fe magnetic tunnel junctions.," *Nat. Mater.*, vol. 3, no. 12, pp. 868–71, 2004.

[98] R. Nouchi and K. Tanigaki, "Charge-density depinning at metal contacts of graphene field-effect transistors," *Appl. Phys. Lett.*, vol. 96, no. 25, p. 253503, 2010.

[99] K. S. Novoselov, E. McCann, S. V. Morozov, V. I. Fal'ko, M. I. Katsnelson, U. Zeitler, D. Jiang, F. Schedin, and A. K. Geim, "Unconventional quantum Hall effect and Berry's phase of 2π in bilayer graphene," *Nat. Phys.*, vol. 2, no. 3, pp. 177–180, 2006.

[100] Y. W. Tan, Y. Zhang, K. Bolotin, Y. Zhao, S. Adam, E. H. Hwang, S. Das Sarma, H. L. Stormer, and P. Kim "Measurement of Scattering Rate and Minimum Conductivity in Graphene." Phys. Rev. Lett. 99, 246803 2007.

[101] M. Monteverde, C. O. Aristizabal, R. Weil, K. Bennaceur, N. Ferrier, S. Gueron, C. Glatti, H. Bouchiat, J. N. Fuchs, and D. L. Maslov Transport and Elastic Scattering Times as Probes of the Nature of Impurity Scattering in Single-Layer and Bilayer Graphene." Phys. Rev. Lett. 104, 126801, 2010.

[102] J. Heo, H. J. Chung, S.-H. Lee, H. Yang, D. H. Seo, J. K. Shin, U.-I. Chung, S. Seo, E. H. Hwang, and S. Das Sarma, "Nonmonotonic temperature dependent transport in graphene grown by chemical vapor deposition," *Phys. Rev. B*, vol. 84, no. 3, p. 035421, 2011.

[103] F. Kuemmeth, S. Ilani, D. C. Ralph, and P. L. McEuen, "Coupling of spin and orbital motion of electrons in carbon nanotubes.," *Nature*, vol. 452, no. 7186, pp. 448–52, 2008.

[104] M. Gmitra, S. Konschuh, C. Ertler, C. Ambrosch-Draxl, and J. Fabian, "Band-structure topologies of graphene: Spin-orbit coupling effects from first principles," *Phys. Rev. B*, vol. 80, no. 23, p. 235431, 2009.

[105] A. H. Castro Neto, and F. Guinea "Impurity-Induced Spin-Orbit Coupling in Graphene." Phys. Rev. Lett. 103, 026804, 2009.

[106] W. Han, K. Pi, K. M. M. McCreary, Y. Li, J. J. I. Wong, A. G. Swartz, R. K. Kawakami, "Tunneling Spin Injection into Single Layer Graphene." Phys. Rev. Lett. 105, 167202, 2010.

[107] S. M. Kim, E. B. Song, S. Lee, J. Zhu, D. H. Seo, M. Mecklenburg, S. Seo, and K. L. Wang, "Transparent and flexible graphene charge-trap memory.," *ACS Nano*, vol. 6, no. 9, pp. 7879–84, 2012.

[108] P. Rickhaus, R. Maurand, M.-H. Liu, M. Weiss, K. Richter, and C. Schönenberger, "Ballistic interferences in suspended graphene.," *Nat. Commun.*, vol. 4, p. 2342, 2013.

[109] D. C. Elias, R. V. Gorbachev, A. S. Mayorov, S. V. Morozov, A. A. Zhukov, P. Blake, L. A. Ponomarenko, I. V. Grigorieva, K. S. Novoselov, F. Guinea, and A. K. Geim, "Dirac cones reshaped by interaction effects in suspended graphene," *Nat. Phys.*, vol. 8, no. 2, pp. 172–172, 2012.

[110] T. Taniguchi and K. Watanabe, "Synthesis of high-purity boron nitride single crystals under high pressure by using Ba–BN solvent," *J. Cryst. Growth*, vol. 303, no. 2, pp. 525–529, 2007.

[111] W. Zhao, Z. Ghorannevis, L. Chu, M. Toh, C. Kloc, P.-H. Tan, and G. Eda, "Evolution of electronic structure in atomically thin sheets of WS2 and WSe2.," *ACS Nano*, vol. 7, no. 1, pp. 791–7, 2013.

[112] C. Gong, H. Zhang, W. Wang, L. Colombo, R. M. Wallace, and K. Cho, "Band alignment of two-dimensional transition metal dichalcogenides: Application in tunnel field effect transistors," *Appl. Phys. Lett.*, vol. 103, no. 5, p. 053513, 2013.

[113] J. Martin, N. Akerman, G. Ulbricht, T. Lohmann, J. H. Smet, K. von Klitzing, and A. Yacoby, "Observation of electron–hole puddles in

graphene using a scanning single-electron transistor," *Nat. Phys.*, vol. 4, no. 2, pp. 144–148, 2007.

[114] S. Adam, E. H. Hwang, V. M. Galitski, and S. Das Sarma, "A self-consistent theory for graphene transport.," *Proc. Natl. Acad. Sci. U. S. A.*, vol. 104, no. 47, pp. 18392–7, 2007.

[115] F. Schwierz, "Graphene transistors.," *Nat. Nanotechnol.*, vol. 5, no. 7, pp. 487–96, 2010.

[116] S. Morozov, K. Novoselov, M. Katsnelson, F. Schedin, D. Elias, J. Jaszczak, and A. Geim, "Giant Intrinsic Carrier Mobilities in Graphene and Its Bilayer," *Phys. Rev. Lett.*, vol. 100, no. 1, p. 016602, 2008.

[117] T. Stauber, N. Peres, and F. Guinea, "Electronic transport in graphene: A semiclassical approach including midgap states," *Phys. Rev. B*, vol. 76, no. 20, p. 205423, 2007.

[118] M. I. Katsnelson and A. K. Geim, "Electron scattering on microscopic corrugations in graphene.," *Philos. Trans. A. Math. Phys. Eng. Sci.*, vol. 366, no. 1863, pp. 195–204, 2008.

[119] J. Moser, A. Barreiro, and A. Bachtold, "Current-induced cleaning of graphene," *Appl. Phys. Lett.*, vol. 91, no. 16, p. 163513, 2007.

[120] P. J. Zomer, S. P. Dash, N. Tombros, and B. J. van Wees, "A transfer technique for high mobility graphene devices on commercially available hexagonal boron nitride," *Appl. Phys. Lett.*, vol. 99, no. 23, p. 232104, 2011.

[121] L. Wang, Z. Chen, C. R. Dean, T. Taniguchi, K. Watanabe, L. E. Brus, and J. Hone, "Negligible environmental sensitivity of graphene in a

hexagonal boron nitride/graphene/h-BN sandwich structure.," *ACS Nano*, vol. 6, no. 10, pp. 9314–9, 2012.

[122] J. Zabel, R. R. Nair, A. Ott, T. Georgiou, A. K. Geim, K. S. Novoselov, and C. Casiraghi, "Raman spectroscopy of graphene and bilayer under biaxial strain: bubbles and balloons.," *Nano Lett.*, vol. 12, no. 2, pp. 617–21, 2012.

[123] N. Levy, S. A. Burke, K. L. Meaker, M. Panlasigui, A. Zettl, F. Guinea, A. H. Castro Neto, and M. F. Crommie, "Strain-induced pseudo-magnetic fields greater than 300 tesla in graphene nanobubbles.," *Science*, vol. 329, no. 5991, pp. 544–7, 2010.

[124] M. Fogler, F. Guinea, and M. Katsnelson, "Pseudomagnetic Fields and Ballistic Transport in a Suspended Graphene Sheet," *Phys. Rev. Lett.*, vol. 101, no. 22, p. 226804, 2008.

[125] F. Guinea, M. I. Katsnelson, and A. K. Geim, "Energy gaps and a zero-field quantum Hall effect in graphene by strain engineering," *Nat. Phys.*, vol. 6, no. 1, pp. 30–33, 2009.

[126] M. Yamamoto, T. L. Einstein, M. S. Fuhrer, and W. G. Cullen, "Charge inhomogeneity determines oxidative reactivity of graphene on substrates.," *ACS Nano*, vol. 6, no. 9, pp. 8335–41, 2012.

[127] L. A. Ponomarenko, R. Yang, T. M. Mohiuddin, M. I. Katsnelson, K. S. Novoselov, S. V. Morozov, A. A. Zhukov, F. Schedin, E. W. Hill, and A. K. Geim, "Effect of a High-κ Environment on Charge Carrier Mobility in Graphene," *Phys. Rev. Lett.*, vol. 102, no. 20, p. 206603, 2009.

[128] W. Kim, A. Javey, O. Vermesh, Q. Wang, Y. Li, and H. Dai, "Hysteresis Caused by Water Molecules in Carbon Nanotube Field-Effect Transistors," *Nano Lett.*, vol. 3, no. 2, pp. 193–198, 2003.

[129] H. Wang, Y. Wu, C. Cong, J. Shang, and T. Yu, "Hysteresis of electronic transport in graphene transistors.," *ACS Nano*, vol. 4, no. 12, pp. 7221–8, 2010.

[130] T. Maassen, J. J. van den Berg, N. Ijbema, F. Fromm, T. Seyller, R. Yakimova, and B. J. van Wees, "Long spin relaxation times in wafer scale epitaxial graphene on SiC(0001).," *Nano Lett.*, vol. 12, no. 3, pp. 1498–502, 2012.

[131] C. L. Kane and E. J. Mele, "Quantum Spin Hall Effect in Graphene," *Phys. Rev. Lett.*, vol. 95, no. 22, p. 226801, 2005.

[132] S. Datta and B. Das, "Electronic analog of the electro-optic modulator," *Appl. Phys. Lett.*, vol. 56, no. 7, p. 665, 1990.

[133] S. Konschuh, M. Gmitra, and J. Fabian, "Tight-binding theory of the spin-orbit coupling in graphene," *Phys. Rev. B*, vol. 82, no. 24, p. 245412, 2010.

[134] M. Wojtaszek, I. J. Vera-Marun, T. Maassen, and B. J. van Wees, "Enhancement of spin relaxation time in hydrogenated graphene spin-valve devices," *Phys. Rev. B*, vol. 87, no. 8, p. 081402, 2013.

[135] M. Gmitra, D. Kochan, and J. Fabian, "Spin-Orbit Coupling in Hydrogenated Graphene," *Phys. Rev. Lett.*, vol. 110, no. 24, p. 246602, 2013.

[136] D. Ma, Z. Li, and Z. Yang, "Strong spin–orbit splitting in graphene with adsorbed Au atoms," *Carbon N. Y.*, vol. 50, no. 1, pp. 297–305, 2012.

[137] C. Weeks, J. Hu, J. Alicea, M. Franz, and R. Wu, "Engineering a Robust Quantum Spin Hall State in Graphene via Adatom Deposition," *Phys. Rev. X*, vol. 1, no. 2, p. 021001, 2011.

[138] K. Pi, W. Han, K. M. McCreary, A. G. Swartz, Y. Li, and R. K. Kawakami, "Manipulation of Spin Transport in Graphene by Surface Chemical Doping," *Phys. Rev. Lett.*, vol. 104, no. 18, p. 187201, 2010.

[139] Q. H. Wang, K. Kalantar-Zadeh, A. Kis, J. N. Coleman, and M. S. Strano, "Electronics and optoelectronics of two-dimensional transition metal dichalcogenides.," *Nat. Nanotechnol.*, vol. 7, no. 11, pp. 699–712, 2012.

[140] http://ulisse.elettra.trieste.it/services/elements/WebElements.html.

[141] F. Y. Xie, L. Gong, X. Liu, Y. T. Tao, W. H. Zhang, S. H. Chen, H. Meng, and J. Chen, "XPS studies on surface reduction of tungsten oxide nanowire film by Ar+ bombardment," *J. Electron Spectros. Relat. Phenomena*, vol. 185, no. 3, pp. 112–118, 2012.

[142] S. Tanuma, C. J. Powell, and D. R. Penn, "Proposed formula for electron inelastic mean free paths based on calculations for 31 materials," *Surf. Sci.*, vol. 192, no. 1, pp. L849–L857, 1987.

[143] A. Berkdemir, H. R. Gutiérrez, A. R. Botello-Méndez, N. Perea-López, A. L. Elías, C.-I. Chia, B. Wang, V. H. Crespi, F. López-Urías, J.-C. Charlier, H. Terrones, and M. Terrones, "Identification of individual and few layers of WS2 using Raman spectroscopy.," *Sci. Rep.*, vol. 3, p. 1755, 2013.

[144] K. S. Novoselov, A. K. Geim, S. V Morozov, D. Jiang, M. I. Katsnelson, I. V Grigorieva, S. V Dubonos, and A. A. Firsov, "Two-dimensional gas of massless Dirac fermions in graphene.," *Nature*, vol. 438, no. 7065, pp. 197–200, 2005.

[145] Y. Zhang, Y.-W. Tan, H. L. Stormer, and P. Kim, "Experimental observation of the quantum Hall effect and Berry's phase in graphene.," *Nature*, vol. 438, no. 7065, pp. 201–4, 2005.

[146] J. Renard, M. Studer, and J. A. Folk, "Origins of Nonlocality near the Dirac Point in Graphene," Phys. Rev. Lett., vol. 112, no. 116601, 2014.

[147] D. A. Abanin, S. V Morozov, L. A. Ponomarenko, R. V Gorbachev, A. S. Mayorov, M. I. Katsnelson, K. Watanabe, T. Taniguchi, K. S. Novoselov, L. S. Levitov, and A. K. Geim, "Giant nonlocality near the Dirac point in graphene.," *Science*, vol. 332, no. 6027, pp. 328–30, 2011.

[148] F. V. Tikhonenko, D. W. Horsell, R. V. Gorbachev, and A. K. Savchenko, "Weak Localization in Graphene Flakes," *Phys. Rev. Lett.*, vol. 100, no. 5, p. 056802, 2008.

[149] W. Zhou, X. Zou, S. Najmaei, Z. Liu, Y. Shi, J. Kong, J. Lou, P. M. Ajayan, B. I. Yakobson, and J.-C. Idrobo, "Intrinsic structural defects in monolayer molybdenum disulfide.," *Nano Lett.*, vol. 13, no. 6, pp. 2615–22, 2013.

[150] A. Carvalho, R. M. Ribeiro, and A. H. Castro Neto, "Band nesting and the optical response of two-dimensional semiconducting transition metal dichalcogenides," *Phys. Rev. B*, vol. 88, no. 11, p. 115205, 2013.

[151] M. H. D. Guimarães, A. Veligura, P. J. Zomer, T. Maassen, I. J. Vera-Marun, N. Tombros, and B. J. van Wees, "Spin transport in high-quality suspended graphene devices.," *Nano Lett.*, vol. 12, no. 7, pp. 3512–7, 2012.

[152] P. J. Zomer, M. H. D. Guimarães, N. Tombros, and B. J. van Wees, "Long-distance spin transport in high-mobility graphene on hexagonal boron nitride," *Phys. Rev. B*, vol. 86, no. 16, p. 161416, 2012.

[153] T. Yang, T. Kimura, and Y. Otani, “Giant spin-accumulation signal and pure spin-current-induced reversible magnetization switching,” *Nat. Phys.*, vol. 4, no. 11, pp. 851–854, 2008.

[154] L. Kou, F. Hu, B. Yan, T. Wehling, C. Felser, T. Frauenheim, and C. Chen, “Proximity Enhanced Quantum Spin Hall State in Graphene,”arXiv: 1309.6653, 2013.

List of Publications

1. J. Balakrishnan, G. K. W. Koon, A. Avsar, Y. Ho, J. H. Lee, M. Jaiswal, A. Ferreira, A. H. Castro Neto, M. A. Cazalilla and B. Özyilmaz, Giant Spin Hall Effect in CVD Graphene, Submitted (2014).
2. J. Y. Tan, A. Avsar, J. Balakrishnan, G. K. W. Koon, T. Taychanatapat, E. C. T. O'Farrell, K. Watanabe, T. Taniguchi, G. Eda and B. Özyilmaz, Substrate Engineering in Graphene-based heterostructures, Appl. Phys. Lett. 104, 183504 (2014).
3. A. Avsar, J. Y. Tan, J. Balakrishnan, G. K. W. Koon, J. Lahiri, A. Carvalho, A. Rodin, T. Taychanatapat, E. C. T. O'Farrell, G. Eda, A. H. Castro Neto and B. Özyilmaz, Spin-Orbit Proximity Effect in Graphene, Submitted (2013).
4. T. Y. Yang, J. Balakrishnan, F. Volmer, A. Avsar, M. Jaiswal, J. Samm, S. R. Ali, A. Pachoud, M. Zeng, M. Popinciuc, B. Beschoten and B. Özyilmaz, Observation of long spin relaxation times in bilayer graphene at room temperature, Physical Review Letters, 107, 047206 (2011).
5. A. Avsar, T. Y. Yang, S. Bae, J. Balakrishnan, F. Volmer, M. Jaiswal, Z. Yi, S. R. Ali, G. Guntherodt, B. H. Hong, B. Beschoten and B. Özyilmaz, Toward Wafer Scale Fabrication of Graphene Based Spin Valves, Nano Letters, 11, 2363 (2011).